MARMARA UNIVERSITY
INSTITUTE FOR GRADUATE STUDIES
IN PURE AND APPLIED SCIENCES

DESIGN AND FABRICATION OF A NOVEL LAMB WAVE DEVICE

SALİH ÇOLAKOĞLU

MASTER THESIS
Department of Electrical and Electronics Engineering

Thesis Supervisor
Assist. Prof. Alper Şişman

ISTANBUL, 2021

MARMARA UNIVERSITY
INSTITUTE FOR GRADUATE STUDIES IN PURE AND APPLIED SCIENCES

Salih ÇOLAKOĞLU, a Master of Science student of Marmara University Institute for Graduate Studies in Pure and Applied Sciences, defended his thesis entitled "**Design, fabrication, and characterization studies of a novel lamb wave device**", on ……………. and has been found to be satisfactory by the jury members.

Jury Members
Assist. Prof. Dr. Alper Şişman (Advisor)
Marmara University .... (SIGN) ....

Assoc. Prof. Adı SOYADI (Jury Member)
Marmara University .... (SIGN) ....

Assist. Prof. Adı SOYADI (Jury Member)
Marmara University .... (SIGN) ....

APPROVAL

Marmara University Institute for Graduate Studies in Pure and Applied Sciences Executive Committee approves that Salih ÇOLAKOĞLU be granted the degree of Master of Science in Department of Electrical and Electronics Engineering, Electrical and Electronics Engineering Program on …….. . (Resolution no: …………………………...).

Director of the Institute
Prof. Dr. Bülent EKİCİ

Acknowledgment

First, I would like to express my sincere gratitude to my advisor, Assist. Prof. Dr. Alper Şişman, who has been there to provide unconditionally his constant supervision and support, trust and tolerance and always wanting us, his students, to understand, and perform to the best of our ability. I am thankful to Dr. Alper ŞİŞMAN for introducing me to the world of Micro-electromechanical systems and for being given the opportunity to be a part of the Sabancı University Nanotechnology Research and Application Center (SUNUM) team member. Also, I would like to thank my colleagues in SUNUM laboratory for their help through my thesis. My sincere thankfulness also goes to my great teachers.

Second, I must express my very profound gratitude to my dear family, my mother and father for helping me through my thesis study and also assisting me during thesis writing, and providing me with unfailing support and continuous encouragement throughout my years of study and throughout my life. This accomplishment would not have been possible without them.

Finally, I would like to thank the scientific and technological research council of Turkey (TÜBİTAK) for financial support and help in making this project (215E098) come to life.

CONTENTS

Acknowledgment........ii

Contents........iii

ÖZET........v

ABSTRACT........vi

LIST OF SYMBOLS........vii

LIST OF ABBRAVIATIONS........ix

LIST OF FIGURES........xi

LIST OF TABLES........xiii

LIST OF SCHEMATICS........xiv

1. INTRODUCTION........1

- 1.1. General Information And Applications........1
- 1.2. Brief History........3
- 1.3. Literature Studies........5
  - 1.3.1. Studies on the band of the filter........7
  - 1.3.2. Adjustable frequency oscillator design........8
  - 1.3.3. Adjustable phase SAW – LW filter / SAW – LW phase modulation........9
- 1.4. The Motivation For This Thesis Work........9
  - 1.4.1. Material characterization........9
  - 1.4.2. Theory and simulation studies........10
  - 1.4.3. Fabrication testing and verification studies........10

2. GENERAL BACKGROUND........11

- 2.1. Lamb Waves........11
- 2.2. IDTs........12
- 2.3. Lamb Wave Devices........15

3. THESIS STUDIES........18

- 3.1. Methodology........18
  - 3.1.1. Mechanical analysis........21
  - 3.1.2. Electrical analysis........22
  - 3.1.3. Lamb wave velocity with thin film precipitation........23

3.2. Design Fabrication And Validation Of A Lamb Wave Device ……………………...…………..27
  3.2.1. Design and simulation studies………………………………………………..…………...28
    3.2.1.1. Developing a finite element analysis model for design, performing analysis through simulation……………………………………………………………………28
    3.2.1.2. The Designs of the fabricated LW device……………………………………35
  3.2.2. Fabrication and characterization studies……………………………………………...36
    3.2.2.1. Coating and fabrication of a thin film……………………………………...37
      3.2.2.1.1. Thin-Film characterization…………………………………………...47
      3.2.2.1.2. ALN film orientation tests…………………………………………...49
    3.2.2.2. Photolithography and etching…………………………………………………53
      3.2.2.2.1. The Processes of using the positive mask and etching the electrodes on the surface…………………………………………………………………...54
      3.2.2.2.2. Negative mask design with PR shaping via optical lithography and application of lift-off method……………………………………………………………55
      3.2.2.2.3. E-Beam lithography patterning with PMMA and application of lift-off method……………………………………………………………………..57

4. RESULTS……………………………………………………………………..62

4.1. Fabrication………………………………………...………………………………....62
4.2. Simulation……………………………………………………………………………..68

5. DISCUSSIONS AND EVALUATIONS……………………………………….77

6. CONCLUSION………………………………………………………………..78

REFERENCES………………………………………………………………......81

ÖZET

ÖZGÜN BİR LAMB DALGASI CİHAZI TASARIM FABRİKASYON VE KARAKTERİZASYON ÇALIŞMALARI

Önerilen Lamb Dalgası Cihazı, klasik yapıda olduğu gibi, ince film üzerinde gecikme hattının iki ucuna karşılıklı olarak yerleştirilmiş iki “InterDigital Transducer” yapısı içermektedir. Bununla birlikte klasik yapıdan farklı olarak, gecikme hattının üst bölümüne bir kapasitif transdüser yapısı yerleştirilmiştir. Bu yapı gecikme hattına mekanik gerilme uygulayabilmektedir. Kapasitif Transdüser yapısına DC potansiyel farkı uygulandığında oluşturulan elektrostatik kuvvet gecikme hattını potansiyelle orantılı olarak aşağıya çekip bükmektedir. Sonuç olarak gecikme hattı gerginliği uygulanan DC gerilimle orantılı olarak ayarlanabilir hale getirilmiştir. Uygulanan gerilme, gecikme hattı üzerinde yayılan Lamb Dalgası hızının değişimine yol açmıştır. Dolayısıyla giriş sinyaline ayarlanabilir bir faz uygulamak mümkün hale gelmiştir. Lamb Dalgası osilatörünün osilasyon frekansı da bu şekilde ayarlanabilir olmuştur. Mevcut Lamb Dalgası osilatör cihazları, ayarlama için kondansatör kullanmaktadırlar fakat kondansatör kullanımı osilatör devresinin lineerliğini bozacaktır. Bizim yaklaşımımız kondansatör gereksinimini yok etmektedir, dolayısıyla osilatörün lineerliğine ve kararlılığına olumlu etkide bulunmuştur. Osilatörün kullanıldığı modülasyon katının da kararlılığı ve lineerliği arttırılmış olacaktır.

Lamb Dalgası cihazı askıda kalacak şekilde oluşturulmuş bir yapıya sahip olduğundan, Q-faktörü daha yüksektir ve ince-film kullanımı çok daha büyük bir faz hızı sağlar. Yüksek faz hızları da yüksek frekanslara çıkabilmeyi sağlamaktadır. Ek olarak, Lamb Dalgası cihazları SAW cihazlara kıyasla yüksek hassasiyet sağlar ve düşük faz hızına sahip özel Lamb Dalgası modları düşük frekanslarda da çalışmaya olanak tanır. Lamb Dalgasının faz hızı sıvı içerisinde yayılarak olduğundan da düşük hale getirilebilir. Bunlar, düşük kayıplı çalışmaya olanak tanır ya da sıvıların sınıflandırılmasında kullanılabilir. Azalan incelik nedeniyle Lamb Dalgası cihazlarının ısı kapasitesi oldukça düşüktür.

Bu projede yeni Lamb Dalgası cihazına ilişkin teori ve benzetim çalışmaları gerçekleştirilmiştir, belirlenen tasarım parametrelerine göre fabrikasyon yapılmış ardından fabrikasyonu yapılan cihazlara ilişkin test ve doğrulama çalışmaları gösterilmiştir.

ABSTRACT

DESIGN FABRICATION AND CHARACTERIZATION STUDIES OF A NOVEL LAMB WAVE DEVICE

The proposed Lamb Wave Device includes two “InterDigital Transducer” structures placed opposite each other on the two ends of the delay line on the thin film, as in the classical structure. However, unlike the classical structure, a capacitive transducer structure is placed in the upper part of the delay line. This structure can apply mechanical stress to the delay line. When DC potential difference is applied to the Capacitive Transducer structure, the electrostatic force created pulls and bends the delay line proportionally to the potential. As a result, the delay line tension was adjusted proportionally to the applied DC voltage. The applied stress causes a variation of the velocity of the Lamb Wave propagating on the delay line. Therefore, it is possible to apply an adjustable phase to the input signal. The oscillation frequency of the Lamb Wave oscillator is also adjustable in this way. Current Lamb Wave oscillator devices use capacitors for tuning, but the use of capacitors degrade the linearity of the oscillator circuit. Our approach eliminates the need for capacitors, so it has a positive impact on the linearity and stability of the oscillator. The stability and linearity of the modulation stage in which the oscillator is used also be increased.

Since the Lamb Wave device has a suspended structure, the Q-factor is to be higher and the use of thin-film provides a much greater phase velocity. High phase velocities also enable to reach high frequencies. In addition, Lamb Wave devices provide high sensitivity compared to SAW devices, and special Lamb Wave modes with low phase velocity allow operation at low frequencies as well. The phase velocity of the Lamb Wave can also be made lower than it is by propagating in the liquid. They allow low loss operation or can be used to classify liquids. Due to the reduced thinness, the heat capacity of Lamb Wave devices is quite low.

In this project, theory and simulation studies of the new Lamb Wave device were carried out, fabrication was carried out according to the determined design parameters, and then test and verification studies on the fabricated devices were demonstrated.

This research is supported by TUBITAK, grant number: 215E098

LIST OF SYMBOLS

$\mathbf{R_m}$: Motional impedance (Ω)

λ : Wavelength (*µm*)

Q : Quality

$\mathbf{A_x, S_x}$: Lamb wave modes, x: 0,1, …

$\mathbf{Y_{11}}$: Reflection admittance (*1/*Ω)

t : Time (*s*)

d : Film thickness (*nm*)

L/H : Membrane length/Transducer depth

ω : Angular frequency (*rad/s*)

ϕ : Amplitudes of wave (*V*)

$\mathbf{P_{11}, P_{22}}$: Reflection coefficient

$\mathbf{P_{12}, P_{21}}$: Transmission coefficient

$\mathbf{P_{13}, P_{23}}$: Electro-acoustic transfer function

$\mathbf{P_{31}, P_{32}}$: Coefficients that determine the efficiency of converting acoustic waves to current

$\mathbf{P_{33}}$: Admittance coefficient that determines the current flowing from the electrodes

f : Frequency (*Hz*)

C_p : Phase velocity (*m/s*)

C_T : Shear wave velocity (*m/s*)

C_L : Longitudinal wave velocity (*m/s*)

E : Modulus of elasticity (Young's Modulus) (N/m^2)

v : Poisson Ratio

ρ : Density (kg/m^3)

K : Wave number

$\mathbf{t_{step}}$: Simulation calculation time interval

y_{max} : Amount of precipitation

$2b$: Upper electrode width

L : Simulation calculation time interval

w : Distributed load (*Nt/m*)

a : Distance between the IDT input port and the beam fixation point

I : Moment of inertia

y : Spring constant

F : Electrostatic force

k : Constant

V : Voltage value

g : Distance between capacitive actuator plates

g_0 : Distance at rest position (V=0)

ε : Dielectric constant of the material between the lower and upper electrodes

ε_p : Dielectric coefficient of the piezoelectric material

v_0 : Wave speed

m : Admittance of the delay line

K^2 : Electromechanical transfer coefficient

M : Mass

V : Volume

$\varepsilon_{x, y, z}$: Amount of elongation

σ : Pressure

LIST OF ABBREVIATIONS

BAW	: Bulk Acoustic Waves
CMOS	: Complementary Metal Oxide Semiconductor
CMUT	: Capacitive Micromachined Ultrasonic Transducer
COM	: Coupling Of Modes
CT	: Capacitive Transducer
DI-Water	: Distilled water
DSP	: Double Side Polished
EBL	: Electron-Beam Lithography
FBAR/TFBAR	: Thin-Film Bulk Acoustic Resonators
FEA	: Finite Element Analysis
FEM	: Finite Element Modeling
FEM	: Finite Element Modeling
FIDT	: focused-IDT
IC	: Integrated Circuit
ICP-RIE	: Inductively Coupled Plasma – Reactive Ion Etching
IDT	: Inter-Digital Transducers
IF	: Intermediate Frequency
IPA	: Isopropyl alcohol
KOH	: Potassium Hydroxide
LW	: Lamb Wave
LWR	: Lamb Wave Resonator
MEMS	: Micro-ElectroMechanical System
NDT	: Nondestructive Testing
PECVD	: Plasma-Enhanced Chemical Vapor Deposition
PMMA	: Polimetil Metakrilat
PMUT	: Piezoelectric Micromachined Ultrasonic Transducers
PR	: Photoresist
PZT	: Lead-Zirconium-Titanium oxide
RF	: Radio Frequency
SAW	: Surface Acoustic Wave
SEM	: Scanning electron microscope

SIDT : Slanted-IDT

SNR : Signal-to-Noise Ratio

SOI : Silicon on insulator

TCF : Temperature Coefficient of Frequency

TMAOH : TetraMethyl Ammonium Hydroxide

UV : Ultraviolet

XRD : X-Ray Diffraction

LIST OF FIGURE

Figure 1: SIDT structure and equivalent model are shown. Here IDT plotted gaps are a function of frequency [53]……………………………………………………………………….8

Figure 2: Commonly used Lamb wave generator. It is seen here that the film thickness is close to the wavelength and the distance between two adjacent IDT fingers is the same as the wavelength. Finger metal thickness is one-quarter of the wavelength [67]……………………11

Figure 3: Representation of fundamental symmetrical (S_0) and fundamental asymmetric (A_0) lamb wave modes moving across the thin-film membrane [17]……………………………….12

Figure 4: Representation of the IDT structure as a three-terminal element [71]…………...….14

Figure 5: Calculated phase velocities of the first two Lamb wave modes comparing with the phase velocities of longitudinal, Rayleigh and shear waves propagating in an AlN membrane [17]………………………………………………………………………………………17

Figure 6: Illustration of capacitive transducer structure for tension-controlled membrane length tuning (a). Dimensions to be used for the electrostatic microactuator design (The design parameter that needs to be optimized here is the l/h ratio.) (b)……………………………...18

Figure 7: Illustration of the placement of the capacitive transducer (CT) element under the delay line and illustration of the working principle…………………………………………19

Figure 8: Schematic representation of Capacitive transducer (CT) structures placed between the IDT fingers……………………………………………………………………………...20

Figure 9: Mechanical equivalent of the proposed structure ……………………...………...21

Figure 10: The relationship between the distributed load applied to the film and the amount of LW delay……………………………………………………………………………...24

Figure 11: Illustration showing thin film and distributed load………………………………..25

Figure 12: A two-port SAW device built on a piezoelectric wafer (ST-Quartz) for a biosensor application. The transmission and reception IDT pair and the delay line between them are seen [75]………………………………………………………………………………………28

Figure 13: Demonstration of the installed COMSOL model. The drawing on the right is side view: Here, Si (500 μm), AlN (200-500 nm) and Cr electrode layers are shown, respectively...30

Figure 14: (Left) Displacement images got by 3D simulation, (Right) LW reaching receiver IDT……………………………………………………………………………………....31

Figure 15: Frequency response plots for 500 nm film thickness: (Left) linear scale, (Right) logarithmic scale……………………………………………………………………….....32

Figure 16: Impulse and frequency response plots for 400 nm film thickness, impulse response at the top, frequency linear scale in the middle, frequency logarithmic scale at the bottom…....33

Figure 17: Impulse (top) and frequency response (bottom) plots for 200 nm film thickness….34

Figure 18: Fabrication processes for electrode growth and thin film release…………………38

Figure 19: Electrode enlarged AlN coated SOI wafer …………………………….…………39

Figure 20: (Left) View before and after (Right) Si3N4 coating with PECVD ……………….…40

Figure 21: Mask to be used to open Bulk-Etch areas 40

Figure 22: Surface shaped by PR after photolithography 41

Figure 23: Structure with Si3N4 and SiO2 obtained as a result of the first ICP-RIE 41

Figure 24: Structure with Si3N4 and Si obtained as a result of the first ICP-RIE 42

Figure 25: Bottom views of fragmented 33 MHz (Left) and 100 MHz (Right) LW devices, before bulk-etching. The outer frame is Si3N4, the middle section is Si..........................43

Figure 26: High temperature etching setup: at 90°C, 20% KOH and no IPA.........................43

Figure 27: Etching of unwanted areas..44

Figure 28: Profilometer result of sample left for 1 hour 45 minutes at 90°C, 20% KOH, non-IPA solution..45

Figure 29: Profilometer results for samples etched for 19 hours 20 min at room temperature: 30% KOH (Left), 20% KOH (Right)...46

Figure 30: Top and bottom view of the resulting LW device 46

Figure 31: Side and top view of the 43.750 nm AlN coating..47

Figure 32: Side and top view of the 100 nm AlN coating 48

Figure 33: Top view of the 200 nm AlN coating..48

Figure 34: Crystal orientations of the structure consisting of 100 nm AlN thin film layer coated on Si(111) obtained by XRD device 50

Figure 35: Crystal orientations of the structure consisting of 100 nm AlN thin film layer coated on Si(111) obtained by XRD device...51

Figure 36: The test setup connected to the network analyzer of the thin film obtained as a result of fabrication...51

Figure 37: Obtained thin-film electrical characterization results. Magnitude plot of the S21 response at the relevant frequency 52

Figure 38: Obtained thin-film electrical characterization results. Phase plot of the S21 response at the relevant frequency...53

Figure 39: The positive mask we used in the lithography process (Right). Sample (Left) coated first with Cr, then PR and shaped by lithography 54

Figure 39: The positive mask we used in the lithography process (Right). Sample (Left) coated first with Cr, then PR and shaped by lithography 54

Figure 40: Example set to connect to network analyzer after Cr Developer 55

Figure 41: Example set to connect to network analyzer after Cr Developer.......................56

Figure 42: Image after cleaning of the sample damaged by the developer: Dissolved AlN (Brown) and undissolved AlN (Blue)...56

Figure 43: Ellipsometer device and measurement result..57

Figure 44: Wafer during the cutting process 58

Figure 45: Ellipsometer device and measurement result..57

Figure 46: (Left) Dummy wafer plate used for coating. (Right) Wafer pieces after coating......59

Figure 47: Microscope images after Cr coating………………………………….……......….59

Figure 48: Acetone bath ………………………………………………………………......….60

Figure 49: (Left) Sample after Cr coating process, (Middle and Right) microscope images….60

Figure 50: IDT electrode enlarged sample with success after lift off ……….…………......….61

Figure 51: Microscope images of successfully magnified samples of the IDT electrode.....….61

Figure 52: Demonstration of the circuit assembly to be set up to measure the LW speed……..63

Figure 53: Fabrication processes of the Adjustable-Phased Lamb Wave Device via Analog-Voltage-Controlled………………………………………………………………………………64

Figure 54: The final version of Cr IDT coated LW device after EBL….……………………...65

Figure 55: Si layer with SiN framework to be wet-etched with KOH………………………...66

Figure 56: (a) The transmission characteristics of the classical LW device and (b) the adjustable delay line LW device using a spectrum analyzer and (c) the transmission characteristic of the classical two-terminal SAW device with a design frequency of 16.8 MHz manufactured on a piezoelectric (ST-Quartz material) wafer…………………………………………………..67

Figure 57: Element mesh representation of the 3D model (upper left). The progression of the Lamb Wave in the established model (upper right). Section (bottom) used in 2D simulation studies to reduce simulation time and complexity……………………………………………..68

Figure 58: Dispersion curve obtained by numerical solution of Rayleigh-Lamb Equations. This curve is obtained for LW A0 mode using f=100 MHz and AlN film mechanical properties…..69

Figure 59: (a) 3D representation of IDT electrodes. (b) The view after meshing …………….70

Figure 60: Constructed model and IDT fingers with measurements…………………………72

Figure 61: Stretching in the film with no distributed load (top) and 10 Kpa load (bottom) (stretching is exaggerated for clarity). Progression of the generated single cycle lamb wave…72

Figure 62: Output voltages read for various distributed load values between 0-10 kPa………73

Figure 63: Phase differences read in output voltage for various distributed load values between 0-10 kPa. It is seen that the phase differences-distributed load relationship is almost linear…..74

Figure 64: Network Analyzer results for the manufactured device, Center Frequency is 55 MHz……………………………………………………………………………………..75

Figure 65: Phase change of the Center Frequency ……………………………………..…..76

LIST OF TABLES

Table 1: Simulation parameters of the model established for the preliminary simulation studies…………………………………………………………………………………………30

Table 2: Simulation parameters of the model established for the preliminary simulation studies…………………………………………………………………………………………70

LIST OF SCHEMATICS

Schematic 1: Fabrication steps for bottom structure……………………………………………79

Schematic 2: Fabrication steps for top structure, and the schematic of the final form………...79

1. INTRODUCTION AND OBJECTIVES

1.1. General Information And Applications

The small-in-size and Complementary Metal Oxide Semiconductor (CMOS) compatible Micro-ElectroMechanical System (MEMS) resonators are likely to be the driving core of a new generation of devices such as Radio Frequency (RF) filters and timing references [1], [2]. Thanks to the CMOS compatibility, ability of high frequencies, low motional-impedances (R_m) and capability of multiple frequencies operation on a single chip, the Lamb Wave (LW) resonators have attracted attention among micromechanical resonator technologies [3], [4].

LW devices are formed by depositing two comb-shaped transmit/receive electrodes with many fingers interdigitated on a thin (<< Wavelength (λ)) piezoelectric membrane [5]. These comb-shaped structures are called InterDigital Transducers (IDT). LW devices can have only one-port or two-port (input/output with 2 terminals), which are the ports for transmitting and receiving the wave. There is a delay line in between these ports to apply a phase to the input signal [6]. Although an IDT structure can generate or sense acoustic waves, it cannot control the wave properties like velocity or frequency because these parameters are lithography defined. The first LW device was realized by Toda in 1973, and he employed a thin film Lead-Zirconium-Titanium oxide (PZT) plate [7]. The first practical LW Resonator device was developed by Piazza and Yantchev in 2002 [3], [8].

The LW modality is attractive for researchers since it has certain advantages over existing Surface Acoustic Wave (SAW) technology. Since the LW device has a suspended structure, the Q factor will be higher, and thin-film utilization enables larger phase velocity. LW devices have higher sensitivity than SAW devices, use of low-velocity lamb wave allows the device to operate at low frequency, the velocity can be made lower than the velocity of the dispersed wave in most of the common liquids, that's permitting low loss operation, heat capacity is low because of the reduced thickness or it may classify liquids [9]. After the first realization of practical LW devices, they can find a place in the market. Since the 4G and higher GSM devices like phones or base stations require high-frequency filters (RF, 4-5 GHz) in their RF or IF (Intermediate Frequency) sections, the LW resonators have the potential to be used in the telecommunication industry [10]-[12].

The proposed Lamb Wave Device includes two “InterDigital Transducer” structures placed opposite each other on the two ends of the delay line on the thin film, as in the classical structure. However, unlike the classical structure, a capacitive transducer structure is placed in the upper part of the delay line. This structure can apply mechanical stress to the delay line. When DC potential difference is applied to the Capacitive Transducer (CT) structure, the electrostatic force created pulls and bends the delay line proportionally to the potential. As a result, the delay line tension was adjusted proportionally to the applied DC voltage. The applied stress causes a variation of the velocity of the Lamb Wave propagating on the delay line. Therefore, it is possible to apply an adjustable phase to the input signal. The oscillation frequency of the Lamb Wave oscillator is also adjustable in this way. Current Lamb Wave oscillator devices use capacitors for tuning, but the use of capacitors degrade the linearity of the oscillator circuit. Our approach eliminates the need for capacitors, so it has a positive impact on the linearity and stability of the oscillator. The stability and linearity of the modulation stage in which the oscillator is used also be increased.

Besides this, it is possible to use LW devices as measuring for physical quantities, like biosensors, gas sensors, or Nondestructive Testing (NDT) equipment. Increased sensitivity, compatibility with IC (Integrated Circuit) technology, low cost, the simple and stable structure of an LW device make the researchers attracted to these devices [1], [13]-[16].

In this project, theory and simulation studies of the new Lamb Wave device were carried out, fabrication was made according to the determined design parameters, and then test and verification studies on the fabricated devices were demonstrated. Acoustic filter simulation studies and experimental studies have been presented as a sample application within the scope of the project. The proposed LW device includes 2-IDT structures placed opposite each other on both ends of the delay line on thin film, as in the conventional structure. LW devices are new compared to SAW devices as LW devices have just been implemented thanks to recent advances in microfabrication technology.

1.2. Brief History

Acoustic waves have been used in various industrial, military, and medical applications for many years, especially SAW devices produced on piezoelectric wafers have been widely used because of the high electromechanical transmission coefficient and low acoustic loss value they provide. The most important advantage of SAW devices used in many applications is that they provide delay lines and long delays in small areas because of their low acoustic speed value. In recent years, the potential of using LW devices instead of SAW devices have been investigated with many studies. This is because LW devices provide monolithic IC integration and advantages such as high Q factor, high frequency, and adjustable wave speed. It has also been shown that the use of LW increases sensitivity [17].

Briefly, if we talk about the historical development on this subject, surface waves were first shown on isotropic material by Lord Rayleigh in 1885 [18]. While studying seismic signals, Rayleigh noticed that there was another wave component that came later after the expected post-shock waves. This signal was moving slower and was stronger than it should have, as it radiates only from the surface (2-dimensional). Later, Love, also a geologist interested in seismic activity, reported a new type of wave that propagated at the surface but particles moved in another direction [19]. In Rayleigh waves, the particles move in the plane that includes the surface normal and the wave propagation direction, whereas in Love waves the particle motion is perpendicular to this plane. Love also showed that Rayleigh waves are only on layered systems. Subsequent studies have shown that surface waves can have many modes [3], [8], [20], [21]. In 1917, British mathematician Horace Lamb mathematically showed that another type of wave (Lamb Wave) propagating on a very thin plate must be physically found [22]. He investigated the surface waves in an infinitely long two-dimensional elastic plane and presented the numerically solvable equations known as Rayleigh-Lamb Equations. In study, lamb wave was produced on PZT ceramic plate, and biosensor applications were developed using lamb wave devices produced with ZnO in subsequent studies [20].

The IDT structure as a nested comb was operated by White and Voltmer and its use became widespread rapidly [6]. Before this date, it was known that a dispersive filter that applied different amounts of delay to different frequencies could provide significant improvements in radar applications, but the dispersive-LC filters to realize this took a lot of space and had no practical application [17]. That SAW waves are almost 100 times slower than electromagnetic waves shows that the desired result can be achieved with SAW technology. In 1969, Court proposed this practice using delay lines and Love waves [23], an idea experimentally showed by Mortley [24]. These developments make up the starting point of SAW devices. In the following years, research continued on topics such as piezoelectric materials, propagation effects, transducer analysis, and design techniques.

From the 1970s to the mid-1980s, the vast majority of efforts in this area focused on military applications, especially radar and communication applications [25]. After that, especially with the widespread use of portable phones, SAW devices have found their place in consumer electronics applications with their low cost, low-loss values, and small dimensions. In the communication industry, SAW devices are mostly used as band-pass filters in RF and IF levels [10]-[12]. In recent years, some observe that SAW devices are used with increasing frequency for sensor applications. Sensor applications are based on the principle that the change to be felt affects the mechanical properties of the delay line and the change that this effect will cause in the phase of the acoustic wave. SAW devices can be found as sensors in the automotive industry (torque and tire pressure measurement), biomedical applications, and various industrial applications (such as temperature, humidity, gas concentration measurement) [26]. Besides, SAW devices are used in applications such as pumping, mixing, particle separation, and flow rate detection in micro fluids [27]-[35].

LW propagating on AlN thin film are an area of interest because LW has the advantages of SAW and Thin-Film Bulk Acoustic Waves (BAW) (Thin-Film Bulk Acoustic Resonators (FBAR/TFBAR) is produced) [36]. The frequencies of LW devices are lithographically defined as in SAW devices, and they have low loss and high Q factor thanks to the thin film. Although LW devices have advantages over SAW technology such as high precision and more stable structure, they develop over the applications created by SAW technology. LW devices, like SAW devices, are suitable for sensor and communication applications but show a higher level of performance. In this study, a novel structure is presented to increase the application potential for LW devices.

1.3. Literature Studies

If we examine the literature on the current status and applications of LW devices, Wenzel S.W. carried out by. In this study, LW characteristics were got analytically, and how the LW parameters were changed by physical quantities was discussed [21].

Physical quantities are possible to measure using the LW oscillator structure: 1. It will be possible to apply biosensor and chemical gas sensors if the phase velocity depends on the mass on the film and the film thickness (much smaller mass changes can be detected compared to SAW). 2. Acoustically, the sound waves can modulate membrane tension and hence LW velocity by making the membrane vibrate. This response of the LW device to the membrane tension will also allow the measurement of the applied force.

Membrane tension is also used for pressure measurement. Immersing the LW device in a liquid reduces the speed radically depending on the mass and density of the liquid on the device, and the change is linear with density [37]. Although this study provides a general perspective for all areas, details have not been addressed. For example, the mass and density measurements of the liquid were made together, but the shares of these two sizes in the measurement were not clarified.

Zhou L. et al. By evaluating the responses of different Lamb modes (A_{01}, A_{03}, S_0, and A_0) to the liquid, he could measure mass and density sizes separately and used this information for the classification of liquids [38].

Another study in which liquid properties were determined using LW was carried out using LW S_0 mode and FBAR [39]. In this study, LW and film bulk acoustic resonators were investigated by simulation studies, and it was shown that fluidity (viscosity) can be measured and the density of the liquid. An interesting LW application reported in the literature is the measurement of the liquid level inside the tanks under high pressure from the outside of the tank [40]. In this application, Lamb waves are produced on the tank and interact with the liquid in the tank, and the liquid level is determined by using this interaction.

In another study carried out for mass measurement, a MEMS structure with dimensions of 1mmx1mm was used, and GaN was chosen as the piezoelectric material in the production of this structure [41]. With its high thermal, mechanical, and chemical stability, GaN can enable MEMS structures to be operated in harsh environments. Besides, compatibility with GaN-based integrated circuits is emphasized in this study.

Lamb waves are also used for NDT of very fine materials [42]-[45]. Studies in which the behavior of emitted Lamb waves in the damaged area is visualized by laser interferometry have been reported in the literature.

A study investigating the propagation of Lamb waves on an aluminum plate and analytically and experimentally showing the velocity change under stress was carried out by Michaels J.E. [46]. The experiments were carried out for 250 kHz (A_0 mode), 400 kHz (A_1), 600 kHz (S_1) frequency (modes) using an aluminum plate with a size of 30 x 60 cm and a thickness of 6.35 mm. 5.75 MPa increments for 0-57 MPa tensile values. Theoretical and experimental speed changes were got and compared.

Other important experiments were conducted to investigate the velocity change of the directed wave under stress and interesting results were got [26], [47], [48]. According to the result got in the study, this effect appears as a speed that increases with stress before a critical angle value, but as a speed that decreases with stress afterward. Perhaps the most important application area for LW devices is LW resonators. Stability in filter, modulation, and oscillator applications, high Q factor, and low cost, MEMS resonators have an important application potential, especially in telecommunications. Especially LW devices allow stable resonator structures at very high frequencies thanks to their adjustable wave velocity and different symmetrical wave modes. The LW resonator using lithium niobate Kadota M. Ver et al. It has been successfully operated by 4.5 and 6.3 GHz frequencies [49]. These structures, which can find wide application areas especially in advanced generation GSM communication devices, have made rapid progress in the last decade with the effect of the developments in micro-processing technology. Especially the structures of LW devices that combine the advantages of FBAR and SAW technologies show that LW resonators will be used effectively in the future.

Yantchev V., LW devices using longitudinal wave, bottom surface grounded, and ungrounded IDT structures were compared in terms of their performance [14], [50]. The reflection admittance (Y_{11}) of the LW device got by using the IDT whose bottom surface is not grounded shows 20 dB lower performance than the others, while this parameter is close in the other two cases, but the SNR performance of the LW device is better. The LW device was fabricated and the Q factor was measured as 3000 at 900 MHz operating frequency. Also, a phase-shifting MEMS filter was produced for a 2-port LW device at the same frequency, signal attenuation was measured as <10 dB at the design frequency. This attenuation value is considerably lower compared to SAW filters. In this study, a filter was used within the oscillator structure and the phase noise generated by the temperature was investigated since the temperature sensitivity of the AlN coating is known. As a result, for 900 MHz, while producing a 27 dBm output signal, phase noise was determined as -92 dBc. Although this value does not pose a problem for the oscillator application, it is possible to reduce the phase noise by using the structure we propose and will be an important contribution to the literature. In his study, Yantchev examined the mass and pressure measurement performances of the LW oscillator with its 900 MHz frequency design, showed that high sensitivity measurement can be made, and revealed that the film thickness and sensitivity are inversely proportional.

In all these studies, the LW frequency and velocity are fixed and specified in the design, such as the IDT type [27], length, aperture, and delay line length. However, the adaptive control of these parameters will contribute to the literature in many areas such as reducing the phase noise (hence, temperature sensitivity compensation for example) or controlling the working band of the filter by changing the center frequency.

In the next section, the previous literature on IDT structure and SAW devices will be presented, emphasizing the contributions of our new approach.

1.3.1. Studies on the band of the filter

One of the first studies carried out after the IDT structure has been proposed, proposes the SIDT (Slanted-IDT) structure and aims to realize more broadband filters with excellent characteristics. This structure, which was conceptually proposed in 1969 [51], was first produced and tested in 1973 [52].

As it is known, IDT structures are designed for a single frequency by setting the distance between fingers as λ, so the filter got is a narrow band. The SIDT structure changes the finger distance along with the IDT aperture, thus the same SAW device generates signals at over than one frequency (Figure 1) [53]. Practically it can be thought of as many IDT devices generate signals at neighboring frequencies along with the IDT opening. This structure is used in several circuits today, and broadband LW and SAW filter applications (SIDT) are an active research area [53], [54].

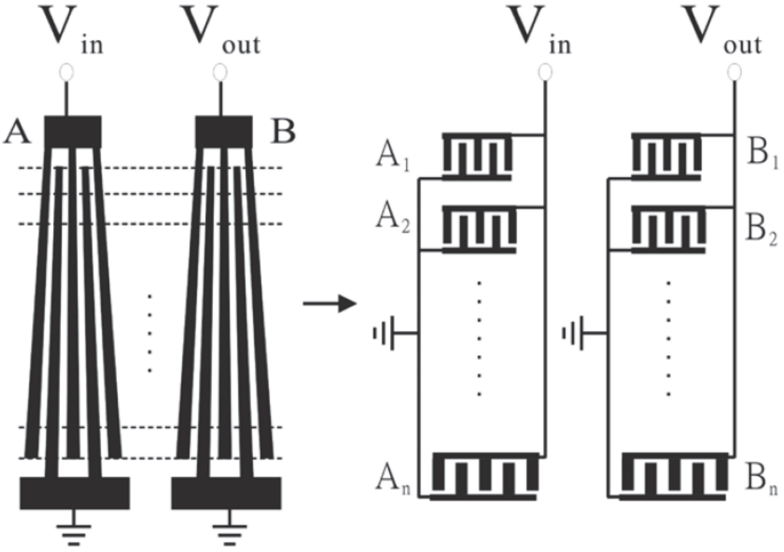

Figure 1: SIDT structure and equivalent model are shown. Here IDT plotted gaps are a function of frequency [53].

Another example of a working band that mimics the function of these types of filters is filter banks. These structures, which contain over than one filter designed for a single frequency, can single-input / multi-outputs, and designs with single input / single-output and selective inputs. Using these structures, the center-frequency can be shifted discretely. Mobile phones with multiple bands have areas of use such as band-pass filters in the RF layer and minimizing overlap errors in reconstruction filters [55]-[58].

1.3.2. Adjustable frequency oscillator design

The high Q factor and low loss structure of LW and SAW devices, as well as the structural determination of the oscillation frequency, have led to the widespread use of these devices in oscillator designs. The adjustable frequency oscillator circuit is implemented by the physical switches [59]-[61]. The biggest handicap in these circuit designs is that phase noise affects oscillation stability. This problem, especially in sensor applications, affects stable biosensor measurements due to the phase noise that occurs during the reaction in the delay line [62], [63]. The proposed structure can eliminate phase noise, thus increasing stability.

1.3.3. Adjustable phase SAW – LW filter / SAW – LW phase modulation

Tunable phase filter applications are found in many beamformer circuits, oscillator circuits, or general-purpose filtering circuits. The tunable phase LW filter we recommend will provide convenience in many communications, radar, and biomedical applications, with its high Q factor and high center frequency [64]-[66].

1.4. The Motivation For This Thesis Work

The aim of thesis was to create a unique Lamb Wave device, thus bringing novel approaches to LW filter and sensor applications. In the original LW structure, we propose, our aim is to adjust the tension of the delay line using a potential difference and in this way to make the phase characteristic of the LW device adjustable. We collect the studies we aim to achieve this goal under 3 main headings:

1.4.1. Material characterization

Our goal in these studies is to make the electrical and acoustic characterization of the material to be used in the design be used in Finite Element Modeling (FEM) studies. With this study, the important parameters related to the materials to be used determined precisely (For example, LW Speed on Aluminum Nitride (AlN) film) allows more reliable results from the simulation studies.

1.4.2. Theory and simulation studies

In these studies, the aim is to determine that the designed structure works as desired, as well as to determine its characteristics, limits, and efficiency parameters without fabrication. Thus, the number of remanufacturing has been reduced, and the productivity and cost of the work has been positively affected. The properties obtained by FEM studies were used in post-production validation studies. In addition, the ability of the CT structure to manipulate the center frequency of the LW resonator device was investigated by simulation studies.

1.4.3. Fabrication testing and verification studies

The proposed LW structure has been revealed in these studies and it has been tested whether the device works as desired. The characteristics obtained in simulation studies have been experimentally obtained by using the fabricated device. The application potential of the new LW device has been explored.

2. GENERAL BACKGROUND

2.1. Lamb Waves

Lamb waves are generated by directing acoustic waves laterally into a sufficiently thin plate (thickness << wavelength) [5]. For the production of lamb waves, metal electrodes as interlocking combs are deposited on a very thin piezoelectric surface. When an RF signal at design frequency applies to these electrodes, the lamb wave at that frequency is propagated across the plate (Figure 2) [67].

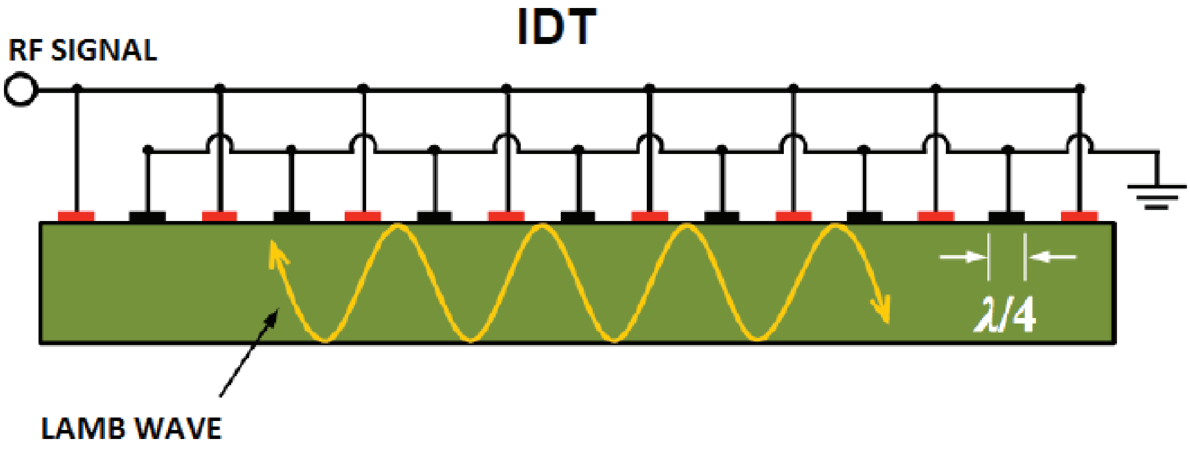

Figure 2: Commonly used Lamb wave generator. It is seen here that the film thickness is close to the wavelength and the distance between two adjacent IDT fingers is the same as the wavelength. Finger metal thickness is one-quarter of the wavelength [67].

There is over one lamb wave mode, and these modes usually only displace the axes (x and z) perpendicular to the direction of travel and the direction of travel. This type of wave is divided into two major groups as symmetric or antisymmetric modes according to the symmetry of particle motions around the midplane of the plate (Figure 3) [17].

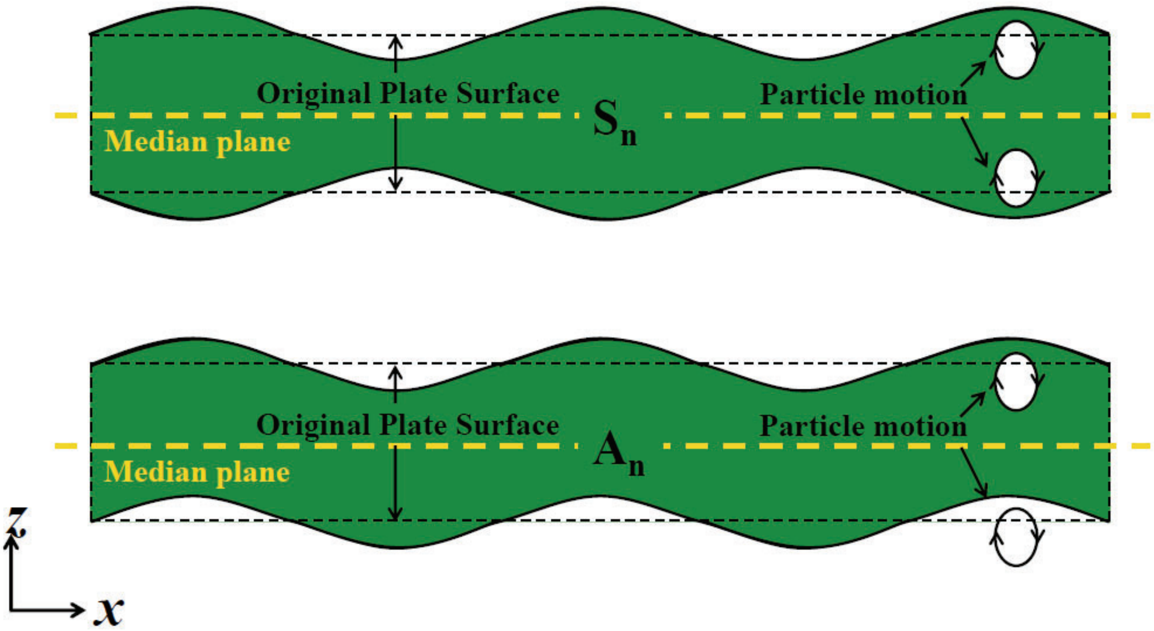

Figure 3: Representation of fundamental symmetrical (S_0) and fundamental asymmetric (A_0) lamb wave modes moving across the thin-film membrane [17].

The unique structure we propose in this study enables a more controlled LW device design by providing the possibility to adjust the voltage in the delay line. Such a device will not only facilitate many communication and sensor applications but also has the potential to create new applications where LW devices are not used yet. In our study, basically, a 2-port LW device delay line using classical IDT structures is fabricated as bendable and stretchable, so that the phase change of the acoustic wave becomes adjustable.

2.2. IDTs

The first model developed for IDT structures is the Delta Function Model. This model is built on a simple and easy-to-understand principle. When voltage applies to the IDT electrodes, an instantaneous charge accumulates and this charge will accumulate at the edges of the IDT fingers because of the constantly changing polarity between neighboring IDT fingers. In this model, the load distribution on IDT fingers is represented by the Discrete-Delta Functions [68]. The amplitude of the Delta Function is directly proportional to the amplitude of the applied voltage. The response of the IDT to the applied voltage is got by summing the delta functions in the IDT fingers. The delta function model produces output based on the calculation of relative attenuation and can provide quite adequate information about bandwidth, side-lobe level and locations, and suppression levels. The absence of impedance levels and second-order effects in the model creates inadequacy for many applications [69].

Another technique used in IDT modeling considers incoming and reflected waves and is called the Coupling Of Modes (COM). Reflections from obstacles with a weak reflectance coefficient are not considered. These two waves propagate towards each other and it is assumed that the amplitudes (Wave Amplitudes and associated Current and Voltage Amplitudes) will be combined linearly. The spatial variation of the amplitude of these two modes and the current and voltage generated at the electrodes are defined by a first-order linear differential equation. COM equations are arranged by Tobolka using the 'P' matrix, and this matrix evaluates the IDT structure as an element with 3 ports [70]. Two of these refer to the acoustic wave propagating in opposite directions, the third is the electrical port where the input voltage is applied (Figure 4) [71]. Here, the boundary conditions are given as the applied voltage (V), the amplitudes of the incident waves as $\phi^+(x_1)$ and $\phi^-(x_2)$, respectively. The response of IDT is the current (I) flowing through the electrodes and reflected waves in amplitudes $\phi^-(x_1)$ and $\phi^+(x_2)$.

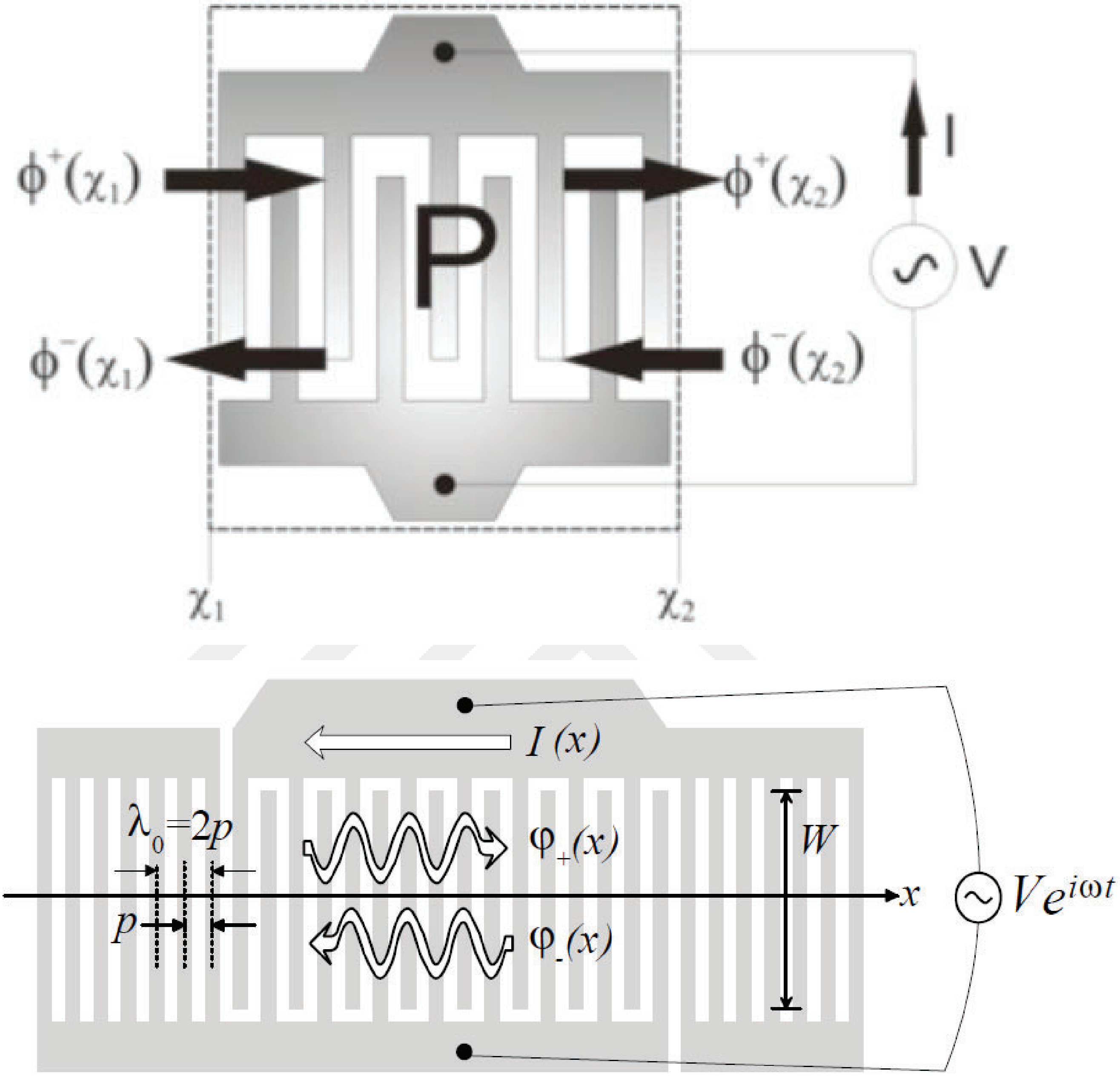

Figure 4: Representation of the IDT structure as a three-terminal element [71].

The relation which relates the boundary conditions of the IDT structure with the response of the device and the expression given with the 'P' matrix (1). Here, the coefficients in the 'P' matrix are: $P_{11} = P_{22}$ reflection coefficient and $P_{12} = P_{21}$ transmission coefficient, and the remaining coefficients represent the electrical properties of the device. P_{13} and P_{23} are the electro-acoustic transfer function of IDT, P_{31} and P_{32} are the coefficients that determine the efficiency of converting acoustic waves to current, and P_{33} is the admittance coefficient that determines the current flowing from the electrodes because of the applied voltage.

$$\begin{bmatrix} \varphi_-(x_1) \\ \varphi_+(x_2) \\ I \end{bmatrix} = \begin{bmatrix} P_{11} & P_{12} & P_{13} \\ P_{21} & P_{22} & P_{23} \\ P_{31} & P_{32} & P_{33} \end{bmatrix} \begin{bmatrix} \varphi_+(x_1) \\ \varphi_-(x_2) \\ V \end{bmatrix} \qquad (1)$$

The biggest advantage of this model is that it allows modeling different IDT structures together. A 'P' matrix can be generated for each IDT structure and the entire design can be expressed with a single 'P' matrix. Besides, to use the COM model, the transducers and reflectors of the LW device to be simulated must be able to be divided into uniform periodic parts. The Equivalent Circuit Model, another modeling technique, uses a technique close to the 'P' matrix [72], [73]. The two acoustic ports in the COM model have been converted into their electrical equivalent in the equivalent circuit model. In this model, the boundary conditions are applied-voltages, and the response generated by IDT is the generated-currents. Thus, the boundary conditions are linked to the IDT response by an admittance matrix. The electrical parameters of the equivalent circuit are calculated depending on parameters such as wave velocity, electromechanical coupling coefficient, center frequency, number of fingers in the IDT.

2.3. Lamb Wave Devices

The basic design parameters of LW devices can be listed as design frequency, the thickness of film coating, wave velocity, and wavelength. The basic design parameter of IDT structures is the wavelength and is determined by the distance between two neighboring finger-shaped electrode extensions. The distance between two neighboring fingers is a wavelength (λ) and the wavelength connects the frequency (f) and phase velocity (C_p) of the acoustic wave to be produced by the relation $C_p = \lambda.f$. The velocity of the lamb wave over the surface C_p is calculated by solving the Rayleigh-Lamb equations in equations (2), (3) and (4) for a specific f and film thickness (d).

$$\boldsymbol{for\ symmetrical\ modes}: S_n = \frac{\tan(qh)}{\tan(ph)} = -\frac{4K^2pq}{(q^2-K^2)^2};\ (\mathbf{2})$$

$$\boldsymbol{for\ asymmetrical\ modes}: A_n = \frac{\tan(qh)}{\tan(ph)} = -\frac{(q^2-K^2)^2}{4K^2pq};\ (\mathbf{3})$$

$$q = \left(\frac{w}{C_T}\right)^2 - K^2;\ p = \left(\frac{w}{C_L}\right)^2 - K^2;\ q = \frac{w}{C_p}; w = 2\pi f;\ C_p = \left(\frac{w}{\pi}\right)\lambda; h = \frac{d}{2};\ (\mathbf{4})$$

$$C_p = \frac{2\pi d}{\lambda}\sqrt{\frac{E}{12(1-v^2)\rho}}\frac{1}{\sqrt{\frac{\pi^2 d^2}{3\lambda^2}+1}};\ (\mathbf{5})$$

In these equations, ω is used for angular frequency, C_T shear wave velocity, K wave number, C_L longitudinal wave velocity, C_p phase velocity. Dispersion curves are got by calculations for different f and d values, and different C_p can be found in different wave modes for a certain $f * d$ value (Figure 5) [17]. The lowest order antisymmetric (A_0) and symmetric (S_0) modes are used. Using A_0 mode was aimed at our study. An approximate expression (5) is given for the speed value got by Rayleigh-Lamb equations, which can only be solved numerically. In this expression, d is the film thickness, E is the modulus of elasticity (Young's Modulus), v is the Poisson Ratio, and ρ is the density.

Apart from these parameters, dimensions such as the length of the delay line, the electromechanical transfer coefficient, the propagation mode of the acoustic wave to be produced, and the damping amount should be taken into consideration during the design. The number of fingers determines the band of the Lamb wave produced, and the metallization ratio between two fingers of an electrode determines the harmonic amount in LW. Studies have shown that a 50% metallization ratio between two adjacent fingers of an electrode (finger-widths should be 0.25λ) gives the optimum result in terms of the harmonic amount [74].

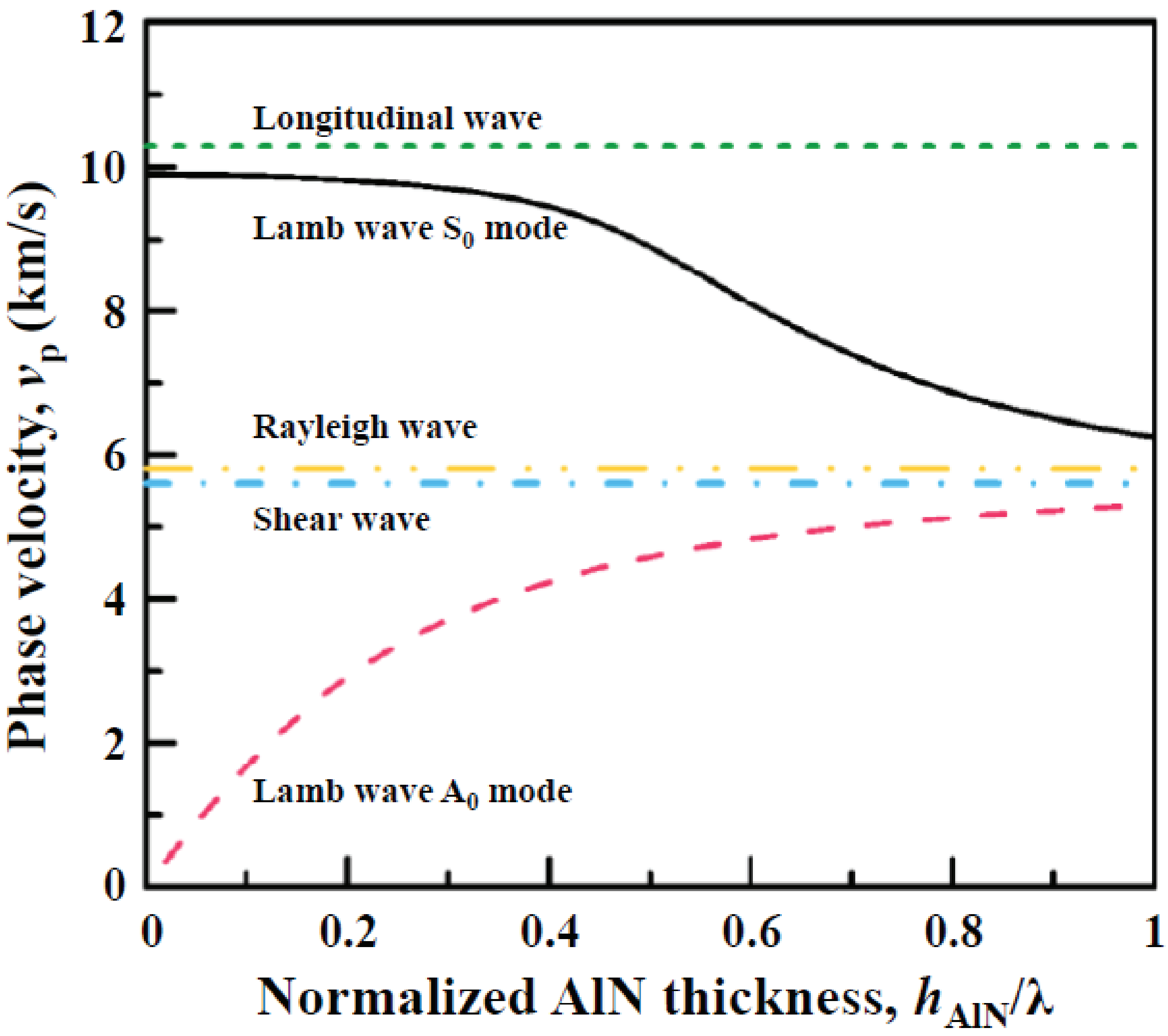

Figure 5: Calculated phase velocities of the first two Lamb wave modes comparing with the phase velocities of longitudinal, Rayleigh and shear waves propagating in an AlN membrane [17].

3. THESIS STUDIES

3.1. Methodology

LW device designs in the literature do not offer the possibility of adjusting both the distance between the fingers, which is the basic design parameter and the delay line distance, which determines the phase to be applied to the acoustic wave by the LW device. Our motivation in this thesis is to make these basic LW device parameters adjustable. For this purpose, the results of the capacitive transducer structure seen in figure 6 are presented in the simulation program. With a similar structure, it is possible to stretch the membrane section on the structure in proportion to the applied DC voltage intended, and thus to control the speed of the wave propagating on the membrane and the membrane length with a DC voltage. This stretching is accomplished by means of an electrostatic force that will be proportional to the applied DC voltage.

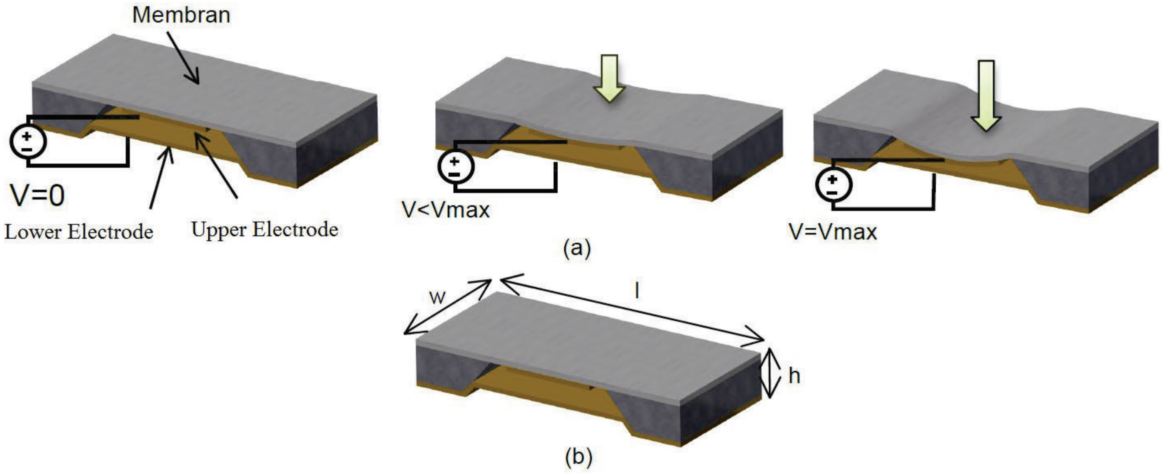

Figure 6: Illustration of capacitive transducer structure for tension-controlled membrane length tuning (a). Dimensions to be used for the electrostatic microactuator design (The design parameter that needs to be optimized here is the l/h ratio.) (b).

It is planned to place IDT structures on the membrane parts of the transducer structures as seen in Figure 6, thus creating LW waves on the membrane. This section will be suspended by using electrodes to be placed opposite the delay line. The length of the delay line stands out as a parameter that determines the phase range and should be determined according to the frequency and application to be used. There are values a few times the wavelength for the delay line length used in the literature [7], [11]. The most important parameter for CT structures that will provide adjusted delay is the membrane length/transducer depth (l/h) (Figure 6.b). This ratio is expected to be large enough to provide effective precipitation. As the ratio increases, the adjusted delay amount will decrease. This ratio can be increased to where the membrane does not deform when the membrane is elongated. The problem here is to make the optimum design with a maximum slump. It has been reported in previous studies that the Capacitive Micromachined Ultrasonic Transducer (CMUT) structure, which is a similar structure, can be precipitated at 1/3 of the maximum height (h) by using DC voltage. The amount of acoustic attenuation, which is another important parameter, varies depending on the type of piezoelectric material, the electrode material used, and the length of the delay line. Here, besides the length of the delay line is known as an effective parameter in the damping of the acoustic wave, other parameters can also have an important effect. Especially for the proposed LW device, it is necessary to examine the effect of the piezoelectric coating attenuating the acoustic wave while the membrane is in tension. In addition, the effects of membrane movement on the acoustic wave should be investigated (Figure 7).

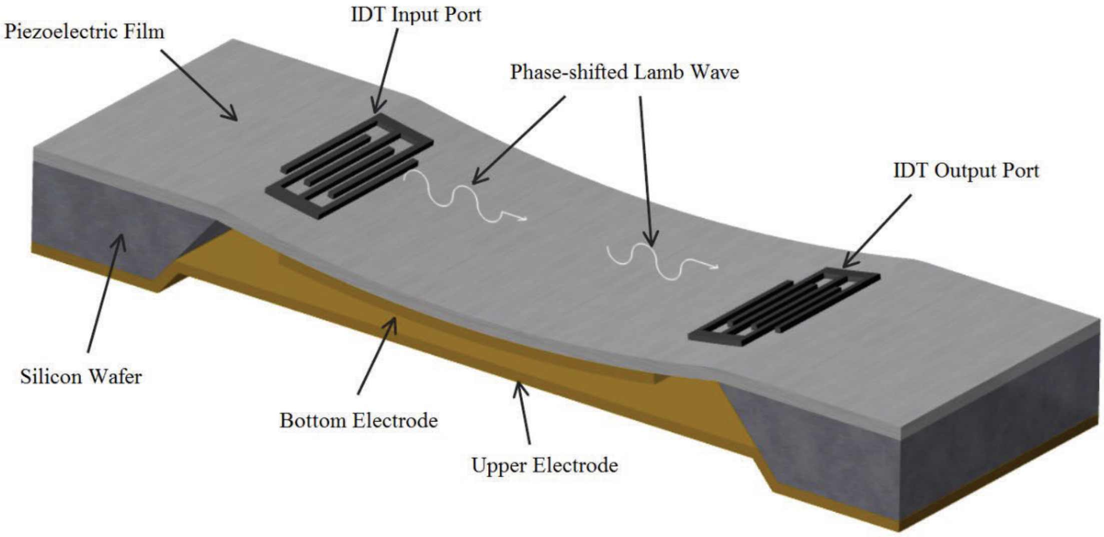

Figure 7: Illustration of the placement of the capacitive transducer (CT) element under the delay line and illustration of the working principle.

Within the thesis, theory, simulation, and fabrication studies were carried out for a 2-port LW device with an adjustable delay line. Produced device characteristics were got and verified with simulation results. The proposed LW device was produced by structurally composed of two blocks. These are 1. IDT pair enlarged on a conventional thin film for LW generation and reception, and a delay line between them, 2. It is the capacitive transducer structure to be placed on the delay line. The LW is delayed by the above-mentioned 3-port structure. Another possible application is to adjust the LW frequency. This structure, which will be examined only with simulations in our study, is given in Figure 8. The aim here is to change the LW speed by applying a homogeneous tension to the IDT section of the LWR device using a DC voltage, thus shifting the center frequency of the LWR device to the right or left. It will be an important contribution that the LW filter, which has a very high-quality factor, can be adjusted even within 1-2% of the center frequency.

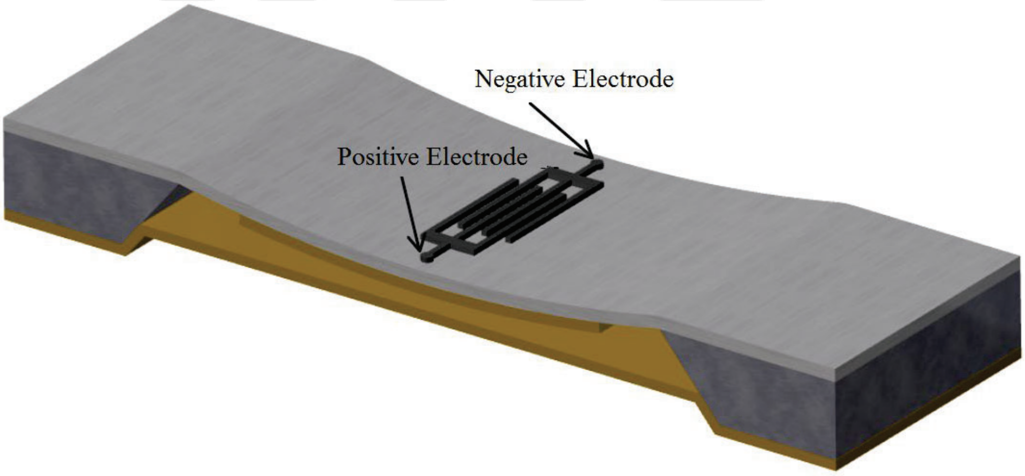

Figure 8: Schematic representation of Capacitive transducer (CT) structures placed between the IDT fingers.

In the thesis studies, LW was produced by using an AlN thin film layer on a silicon wafer. AlN also formed the membrane of CT structures (Figure 7). The electrodes of the CT structure are coated on AlN. The upper electrode is formed by coating on a silicon wafer. The frequency to be chosen within the thesis has been chosen to be high enough but low enough that we can easily see the phase delay and not complicate our fabrication and test work. In our preliminary simulation studies, the LW frequency was chosen as 100 MHz. A 55 MHz LW device was produced under laboratory conditions.

3.1.1. Mechanical analysis

The structure we propose in the thesis corresponds to a beam structure fixed from both sides under a mechanically distributed load (Figure 9) [75].

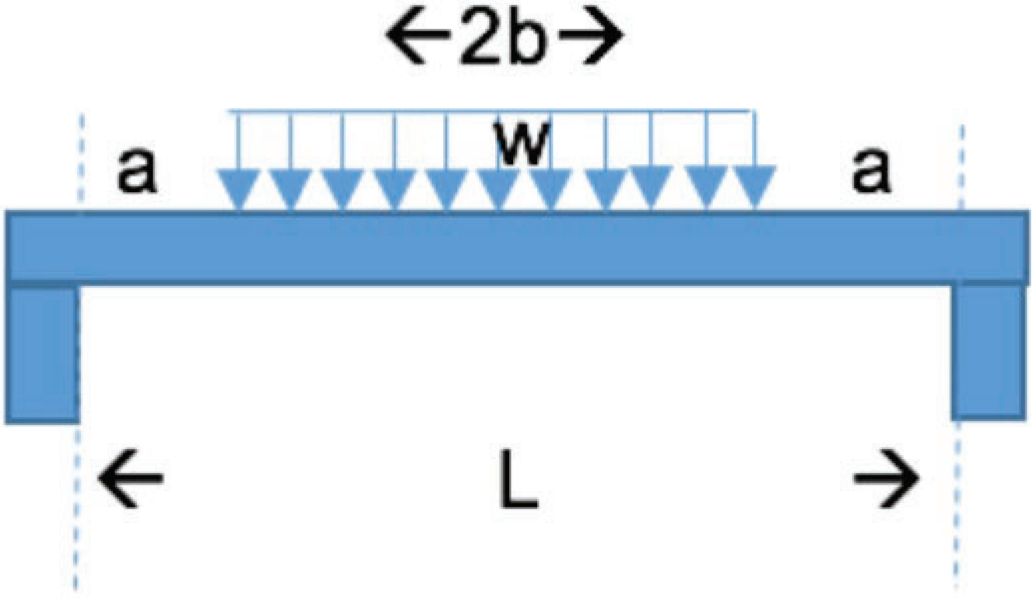

Figure 9: Mechanical equivalent of the proposed structure.

Here, since the beam structure is formed by hard material, AlN film, the maximum and minimum values of a slump are very close. The amount of precipitation (y_{max}) is given by (6).

$$y_{max} = \frac{w}{24.E.I}.\left[\frac{b.L}{4}.\left(12.b^2 - 4.L^2 - \frac{16.a.b^2}{L} - \frac{16.b^3}{L}\right) - b^4\right]; \ (\mathbf{6})$$

$$I = \frac{H.h^3}{12}; \ (\mathbf{7})$$

Here, '$2b$' is the upper electrode width, 'L' is the released film length, and 'w' is the distributed load (*Nt/m*). The distance between the IDT input port and the beam fixation point is given by 'a'. 'E' and 'I' represent the Youngs modulus and the moment of inertia, respectively, and the moment of inertia for the fixed-fixed beam is given by (7). Here, 'h' shows the beam height and 'H' its depth.

$$k = \frac{24.E.I}{b}.[\frac{b.L}{4}.\left(12.b^2 - 4.L^2 - \frac{16.a.b^2}{L} - \frac{16.b^3}{L}\right) - b^4]^{-1};\ \mathbf{(8)}$$

Based on this information, it is possible to obtain the spring constant of the system. Total force instead of distributed load: If $w = F.2b$ value is used, easily obtaining spring constant with Hook's Law ($F = k.y_{max}$) is possible (8).

By utilizing the obtained mechanical model, 3D simulation studies were got and the amount of collapse was compared and it was revealed how this affects the LW speed on the film.

3.1.2. Electrical analysis

Another issue that has been examined is to get the relationship between the electrical port and the amount of collapse. In this way, the limits of the DC voltage that will adjust the tension in the film will be got.

$$F = \frac{\varepsilon.2b.t.V^2}{2.g^2};\ \mathbf{(9)}$$

$$y = \frac{F}{k};\ \mathbf{(10)}$$

$$g = g_0 - y;\ \mathbf{(11)}$$

In this analysis, the safe DC voltage limit is also revealed. The electrostatic force (F) that will occur for a certain applied voltage value (V), how much collapse this force will cause in the system with known spring constant (y), and the distance (g) between the capacitive actuator plates because of this collapse are respectively (9), (10) and (11). Here, 'ε' shows the dielectric constant of the material between the lower and upper electrodes, 'g' the distance between the lower and upper electrodes, and 'g_0' the value of this distance at rest position (V=0) [76].

To calculate the net force in the system, the difference between the force exerted by the voltage source and the spring force must be taken:

$$F_{net} = k.(g_0 - g) - \frac{\mathcal{E}.2b.t.V^2}{2.g^2}; \ \mathbf{(12)}$$

As it is known, in this equation (12), while $\partial g > 0$, $\boldsymbol{\partial F_{net} > 0}$ ***should not be***, therefore it should be $\frac{\mathcal{E}.2b.t.V^2}{2.g^3} - k < 0$. When the maximum collapse amount is taken as $y = \frac{g_0}{3}$, *the maximum value of the voltage* (13) to be applied is:

$$V_{net} = (\frac{8.k.g^3}{27.\mathcal{E}.2b.t})^{\frac{1}{2}}; \ \mathbf{(13)}$$

The applied DC Voltage (V), the Force (F)/Distributed Load Value, the amount of collapse in the AlN film and the stress generated are determined by these calculations.

3.1.3. Lamb wave velocity with thin film precipitation

The collapse in the thin film influences the velocity by triggering several mechanisms. The most effective of these is that the change in the crystal structure after elongation reduces the electric field and the falling potential difference value negatively affects the wave velocity. The relationship between electric field and wave velocity is given by (14) [77, 78]. In this expression v_0 wave speed, f frequency, ε_p the dielectric coefficient of the piezoelectric material, m the admittance of the delay line and K^2 the electromechanical transfer coefficient.

$$v_0 = \frac{2.\pi^2.f^2.\varepsilon_p}{m.K^2}; \ \mathbf{(14)}$$

Apart from this, the change in the film density because of precipitation also influences the LW velocity. In addition, although it does not have a large effect, it affects the time it takes for the wave to reach the output port in the change in the delay's length line. Finally, the physical deformation on the IDT also affects the wave velocity [79].

The electrical and mechanical model of the studies we have done has been created with the theoretical analyzes we have shown in the previous sections. The relationship between the LW rate and the amount of thin-film precipitation was investigated. The parameters on which the velocity change depends are listed as the electric field decrease because of the change in the crystal structure after elongation, the change in the film density because of precipitation, and the change in the delay's length line. The effect of the change in crystal structure after elongation has been shown previously (14). In our studies, the effect of density change was also revealed. As it is known, the volume of the objects that extend under pressure while remaining in the elastic area varies. The object will increase in size along the axis it extends, but there will be a length change proportional to the amount of extension in other axes. As it is known, the length change in other axes can be calculated with the Poisson Ratio, which is an object-specific constant. Poisson's Ratio:

When $\upsilon > 0.5$, the elongation decreases the volume of the object; When $\upsilon < 0.5$, the volume increases with extension. In ceramic materials, it is usually around $\upsilon \sim 0.24$, and the density decreases with elongation in these materials. Since the density of the object is given by the expression $\rho = \frac{M}{V}$, while the mass (M) is constant, the density will decrease when the volume (V) increases.

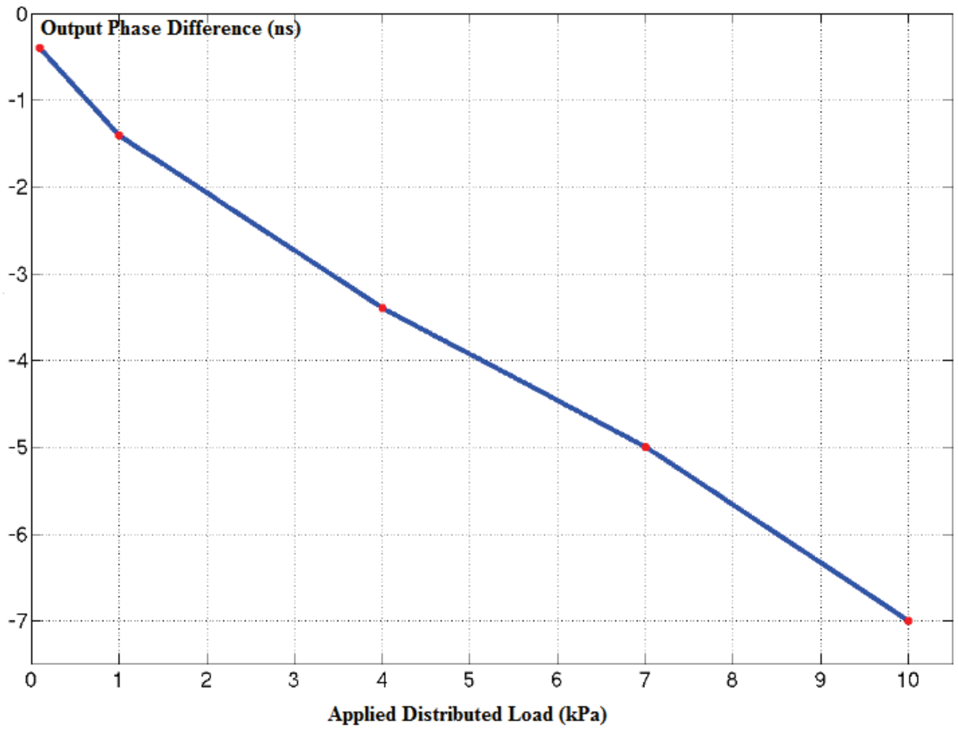

Figure 10: The relationship between the distributed load applied to the film and the amount of LW delay.

As can be seen in the expression given by density change (5), LW will change its speed. In this relationship, it can be seen that decreasing the density will increase the speed, and this result is compatible with the distributed load-output phase difference relationship we obtained previously and given in Figure 10.

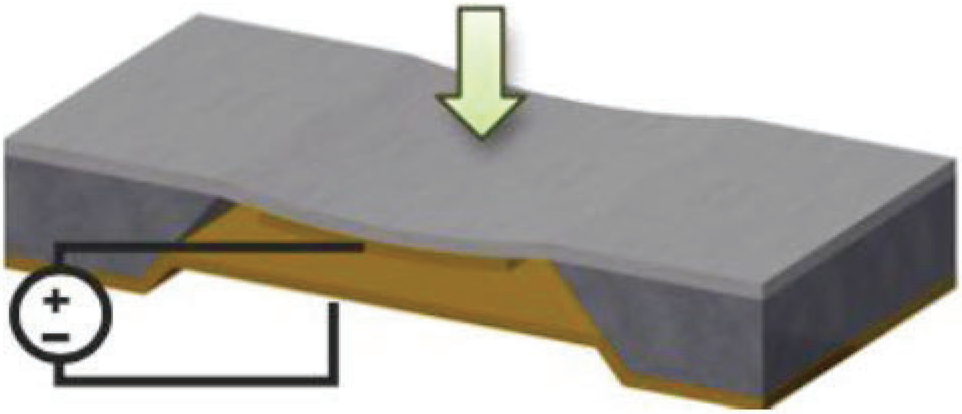

Figure 11: Illustration showing thin film and distributed load.

The effect of the amount of elongation formed in the film on the volume and density by pulling the thin-film down (Figure 11) was investigated, the variation of the wave velocity was calculated and the extent to which it fits the results given in Figure 10 was examined.

When stress is applied in one dimension; The amount of elongation ($\varepsilon_{x,\,y,\,z}$) is given by the applied stress (pressure=σ)/modulus of elasticity (E). At the end of this process, other dimensions also change and other dimensions change by $-V.(\frac{\sigma}{E})$. In the most general case, if we assume that all three dimensions are under stress, we get the set of equations given by (15).

$$\varepsilon_x = \frac{\sigma_x}{E} - V\frac{\sigma_y}{E} - V\frac{\sigma_z}{E}$$

$$\varepsilon_y = -V\frac{\sigma_x}{E} + \frac{\sigma_y}{E} - V\frac{\sigma_z}{E}$$

$$\varepsilon_z = -V\frac{\sigma_x}{E} - V\frac{\sigma_y}{E} + \frac{\sigma_z}{E}$$

$$\mathbf{(15)}$$

If a unit volume cube is considered, the volume after extensions will be obtained as $(1+\varepsilon_x)(1+\varepsilon_y)(1+\varepsilon_z)$. When the operation is performed, assuming that only one-dimensional shrinkage is applied, the new volume will be calculated as $V = (1 + \varepsilon_x + \varepsilon_y + \varepsilon_z)$ and the volume change will be $\Delta V = v - 1$. If the expression (15) is substituted in the equation giving the volume change, $\Delta V = (\frac{\sigma_x}{\mathrm{E}})(1 - 2V)$ is calculated. Since we initially assumed a unit volume, for any initial volume (V_0) it will be as given by expression (16).

$$\frac{\Delta v}{v_0} = e = (\frac{\sigma_x}{\mathrm{E}})(1 - 2v);\ \mathbf{(16)}$$

If the initial density is given as $\rho_0 = \frac{\mathrm{M}}{V_0}$, then the density (17) can be given as:

$$\rho = \frac{\mathrm{M}}{V} = \frac{\mathrm{M}}{V_0 - \Delta V};\ \mathbf{(17)}$$

In this case, the density after the new spelling is:

$$\rho = \rho_0(\frac{1}{1 - \mathrm{e}});\ \mathbf{(18)}$$

LW velocities can be easily calculated for two different stress values by substituting the ρ and ρ_0 density values in the expression (5). For the material we use here (AlN film), the film thickness is d=500 nm, λ=9.8 µm, E=340 Gpa, ν =0.24 and stress values are taken as $\sigma_{x_0} = 1000\ Pa$ and $\sigma_{x_1} = 4000\ Pa$, respectively ρ and ρ_0 calculated.

The velocity values obtained after the calculation were calculated as:

$$306.68777409030617415827976578206.\pi\ \frac{\mathrm{m}}{\mathrm{s}},$$

$$306.68777338672833759741313 98581.\pi\ \frac{\mathrm{m}}{\mathrm{s}},$$

respectively. If the times to traverse the 492.5 µm delay line used when obtaining the results given in Figure 10 are calculated, it can be calculated as:

5.044982267331531211596029606 8806 µs,

5.0449822789053140326132051995955 µs, respectively. The difference is 115.74 ps.

The calculation reveals that the effect of density change on speed is negligibly small. Therefore, only the effect of the change in the crystal structure will be considered while creating the model.

3.2. Design Fabrication And Validation Of A Lamb Wave Device

In this section, first, the new LW device structure will be explained, and the studies carried out to reveal and test this structure will be presented. Afterward, the pre-simulation studies that test the accuracy of the concept and the simulation results got will be presented and the simulation studies carried out within the project will be mentioned. Finally, studies on the tests of filter structures that have emerged by using the obtained structure will be explained.

Generation of LW waves is classically achieved by growing IDT structures on thin film. This process was carried out on a silicon wafer in order to allow microelectronic circuit integration. In order to produce lamb waves, the thin film coated on silicon must be piezoelectric. There are also methods in the literature that use CMUT structures and do not require piezoelectric properties [97]. The electromechanical transfer coefficient, which is an important parameter in terms of LW production, is higher in structures using CMUT than in thin-film coated structures. Although the electromechanical transfer coefficient got with CMUT structures gives better results, in theory, thin-film coated plates give better results in practice because of fabrication problems.

LW fabrication on a wafer is accomplished using IDT structures, such as the SAW fabrication process. IDT is a structure that has three ports, 2 acoustic and 1 electrical, and generates acoustic waves propagating in two directions (Figure 4). This structure is formed by the production of two comb-shaped electrodes nested inside each other. IDT structures can be used alone in LW/SAW devices, or they can be used as LW send-receive pairs by placing them together (2-port SAW devices). Between the mutually placed IDT transmit/receive pair there is a delay line that will phase the input signal, a two-port SAW device that we have fabricated before can be seen in Figure 12 [80].

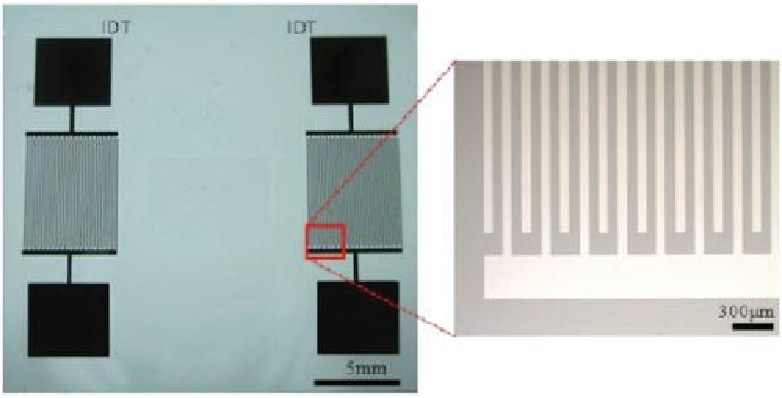

Figure 12: A two-port SAW device built on a piezoelectric wafer (ST-Quartz) for a biosensor application. The transmission and reception IDT pair and the delay line between them are seen [80].

The studies to be carried out within the scope of the thesis can be evaluated under 1. Design and simulation studies, 2. Fabrication and characterization studies. 3. Testing and validation studies. The literature related to the studies conducted within the scope of the thesis is discussed below.

3.2.1. Design and simulation studies

The design of LW devices requires the selection and change of many parameters such as film thickness, electrode sizes, shapes and placements, film and wafer material, operating frequency, and wave propagation modes [64], [65], [81]. Therefore, the design process requires a lot of repeated fabrication. Also, analysis of the complex electromechanical interactions during LW production is required in many applications. Because of these needs, many modeling and analysis studies have been carried out in the literature for IDT structures used by both LW and SAW devices as electrodes.

3.2.1.1. Developing a finite element analysis model for design, performing analysis through simulation

While the use of IDT and LW models is a good starting point for design, the various approximations and assumptions used during Acoustic ⇔ Electrical conversions affect the accuracy of the calculations. Apart from this, it is necessary to use a more effective method to better understand the acoustic interaction on the film layer. Finite Element

Analysis (FEA) provides a more comprehensive analysis opportunity, as it uses a differential equation solution-based method. The characteristics got by solving the differential equation are independent of the LW device structure and are calculated according to the properties of the material used. Within this project, simulation software (COMSOL) from Finite Element Modeling (FEM) software was used to analyze both electrical and acoustic interactions. This software is a widely used tool for finite element modeling FEM, but it has some limitations previously reported:

a. In FEM software it is impossible to define a non-reflective right and left boundary to be used for piezoelectric analysis. This problem prevents the definition of an infinite length plate [82]. This problem, which occurs when the waves reflected from the plate boundaries are not desired to affect the simulation results, can be solved by defining silicon fields with high damping coefficients in the desired boundary regions [83], [84].

b. The higher the precision, the higher the account complexity. This problem has been reported not only in COMSOL but also in other FEM software [85]. The major problem here is that while the distance between IDT fingers is in the order of 400-600 nm [86]-[89], the length of IDT fingers can go up to 0.5-5 mm in some applications [86], [87], [89] and therefore the entire region must be sampled in nanometre scale. Since the reduction of IDT finger lengths will cause the diffraction effect to be seen in the near field, this parameter should be chosen large enough [90], [91]. To reduce the effect of this problem, the simulation is reduced to 2 dimensional [92]. Solutions for making it have been suggested.

c. Metal properties of IDT fingers are not considered. The effect of metal fingers can be roughly divided into 3 groups: Electrical Charging, Mechanical Charging, and Energy Storage [93], [94]. In most analyzes, only mechanical loading and energy storage effects are considered. In addition, in our study, the COMSOL software was used to model the capacitive transducers structures used in the proposed structure. Similar FEM studies in the literature have been conducted to determine the design parameters of capacitive micro-machined ultrasonic transducer (CMUT) [81], [95]-[100]. Since a capacitive transducer with a structure similar to CMUT structures was used in our study, similar approaches could be used in COMSOL simulation studies (The main difference of the CT structure we used from the CMUT structure was that it did not require vacuum).

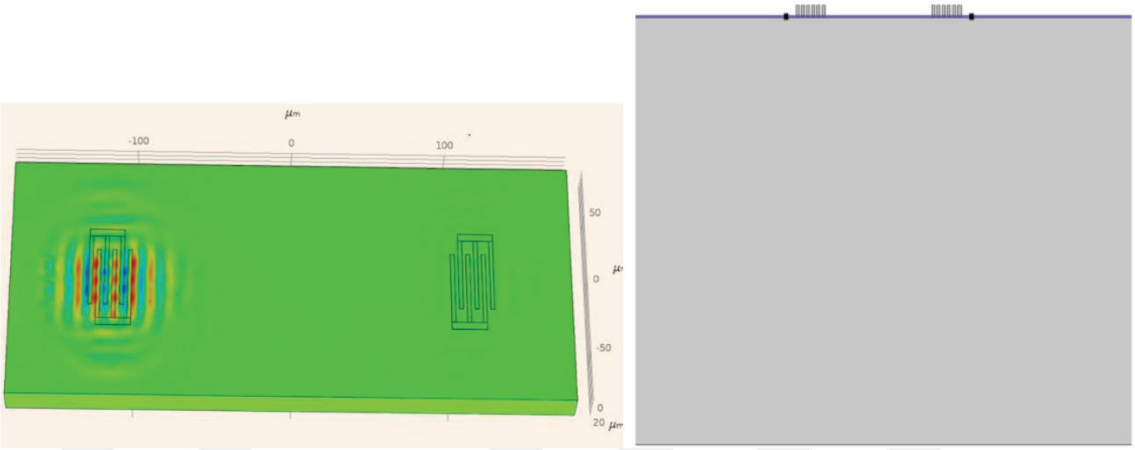

Figure 13: Demonstration of the installed COMSOL model. The drawing on the right is side view: Here, Si (500 µm), AlN (200-500 nm) and Cr electrode layers are shown, respectively.

In this context, in the simulation studies, a model with AlN coated on silicon and Cr transceiver IDT electrodes was established (Figure 13). Models containing various values of AlN between 200 and 500 nm on 500 µm silicon were used and the film characteristics were extracted. COMSOL model parameters are given in Table-1.

Table 1: Simulation parameters of the model established for the simulation studies.

The Number of CFL	0.2
Mechanical loss factor	0.001
Center Frequency	530 MHz
Horizontal spacing between ports	10.25*λ
IDT Finger-to-Finger Distance (Pitch)	9.85 µm
Number of IDT Fingers	3
Delay Line Distance	492.5 µm
Piezoelectric Film Length	1324.8 µm

Si thickness	500 µm
Simulation Time	375 ns
Simulation Time Step	0.2 ns
Maximum Network Element Size	λ/5
Stiffness Damping Coefficient	1.5915 ps
Distributed Load Trials	0 kPa, 0.1 kPa, 1 kPa, 4 kPa, 7 kPa, 10 kPa

(Continue)

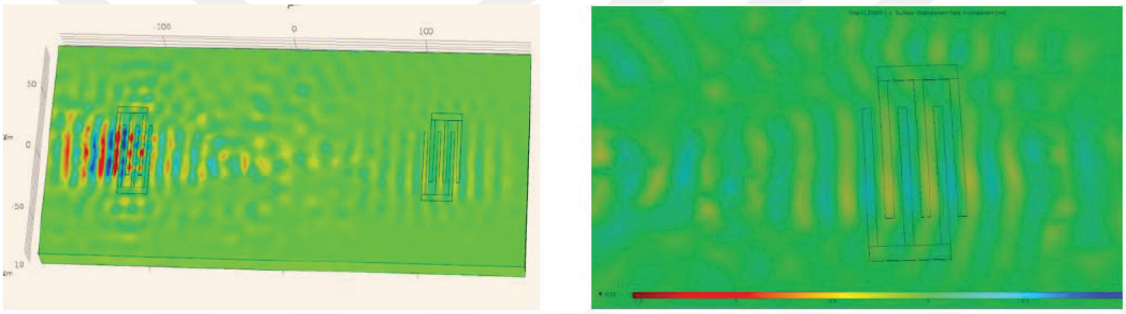

Figure 14: (Left) Displacement images got by 3D simulation, (Right) LW reaching receiver IDT.

3D simulation images made using this model are given in Figure 11. Here, the system was driven by a 530 MHz continuous wave and the propagation of the wave was investigated. In the following studies, the same model, different AlN thin film values were used and impulse responses, frequency characteristics and thin film characteristics were examined. Here, a 10 V unipolar square pulse between -1e-12 and 1e-12 sec is used as impulse function. Output port responses are given in Figure 15-17.

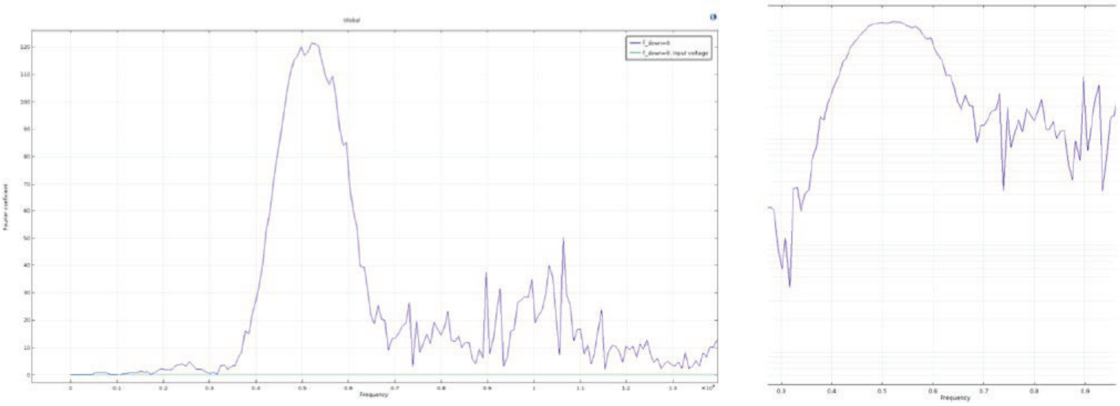

Figure 15: Frequency response plots for 500 nm film thickness: (Left) linear scale, (Right) logarithmic scale.

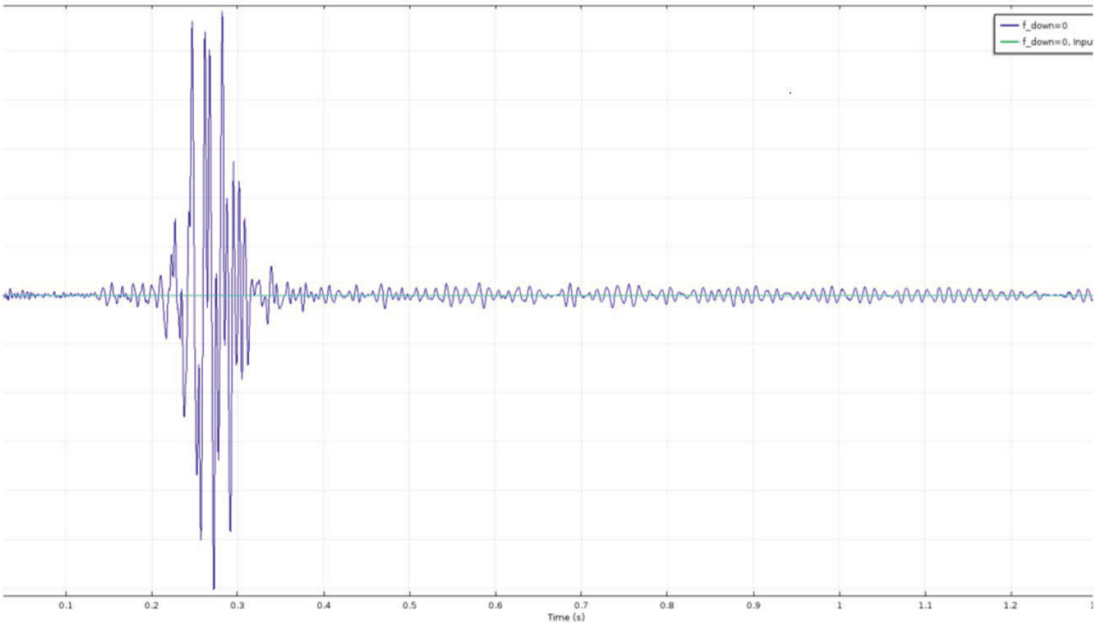

Continue

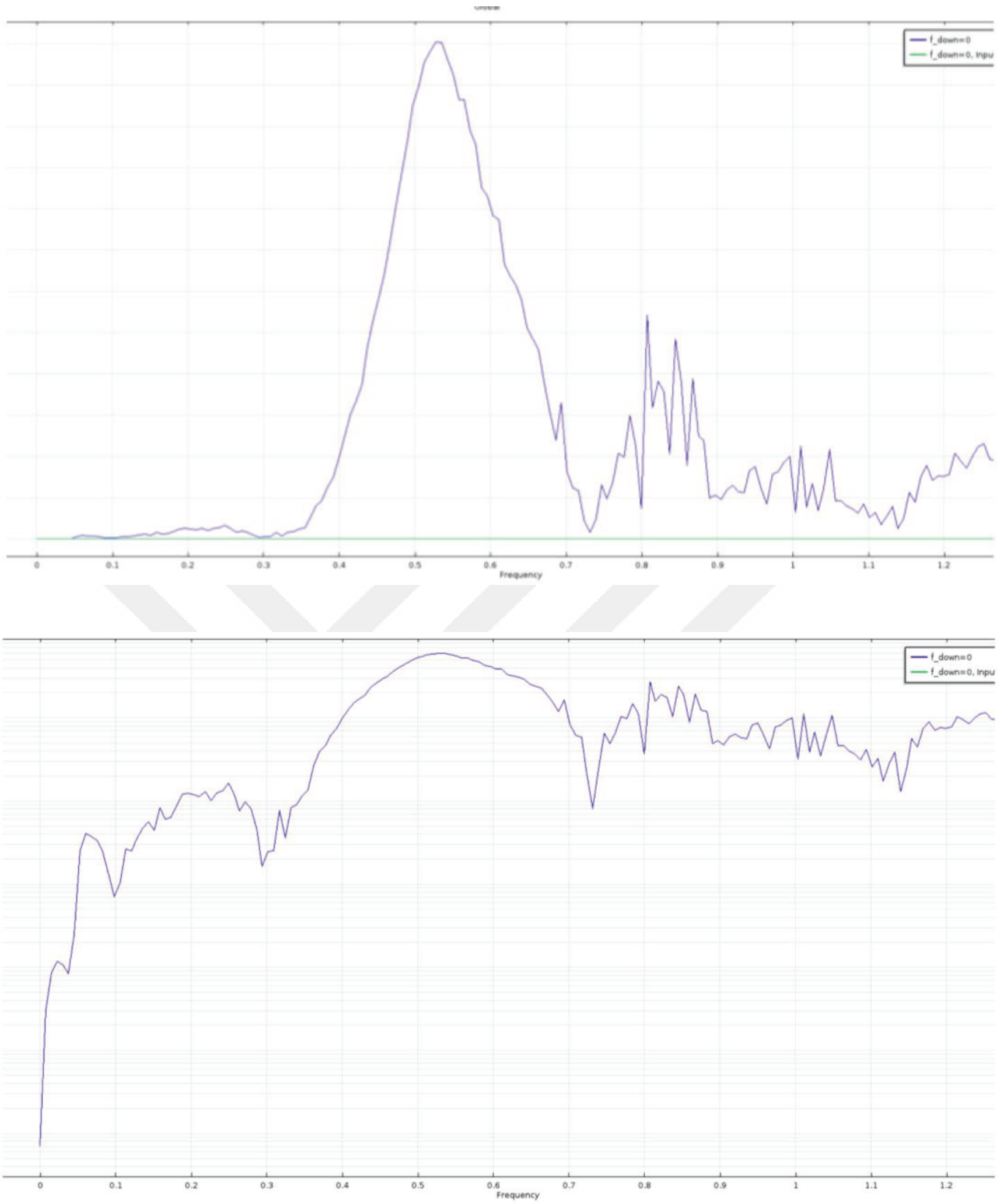

Figure 16: Impulse and frequency response plots for 400 nm film thickness, impulse response at the top, frequency linear scale in the middle, frequency logarithmic scale at the bottom.

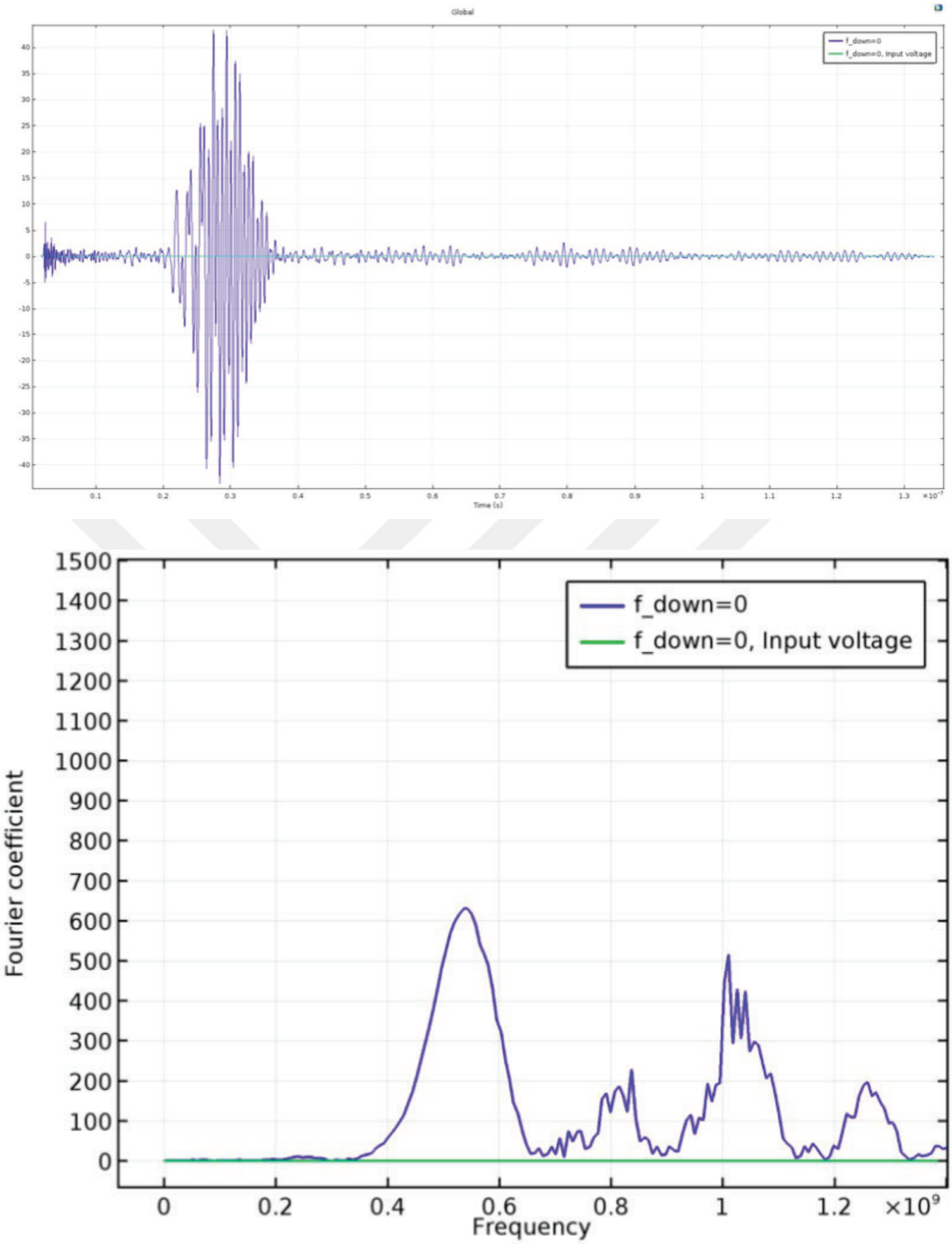

Figure 17: Impulse (top) and frequency response (bottom) plots for 200 nm film thickness.

Impulse responses and linear and dB scale frequency responses (magnitude) of structures with film thicknesses of 500, 400, and 200 nm, respectively, are given. First of all, it is seen that the impulse response is received at the design frequency. In the measurements made, designs with a film thickness of 200-500 nm show response frequencies of 530, 525, and 515 MHz, respectively. It is expected that with the increase of film thickness, a decrease in speed and a slight decrease in operating frequency.

In addition, the negative effect of the decrease in the film thickness on the frequency response is striking. As the thickness decreases, the peak value of the response at the design frequency approaches the noise level of the signal. This phenomenon can be seen more clearly in the logarithmic scale figures in Figures 15-16.

In addition, it is noteworthy that the impulse response moves away from the zero points as the thickness increases. Therefore, as the thickness increases, the speed decreases, and the same effect is seen in the frequency response. Although the velocity change because of thickness is not important for our project, the relation between thickness and velocity has been got by simulation. That the thinner film absorbs the surface wave more quickly indicates that increasing the coating thickness will increase the signal level.

3.2.1.2. The Designs of the fabricated LW device

First, it is planned to produce LW devices at two different frequencies (100 MHz and 55 MHz). In order to determine the wavelength, it should be known which wave mode to use and what the velocity is. Frequently used wave modes are known as zero-order Asymmetric (A_0) and Symmetric (S_0). In our study, A_0 wave mode is used and the LW speed can be calculated approximately using the formula given by (5).

In addition, using the formula given by (3), which gives the LW velocity values, velocity calculations were made through iteration. Here, frequency (f), film thickness (d), angular frequency (ω), Shear Wave Velocity (C_T), wavenumber (k), Longitudinal Wave velocity (C_L), and C_P are used for Phase Velocity.

An initial frequency is selected and a solution is provided by iteration. In the study carried out by preparing a MATLAB code, the antisymmetric mode lamb wave calculations we made using the values f=100 MHz, ρ=3300 kg/m^2, E=270 Gpa, ν =0.24 and the velocity values we found with iteration and approximate formula (5), respectively, are 985 and 991 m/s.

Among these velocity values, 985 m/s was used, and λ=9.85 µm for f=100 MHz with the relation c= λ.f. Thin-film coated silicon will be used since the simulation studies to be carried out at the beginning will only be for film characterization. Therefore, the wave will travel not only on the film but also on the silicon + film layer. In other words, one of the SAW modes will be driven, not LW. The speed value of SAW modes traveling on AlN film is given as approximately 5100-5200 m/s in the literature. Experimental verification of this velocity value was done in film characterization studies. Although the value in the literature is used, for now, the simulations will be repeated with the experimentally obtained velocity value. Since the wavelength is determined by the distance between the fingers and is chosen as 9.8 µm above, the operating frequency should be around f=532 MHz in SAW mode with c= λ.f relationship.

3.2.2. Fabrication and characterization studies

The step that follows the design and simulation processes are fabrication and characterization studies. The IDT structure is usually produced on a piezoelectric wafer, and the IDT form is formed on a sheet of metal coated on the plate [6]. Although this production process, which has been used in the production of IDT for a long time, is simple and stable, new fabrication methods have been proposed in recent years because of the need for monolithic-IC in filter and sensor applications (thin-film SAW filters) [101]. The most important advantage of LW structures when compared to conventional SAW structures is that they allow microelectronic integration with high Q factor and adjustable wave velocity. In our proposed structure, the thin-film piezoelectric coating is used, so that the delay line is formed from a continuous and single medium (in the coated piezoelectric film). The piezoelectric thin film also formed the membrane of the CT structure placed above the delay line. In the literature, LW devices are designed using various thin film coatings, such as ZnO, LiNbO3, PZT, and AlN.

Since it shows the best compatibility with the silicon crystal structure in our study, AlN film, which is more preferred in recent studies, was used [102]-[105]. The structure got by piezoelectric thin film coating of the CMUT structures we propose is like the

Piezoelectric Micromachined Ultrasonic Transducers (PMUT) structure. Coating the membrane parts of capacitive structures with piezoelectric material is a previously applied and defined process [100], [106]-[111]. The sputtering process is used for the coating process, and the most important problem reported in the studies is that the material properties change after the sputtering process. Especially the sequence distribution should be examined by optical methods after the process. Apart from that, the surface structure and roughness should also be checked [112]. A study was conducted by Clement to model SAW characteristics after sputtering Aluminum Nitride (AlN) on the silicon wafer was coated, and the AlN film sputtered on various silicon plates was compared in terms of its electromechanical properties. In the study, it was concluded that low resistance conductive silicon wafers showed poor performance [113]. In a recent study, it was reported that coating the piezoelectric film layer on IDT electrodes increases the electromechanical transfer capacity. In this study, ZnO a piezoelectric film, and all steps from design to fabrication were explained [114], [115].

In our study, aluminum nitride (AlN) was used as a piezoelectric thin film due to its stronger electromechanical transfer potential. Although its coupling coefficient is not as high as that of ZnO and $LiNbO_3$ that are also widely used in piezoelectric MEMS devices, it has high acoustic velocity, high thermal conductivity, low acoustic loss, chemical stability and relatively low *TCF* (Temperature Coefficient of Frequency) [36]. Piezoelectric AlN film structure was examined in the study by Freidel et al. For a 2 GHz resonator designed using 1.1 µm AlN layer coated on a 32 µm molybdenum layer, the quality factor was 1000 and the electromechanical transfer constant was measured as 6.5%. When aluminum electrodes were used instead of molybdenum electrodes, it was observed that the quality factor decreased 3 times because of high acoustic propagation losses on aluminum [116].

3.2.2.1. Coating and fabrication of a thin-film

Within the scope of the studies described in this section, the steps for metal electrode coating, etching, membrane release and optimization are mentioned. Within the scope of these studies, the electrode was enlarged on the SOI wafer covered with AlN film and the lower part of these electrodes was etched. The applied coating and etching processes are given in Figure 18. In addition, since the AlN film coating process was carried out in another laboratory in the studies carried out in this section, this fabrication process was also optimized again and the film structure was examined.

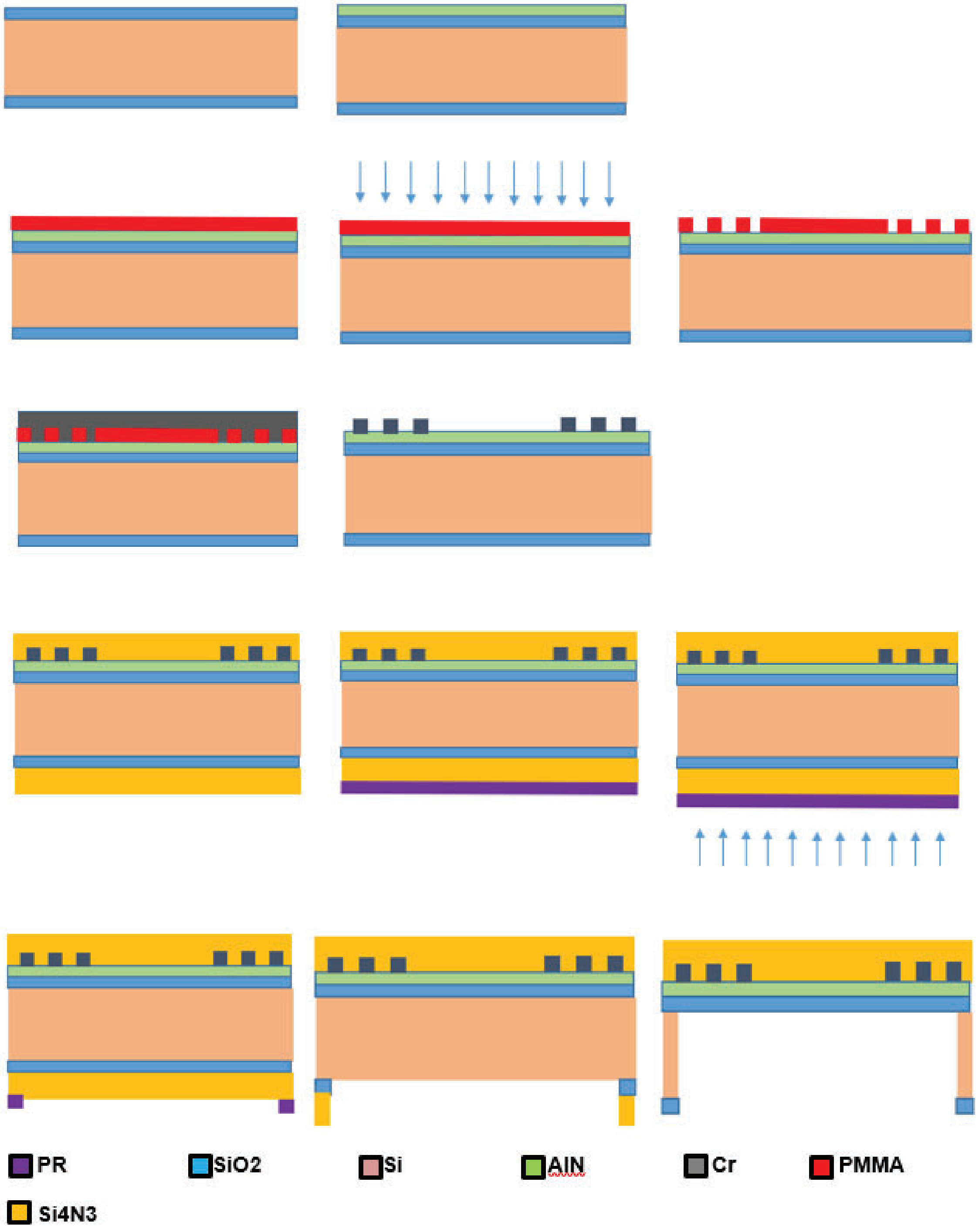

Figure 18: Fabrication processes for electrode growth and thin film release.

The processes for forming IDT electrodes are explained in this section. SOI wafer was used during the preliminary studies. The SiO_2 (300 nm) layer will be useful both for insulating and as an etch-stop layer when releasing the thin film. The first three lines of Figure 18 show the steps of forming IDT electrodes on AlN film. Here, in the first step, the SOI wafer was coated with AlN (100-200 nm) with a sputter device. Then, the top of the AlN layer was coated with PMMA with a spin coater, and IDT electrode was patterned by EBL. Afterwards, Cr (100 nm) coating was done with metal evaporator and lift off process was applied using acetone bath. At the end, Cr IDT electrodes on AlN were successfully grown (Figure 19).

Figure 19: Electrode enlarged AlN coated SOI wafer.

After this step, the work on the discharge of the part corresponding to the back side of the IDT electrodes and the release of the thin film was started. In this context, the anisotropic wet etching technique was chosen as a suitable technique since the silicone would have to be bulk etch. For this purpose, KOH was chosen as a chemical that erodes Si rapidly but slowly erodes SiO_2. In KOH, SiO_2 etches about 1000 times slower than Si. In addition, Si_3N_4 is planned to open a suitable window. The Si_3N_4 layer is hardly etched by KOH.

The last two lines in Figure 18 describe the work done to release the thin film. For this purpose, firstly, Si_3N_4 was coated on both sides of the sample with Plasma-Enhanced Chemical Vapor Deposition (PECVD) (Figure 20). The sample was first cleaned in acetone and isopropyl alcohol and in an ultrasonic (US) bath. Afterwards, 50 nm Si_3N_4 was coated with PECVD method at 300 C temperature, 400 nm/h coating speed, 8 minutes, using Oxford Plasmalab System 100 PECVD system, which is suitable for coating SiO_2 and SiN_x films. This step both protects the electrode side and prepares the back surface for wet etching. Processing time takes 14 minutes, including preheating and vacuuming.

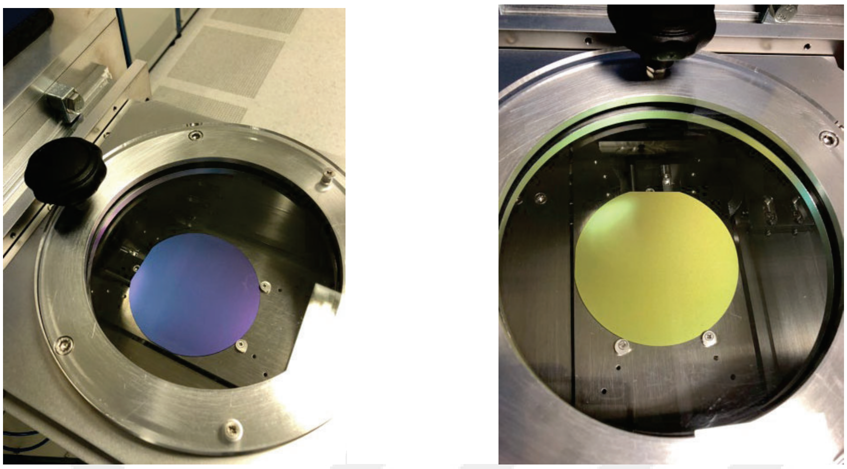

Figure 20: (Left) View before and after (Right) Si_3N_4 coating with PECVD.

After the backside of the particleboard was coated with Si_3N_4, this section was prepared for wet etching to release the film. For this purpose, the rear section is covered with PR. The areas to be etched were opened by photolithography. For the photolithography process, the mask is designed and aligned to open the bottom of the mask (IDT-delay line-IDT) sections in the lithography step. The mask to be used in the Bulk-Etch process can be seen in Figure 21.

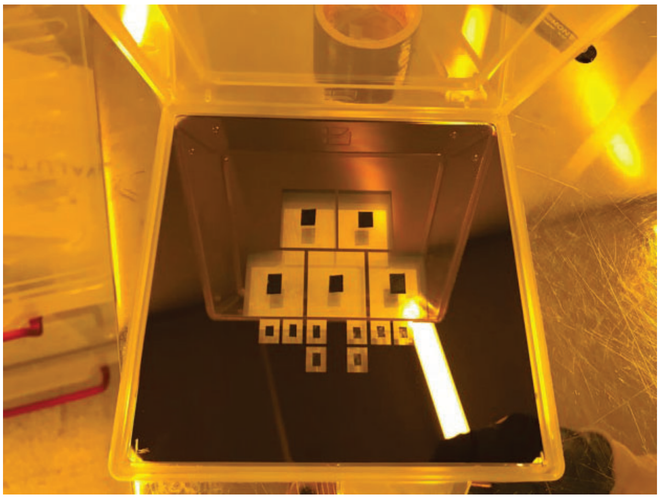

Figure 21: Mask to be used to open Bulk-Etch areas.

After performing this step, which can be seen in the third row of Figure 18, the back side of the wafer is seen as given in Figure 22.

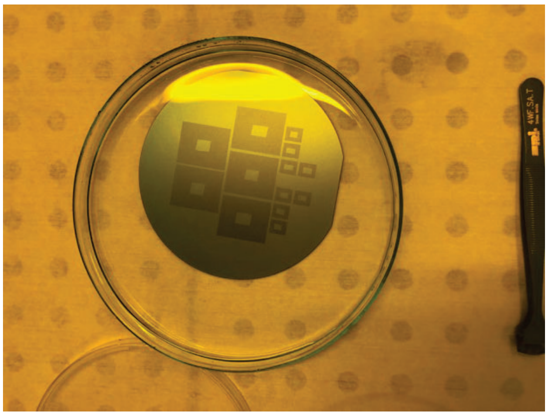

Figure 22: Surface shaped by PR after photolithography.

After the photolithography process, the Si_3N_4 and SiO_2 layers must be etched. This step is shown in Figure 18, the first figure in the last row. Inductively Coupled Plasma – Reactive Ion Etching (ICP-RIE) technique was used for etching. With the Oxford PlasmaLab System 100 DRIE, which is optimized for Si, SiO_2, and SiNx thin films, SiN_x surface was treated with ICP-RIE for 5 seconds at a speed of 400 nm/min. Then, the surface was etched and SiO_2 windows were opened (Figure 23).

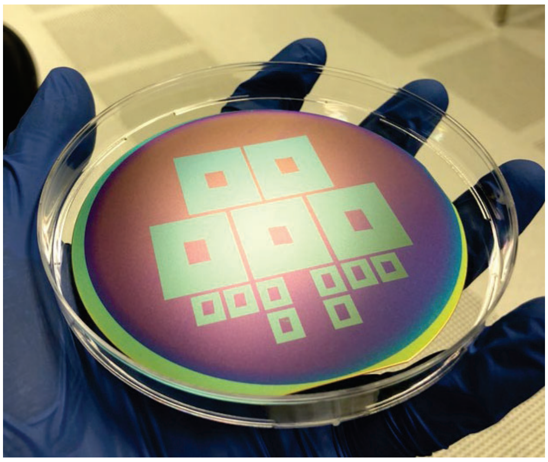

Figure 23: Structure with Si_3N_4 and SiO_2 obtained as a result of the first ICP-RIE.

In the samples we obtained, 300 nm of SiO_2 remaining on the surface of the windows must be etched in order to make Si suitable for etching tests with KOH. The recipe with an etching speed of 250 nm/min was applied for 1 minute and 15 seconds, and at the end of the process, windows with SiN_x around and Si inside were got (Figure 24).

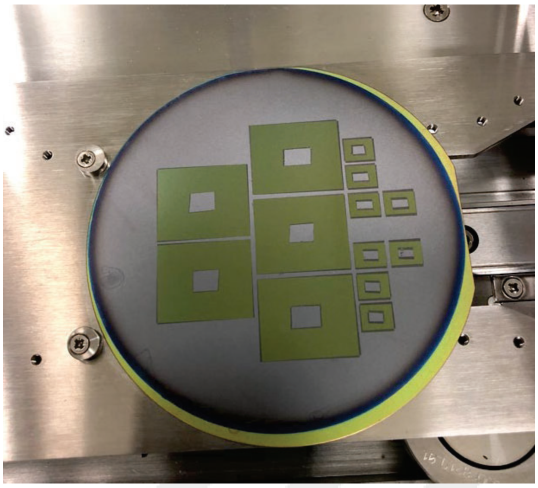

Figure 24: Structure with Si_3N_4 and Si obtained as a result of the second ICP-RIE.

The sample is then ready to be diced and subjected to the wet etching process. The final state of the Sample is as seen in the middle illustration in the last row of Figure 18. The next thing to do is to optimize the wet etching process by making more trials. Subsequent processes were carried out in the laboratories of Marmara University, Faculty of Science and Letters, Department of Chemistry. First, the wafer (sample) was cut into pieces using a pen scriber (Figure 25). Then, KOH solutions were prepared at 20-30% concentrations. For the abrasive with a concentration of 20% KOH solution, 40 g of solid KOH and 210 ml of DI-Water were used. It is also possible to add isopropyl alcohol to the solution in order for the KOH to achieve a smoother etching surface. However, since alcohol boils at 80 degrees, it was thought that corrosion problems might be encountered at high temperatures, and both alcoholic and non-alcoholic solutions were tested. When alcohol is used, 190 ml of DI-Water and 40 ml of IPA are used instead of 210 ml of DI-Water (Alcohol weighs half as much as water by volume). Therefore, the prepared solutions are:

- **a.** 20% KOH, no IPA => 40 g KOH tablets + 210 ml DI water
- **b.** There is 20% KOH, IPA => 40 g KOH tablets + 190 ml DI water + 40 ml IPA
- **c.** There is 30% KOH, IPA => 70 g KOH tablets + 190 ml DI water + 40 ml IPA

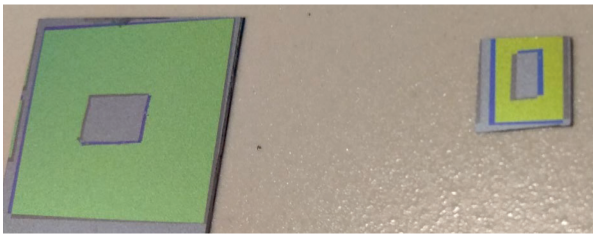

Figure 25: Bottom views of fragmented 33 MHz (Left) and 100 MHz (Right) LW devices, before bulk-etching. The outer frame is Si3N4, the middle section is Si.

The chemical wet etching process was carried out at a high temperature in order to be faster. The hottest point without boiling was chosen as 90°C. There is information in the literature that at this temperature, approximately 175 µm of etching per hour will occur. For this purpose, the apparatus given in Figure 26 was prepared and the temperature of the 20% KOH solution, which does not contain IPA, was increased up to 90 degrees and fixed by controlling it with a thermometer. Afterward, the sample to be etched was placed in the liquid. Figure 26 shows an example of both the setup and the etching process. For example, it can be clearly observed that bubbles emerge from only the middle region and only this region is etched (Figure 26). If there is etching in unwanted areas, the bubbles easily show this. An image of a commonly worn example is shared in Figure 27.

Figure 26: High temperature etching setup: at 90°C, 20% KOH and no IPA.

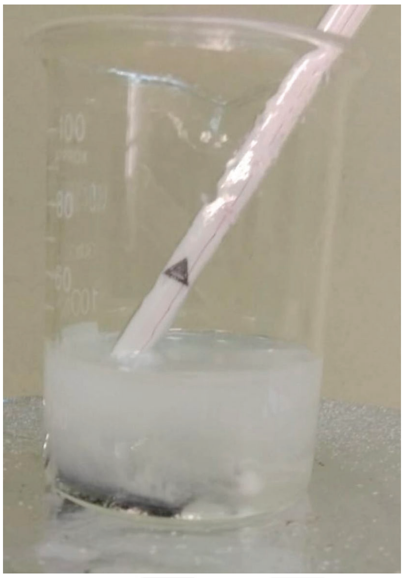

Figure 27: Etching of unwanted areas.

In addition, long-term abrasion tests were carried out at room temperature. Solutions used in this process: a) There is 20% KOH, IPA => 40 g KOH tablets + 190 ml DI water + 40 ml IPA. b)There is 30% KOH, IPA => 70 g KOH tablets + 190 ml DI water + 40 ml IPA.

The samples were kept in these solutions for 19 hours and 20 minutes. Etched samples were examined using a Profilometer and the etching process was optimized.

Various experiments were carried out using the high-temperature etching apparatus. E.g; The Profilometer result of the sample left for 1 hour and 45 minutes at 90 °C, 20% KOH, IPA-free solution is given in Figure 28. Because of these tests, it was found that the sample was etched by 200 μm under these conditions. Therefore, it takes 4.3 hours to etch the 500 μm-thick SOI wafer.

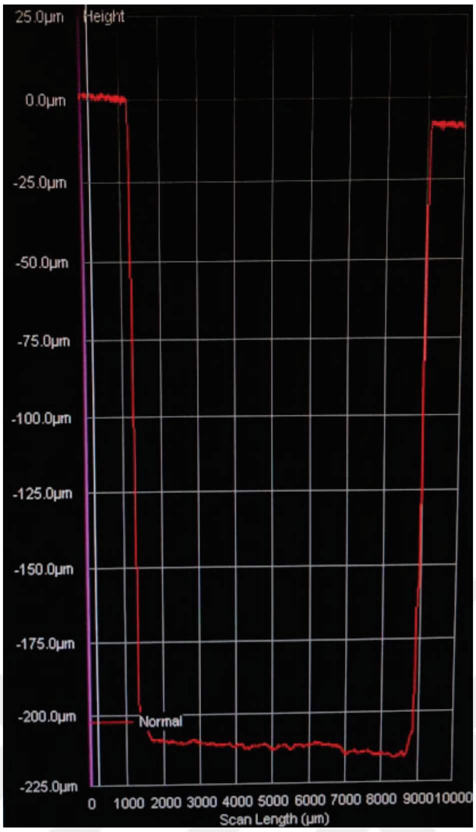

Figure 28: Profilometer result of sample left for 1 hour 45 minutes at 90°C, 20% KOH, non-IPA solution.

The profilometer results of the samples, which were kept at room temperature for 19 hours and 20 minutes, are given in figure 29. Here, solutions containing 20% KOH and 30% KOH provided approximately 17 µm and 20 µm wear, respectively. Although these values are quite low, the profilometer results show that the wear is of very poor quality. The roughness of worn surfaces is quite high.

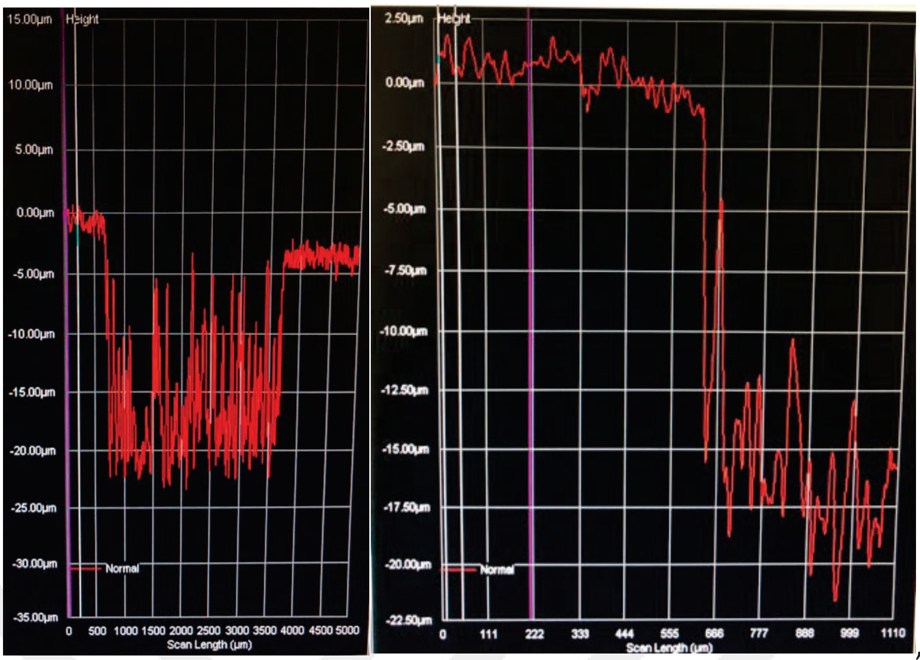

,

Figure 29: Profilometer results for samples etched for 19 hours 20 min at room temperature: 30% KOH (Left), 20% KOH (Right).

Because of the etching tests, it has been understood that wet etching at high temperatures provides optimum results in terms of both quality and speed. The required etching time has been determined. Since the SiO_2 layer just below the thin film will act as an etch-stop, a slight overshoot of the etching will not cause a problem. The top and bottom views of the structure after the optimized etching process are given in Figure 30.

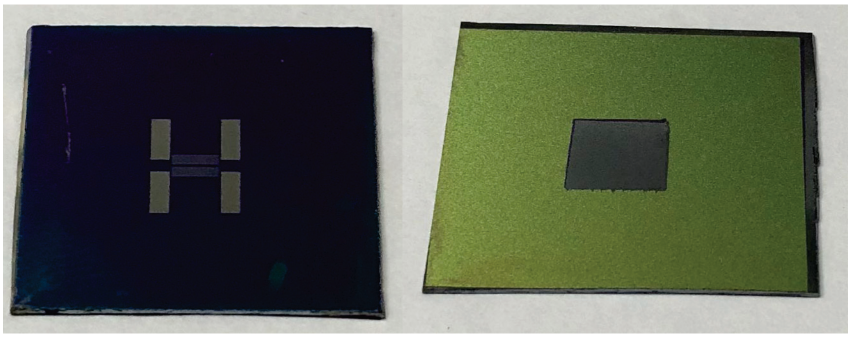

Figure 30: Top and bottom view of the resulting LW device.

3.2.2.1.1. Thin-Film characterization

Our aim with this work package is to show the purposeful effectiveness of the AlN film, which we will use as the piezoelectric layer. First, various thicknesses of the coating are applied to a silicon wafer. For coatings, it is primarily important that they be uniform, continuous, and have a crystal orientation to produce LW. According to the test results, the coating process has been optimized. The measurement of the LW velocity on the pavement was also made. Film coatings of approximately 50 nm, 100 nm, and 200 nm were made on 100-Si wafers and the results were examined by Electron microscope (SEM). DC sputter device was used for the coating process, and AlN was formed with reactive nitrogen gas in pure-Al-target and Ar plasma. Initially, the Ar/N ratio was selected as 7/3, the pressure was 7.5 mtorr and the temperature was set to 300 °C. It was observed that the plasma was extinguished after 1 hour when DC 200W was used. When looking at the sample, it was seen that 43 nm coating was achieved, but it was noticed that the coating was not uniform enough in SEM images. However, no cracking was observed along the pavement surface because of internal stress (Figure 31).

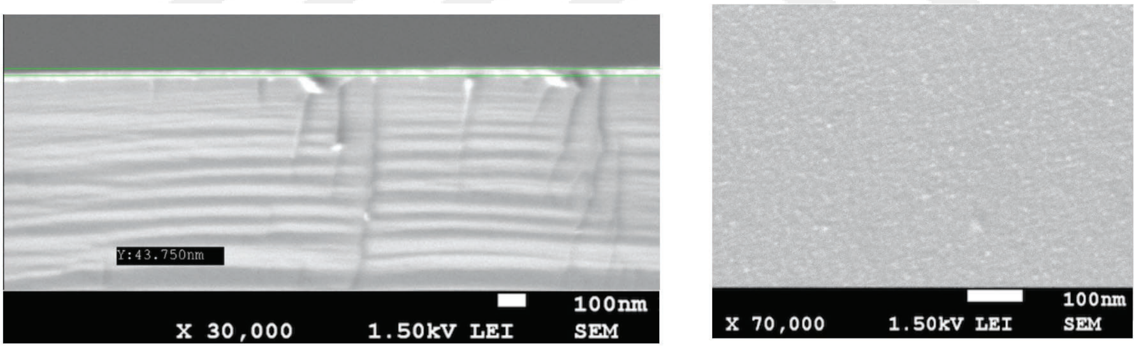

Figure 31: Side and top view of the 43.750 nm AlN coating.

Afterward, the DC power was adjusted to 300 W, the pressure was reduced to 5 mtorr, and the Ar/N ratio was given as 21/9 in order to increase the coating speed and to make the plasma more durable. In the test performed at the same temperature, it was observed that the plasma remained active for about 2 hours. Because of this test, AlN films with 100 nm and 200 nm thicknesses were formed using the same values.

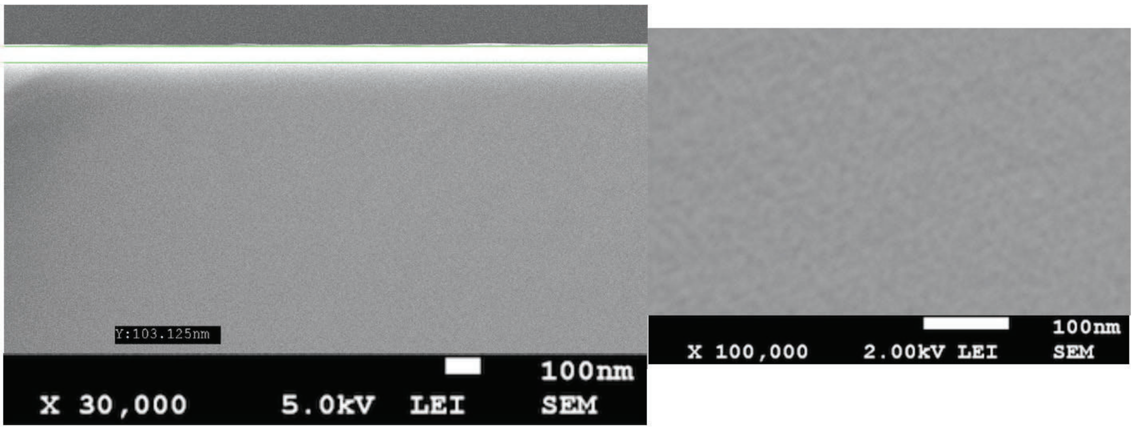

Figure 32: Side and top view of the 100 nm AlN coating.

In the lateral section of the 100 nm coating shown in Figure 32, the surface roughness appears to have improved significantly. The crystal orientation also appears to be more uniform. Based on these results, 200 nm coating was made with the same setup and surface images were taken (Figure 33).

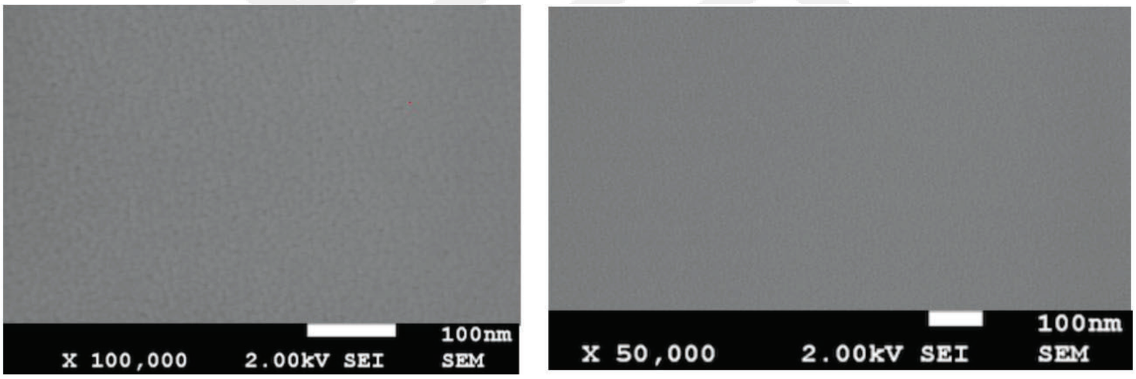

Figure 33: Top view of the 200 nm AlN coating.

As expected, the orientations were congruent. The C-axis orientation of this example is expected to be 002. For this test, an X-Ray diffraction (XRD) device will be used and the crystal orientations are examined to whether they are suitable for lamb wave generation. The last sample (which was coated at 200 nm) was not broken for lateral section imaging, IDT electrodes were grown on this sample, and wave velocity tests were performed.

3.2.2.1.2. AlN film orientation tests

In the ongoing studies, coating on Silicon (100) has been carried out and optimization studies have been completed. With the help of SEM images, it has been revealed that the coating is performed uniformly and has an orientation. In that section, the crystal orientation of the coated AlN film was investigated by XRD tests. And then, the electrodes were enlarged on the film, the production processes were determined and optimized.

With the procedure we optimized, 100 nm and 200 nm thick films (111) and (100) silicon wafers were used, respectively. The samples were examined with the XRD device of Marmara University Materials Engineering. The desired orientation of the AlN film has been got, the orientation of the AlN film (002) is seen at 36° (Figure 34). However, Silicon (111) orientation is more dominant at 28°. As the result got, the high noise level draws attention. We evaluated that the XRD device we use is not a thin-film-optimized device and the fact that we cut a part of the sample and put it inside the device, rather than as a whole, may have an effect.

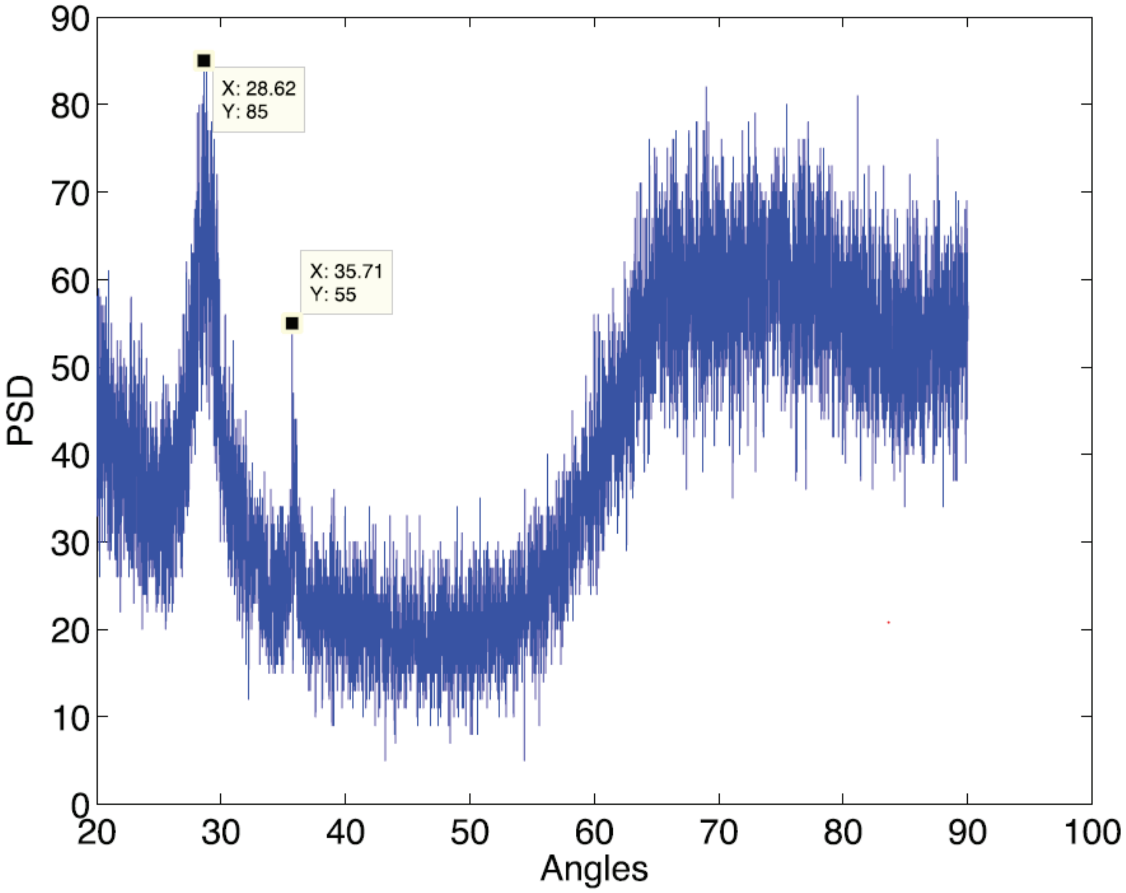

Figure 34: Crystal orientations of the structure consisting of 100 nm AlN thin film layer coated on Si(111) obtained by XRD device.

The next XRD test used a thin-film-optimized device that would not require wafer cutting. The silicon (100) and 200 nm AlN coated sample was tested in this way and the result given in Figure 35 was got. The Si (111) sample (the sample used in the first test) with a 100 nm AlN film coated on it was also measured in the second test. This result can be seen in Figure 35 (left).

When this figure is compared with the figure given in Figure 34, it is seen that the second measurements are much cleaner and the (002) AlN orientation (36°) is dominant. Figure 35 (right) As expected in the 200 nm AlN film-coated sample on the right, (002) AlN orientation is much more pronounced than the figure 35 on the left, which can be explained by the increase in thickness. In addition, Si (111) and Si (100) orientations are seen in reflections at 28° and 69°, respectively.

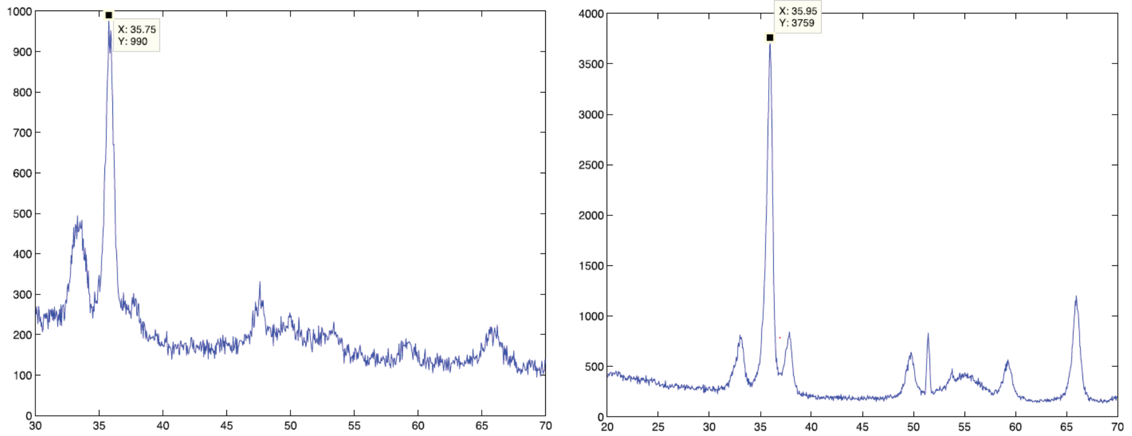

Figure 35: Crystal orientations of the structure consisting of 100 nm AlN thin film layer coated on Si(111) obtained by XRD device.

The results show that the thin-film crystal structure we got has the desired piezoelectric property. The electrodes were enlarged on the film, the production processes were determined and optimized.

For the electrical characterization studies of the film, the electrode was enlarged on the film and in this way, the frequency characteristics of the structure and the mechanical properties of the wave formed on the surface (such as velocity, damping) could be examined. For this purpose, metal electrode coating processes were carried out.

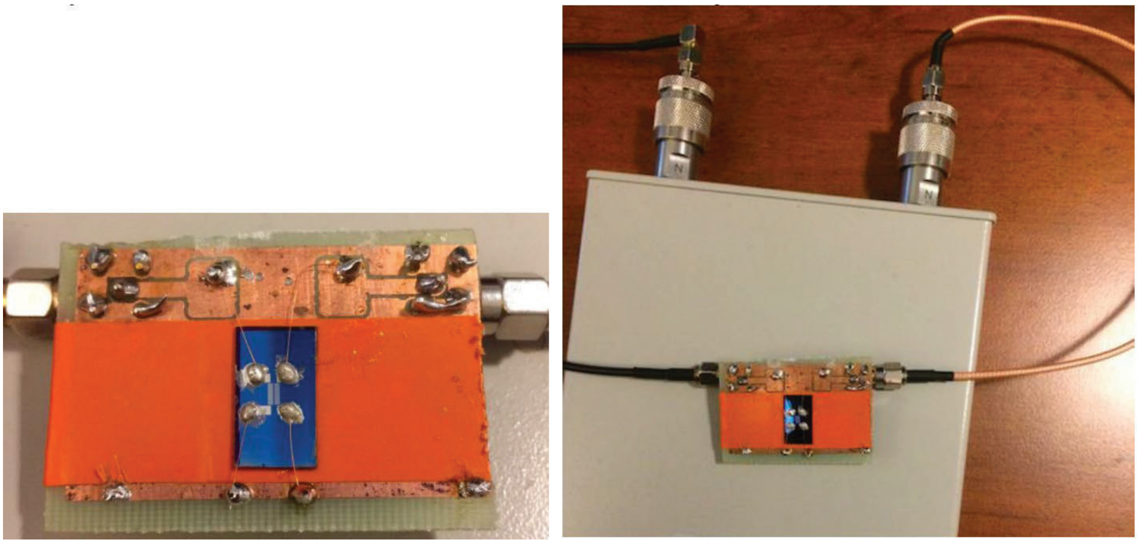

Figure 36: The test setup connected to the network analyzer of the thin film obtained as a result of fabrication.

The structure obtained by fabrication studies is shown in Figure 18. This structure was connected to the network analyzer and the results given in Figure 37-38 were obtained. The surface wave frequency driven here seems to be compatible with the results we obtained in our simulation studies. The response, which is around 1 dB, is the highest response seen in the 100-500 MHz range. It was thought that coating an insulator between AlN and silicon would strengthen the response. In ongoing production, the use of SOI both facilitated fabrication and provided insulation. The use of SOI was used as the etch-stop layer during the film's release and also facilitated fabrication. Thin film tests also include studies such as wave velocity measurement and extinction coefficient determination in the time axis.

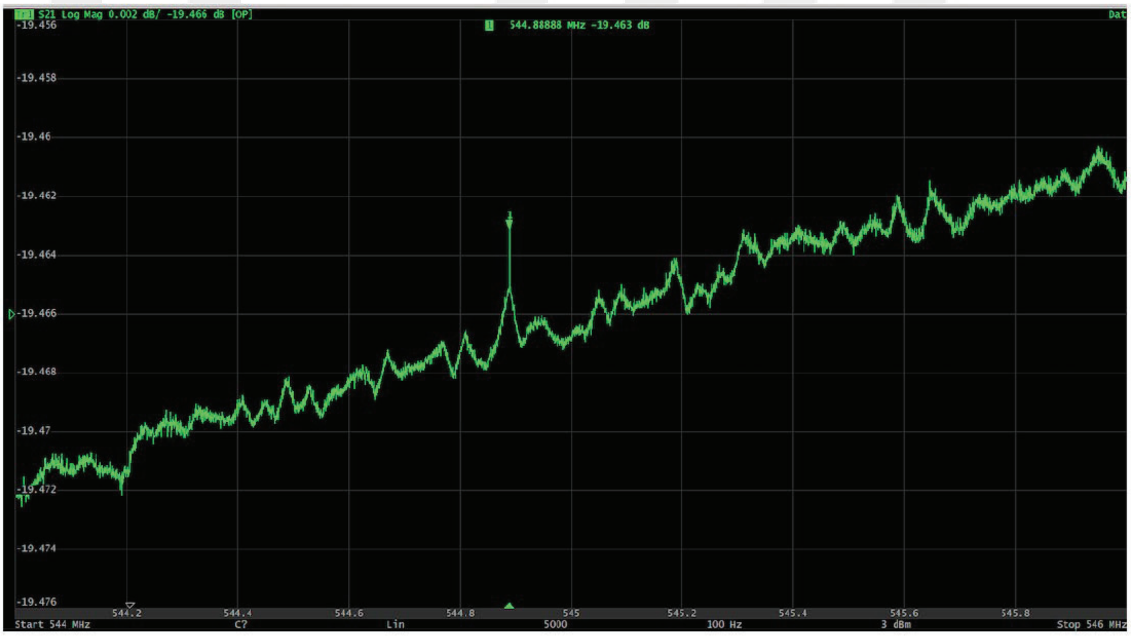

Figure 37: Obtained thin-film electrical characterization results. Magnitude plot of the S_{21} response at the relevant frequency.

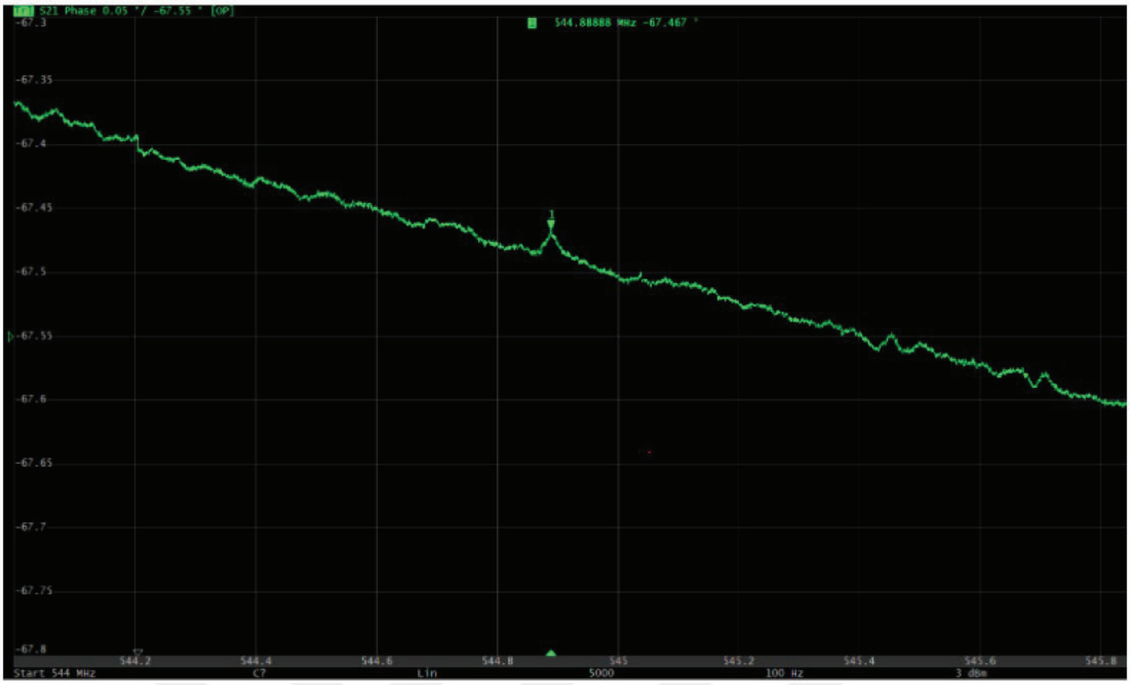

Figure 38: Obtained thin-film electrical characterization results. Phase plot of the S_{21} response at the relevant frequency.

3.2.2.2. Photolithography and etching

In this section, information is given about the mask designs for the structure we simulate and the studies for the lithography process. Lithography and shaping are necessary for characterization studies. Metal electrode coating and etching processes required to complete the works, such as film characterization, velocity determination studies, damping tests, were carried out within these studies. As a result, it has been shown by characterization studies that the thin film works as expected.

Studies carried out: 1. Positive mask usage, creation of electrodes by etching directly on the surface 2. Negative mask design, optical lithography, and photoresist (PR) shaping and application of lift-off method 3. E-beam lithography and PMMA shaping and lift-off application of the method.

Let's explain these studies in order:

3.2.2.2.1. The Processes of using the positive mask and etching the electrodes on the surface

Electrode amplifications were performed primarily on 100 nm AlN-coated Si wafer, which was broken for sampling during XRD studies. Before, during and after the coating, it was kept in acetone and then in isopropyl alcohol to be cleaned from possible organic particles.

After cleaning, the AlN coated wafer was first coated with 200 nm Cr under $8x10^{-6}$ Torr pressure using the E-Beam Evaporator.

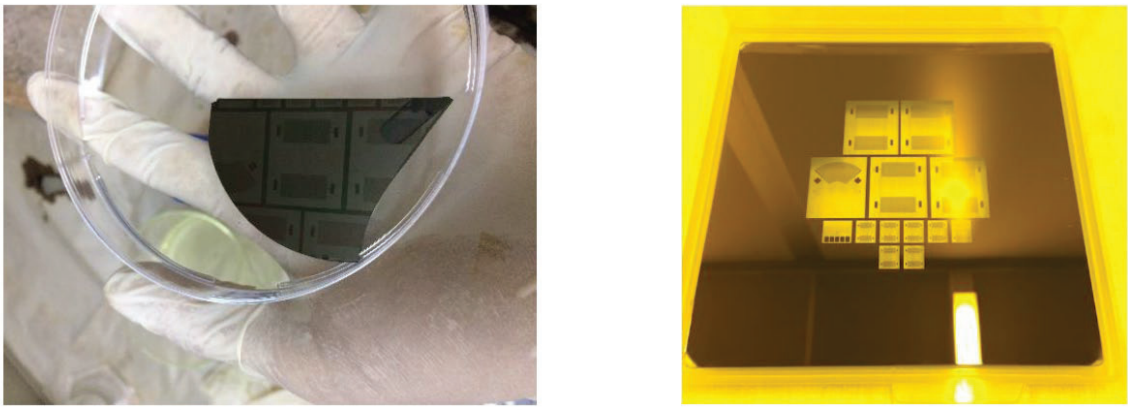

Figure 39: The positive mask we used in the lithography process (Right). Sample (Left) coated first with Cr, then PR and shaped by lithography.

AZ5214 Positive PR was used in the photolithography process. It was spun for 45 seconds at 4000 rpm and the surface was covered with 1.4 um PR. It was baked at 110 °C for 50 seconds. Shaping was done by exposing it to the 1 kW UV lamp of the Midas MDA-60 MS Mask Aligner & Exposure system for 4.5 seconds. PR was developed using AZ 726 MIF Developer. Cr etchant (Ceric ammonium nitrate (CAN) ($H_8N_8CeO_{18}$) : Perchloric acid ($HClO_4$) : Deionized (DI) water (H_2O) / 10.9% : 4.25% : 84.85%) at 60 nm/min rate in 3 minutes 20 seconds using Cr etchant and the sensor was produced (Figure 39).

In the last step, the sample was kept in the solution in a controlled manner so that the AlN thin film and the Cr etchant did not come into contact. Controls were made with a microscope and the process was characterized. The generated sample was placed on the circuit board and frequency measurements were made using the Vector Network Analyzer (Figure 40).

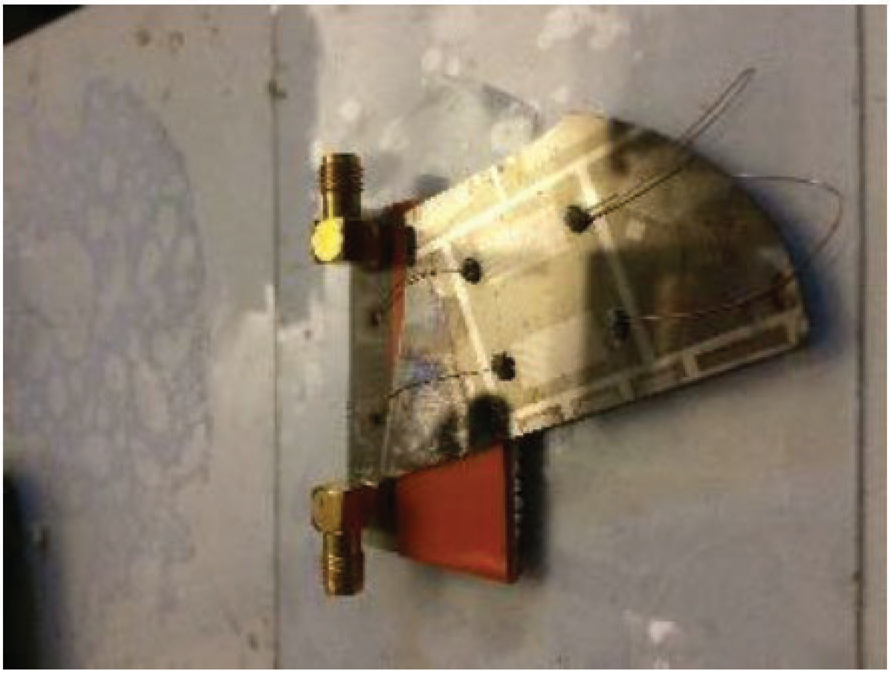

Figure 40: Example set to connect to network analyzer after Cr Developer.

However, no results were got in the measurements. In the last stage, electrode enlargement with another process was considered, since it was thought that there might be a problem in the controlled Cr dissolving process.

3.2.2.2.2. Negative mask design with PR shaping via optical lithography and application of lift-off method

It was designed a mask suitable for negative photolithography to avoid Cr solvent, and to enlarge the electrode by removing PR instead of Cr etch with the lift-off technique. By the mask, it is produced an LW device with a wavelength of 10 µm. The design was also carried out for LW devices with a wavelength of 30 µm which is the lower frequency in the same mask (Figure 41). In this process, a 200 nm AlN coated sample was used on Si (100), which has not been damaged yet. Negative PR is developed from AZ5214 code PR by a 2-minute pre-firing process at 90 °C.

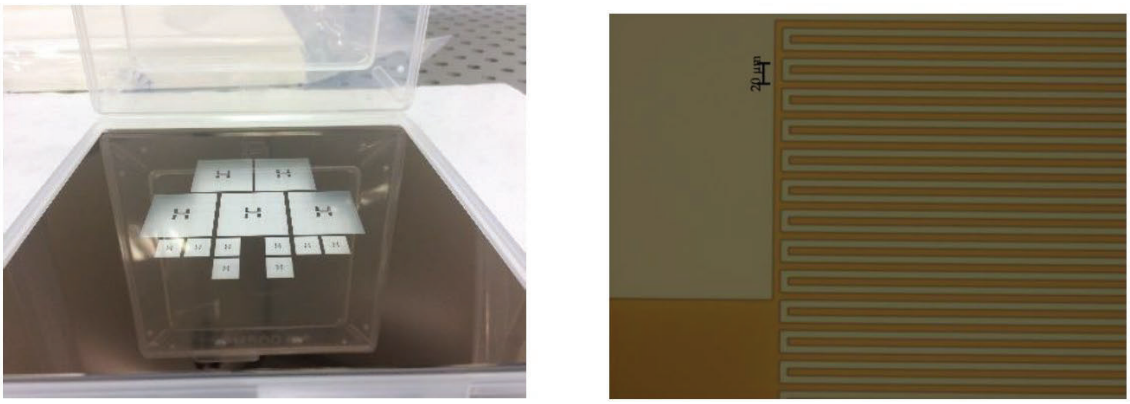

Figure 41: Example set to connect to network analyzer after Cr Developer.

It was shaped by exposure to UV for 14 seconds (2 seconds with mask and 12 seconds without mask) and again developed using AZ 726 MIF Developer for 45 seconds. In the microscope photographs given on the right in Figure 42 after the bathing process, it was noted that there was a mishap related to the pattern thicknesses after shaping with PR.

Since the PR was not sufficiently dissolved, it was abandoned the planned Cr coating process after the bath, to remove the PR from the surface and to repeat the process. It was noticed that the patterns on the wafer did not disappear even though the wafer was left in acetone for a sufficient time and kept in an ultrasonic bath for cleaning the PR on the surface. Therefore, it was understood that the patterns seen after the acetone bath were not PR and that the AlN film had some etch.

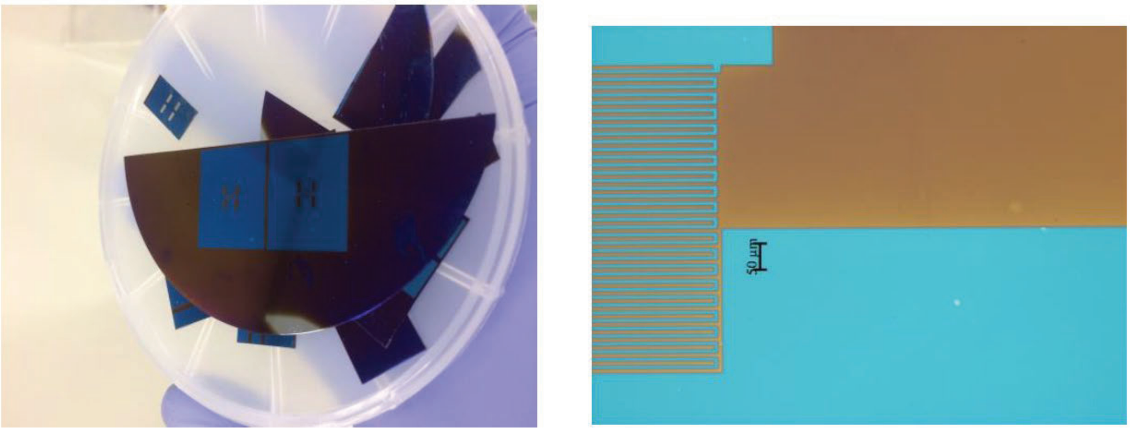

Figure 42: Image after cleaning of the sample damaged by the developer: Dissolved AlN (Brown) and undissolved AlN (Blue).

Since we only use PR and PR-developer, the effect of these chemicals on AlN film was investigated. We noticed that the AZ 726 MIF Developer solution we used in the bathing process contains TMAH (Tetramethylammonium hydroxide) and this solution etch the AlN layer (Figure 42). The thickness was measured with an ellipsometer, and the AlN thickness in the regions we thought were dissolved AlN was determined to be around 84 nm (Figure 43). Because of this information, a new procedure that does not require the use of PR has been planned.

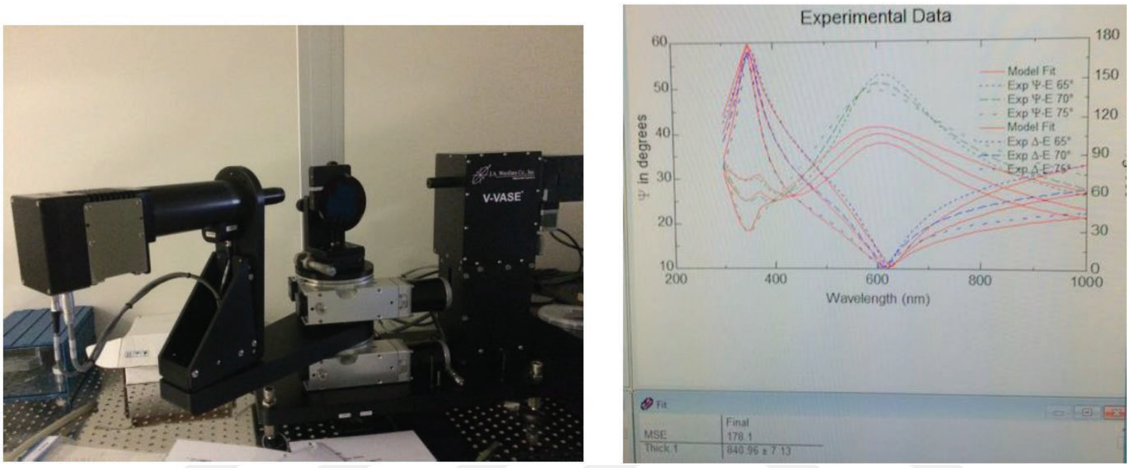

	Final
MSE	178.1
Thick 1	840.96 ± 7.13

Figure 43: Ellipsometer device and measurement result.

3.2.2.2.3. E-Beam lithography patterning with PMMA and application of lift-off method

To avoid AZ 726 MIF Developer, it was decided to change the lithography method to E-Beam Lithography (EBL). In the new method, the lift-off technique will be used again, but this time PMMA, which has a ketone solvent and does not damage the AlN film, is considered instead of PR. Since the PMMA surface is shaped by dosing with electrons, the EBL device was used. Instead of making a new coating, the intact parts of the wafer (with undissolved AlN of blue color) were cut and processed on them (Figure 44). During the cutting process, care was taken not to lose the crystal orientation in the new parts.

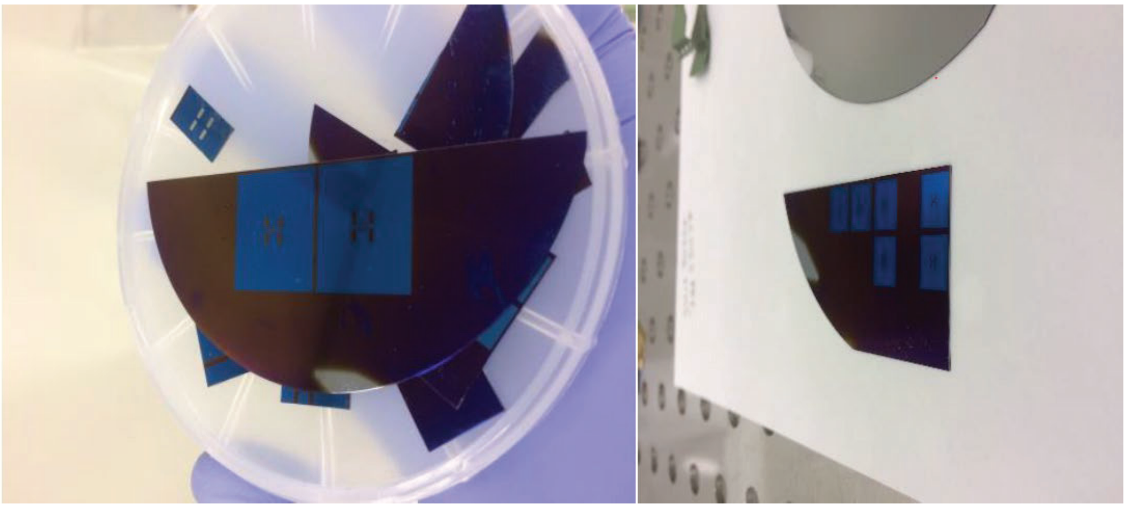

Figure 44: Wafer during the cutting process.

Before EBL, Copolymer (MMA (8.5) MAA EL11) and 950k PMMA A2 were spun, respectively. The spinning process was carried out in two steps. In order for PMMA and MMA to spread smoothly on the surface, solutions were dripped on it for the first 4 seconds, at 1000 rpm, and then it was allowed to spin on its own for 50 seconds at 4000 rpm.

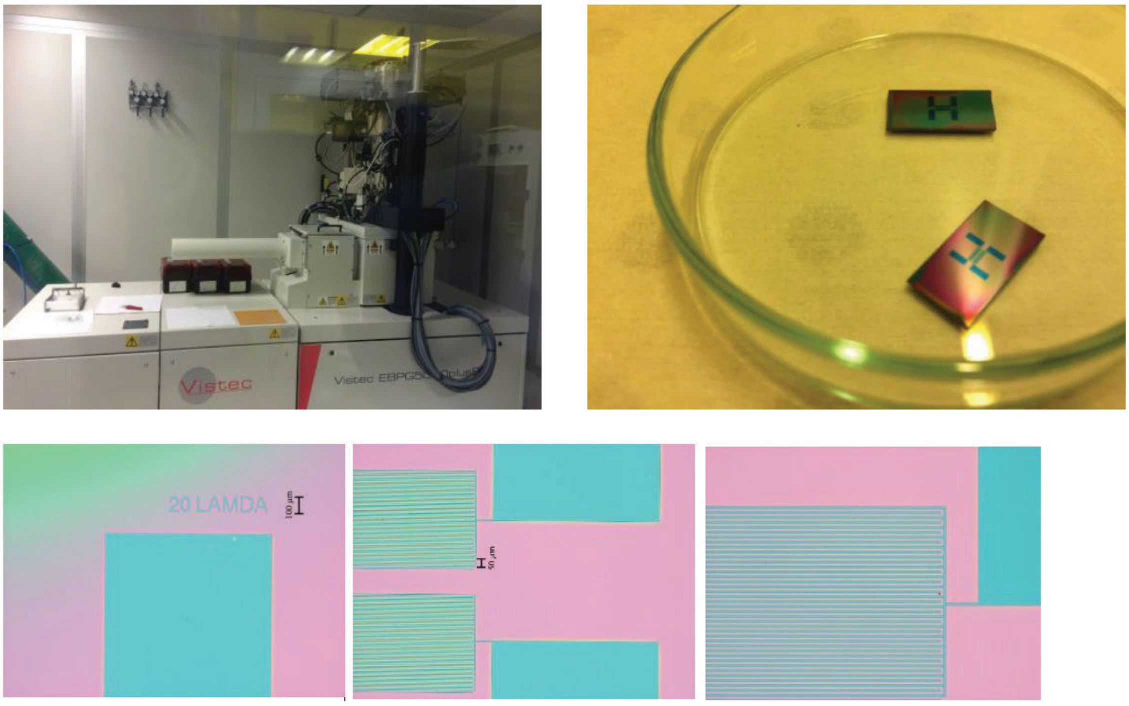

Figure 45: Pre-coating microscope images are as follows.

Then, the liquid solution was completely evaporated by keeping it at 170 C for 3-4 minutes, and ready samples were obtained for EBL shaping with 0.5 µm thickness. In the EBL process, shaping was performed with the Vistec EBPG 5000PlusES tool at a dose of 850 uC/cm2. After shaping, PMMA on the surface was bathed in a mixture of MIBK (Methyl isobutyl ketone) and isopropyl alcohol (Developer) for 1 minute. Then, as a stopper, our sample with a shaped 500 nm thick PMMA surface was obtained, which was kept in pure isopropyl alcohol for 30 seconds and ready for Cr coating (Figure 45).

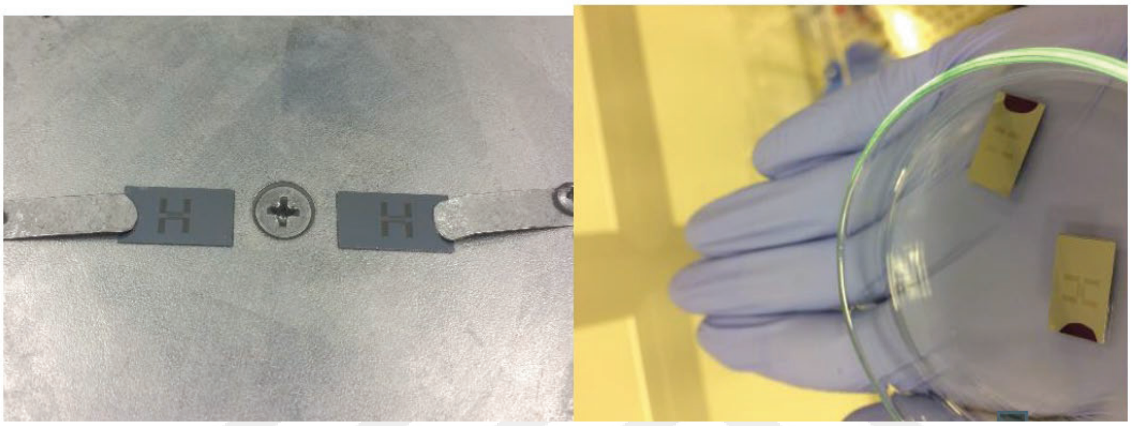

Figure 46: (Left) Dummy wafer plate used for coating. (Right) Wafer pieces after coating.

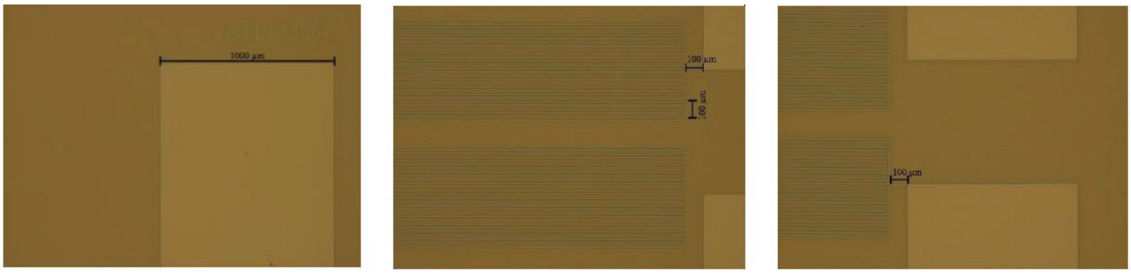

Figure 47: Microscope images after Cr coating.

The surface of the sample was coated with 150 nm chrome under 8 x 10^{-6} Torr pressure using an e-beam evaporator (Figure 46-47). Maximum 1:3 ratio required for lift-off was achieved with PMMA at 500 nm. Afterwards, the coated samples were thrown into acetone for the lift-off process and the PMMA under the chrome on the surface was expected to dissolve (Figure 48).

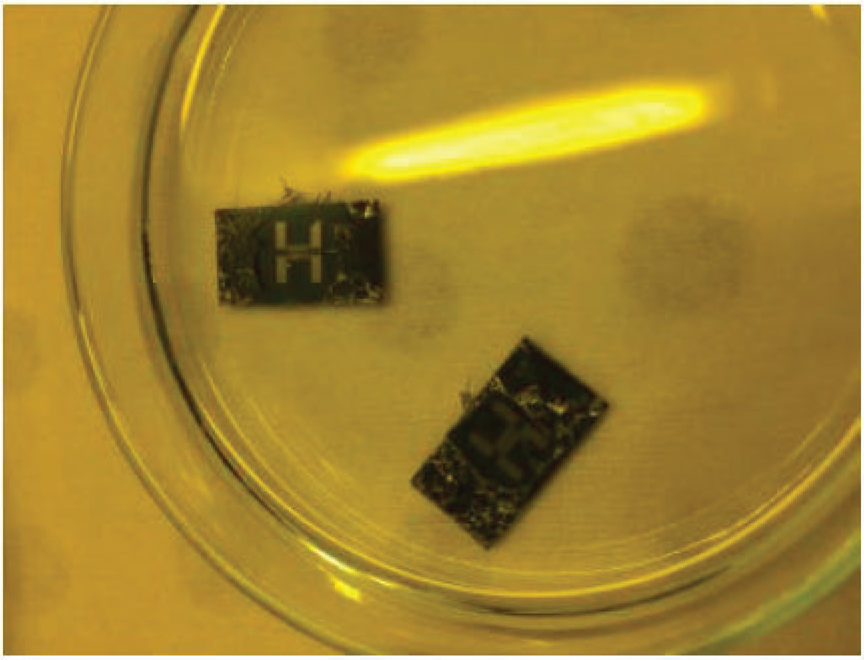

Figure 48: Acetone bath.

After one hour of waiting, it was observed that the fine Cr on the surface was removed and the electrode coating deteriorated during the ultrasonic bathing process of the lift-off process. Two possibilities have been considered for this:

a. The 150 nm Cr coating was too thick and did not fit proportionally with the 500 nm PMMA.
b. Oxygen plasma treatment was not done before Cr coating and PMMA residues remaining on the surface caused the Cr, which should not be removed, not be able to adhere to the AlN surface.

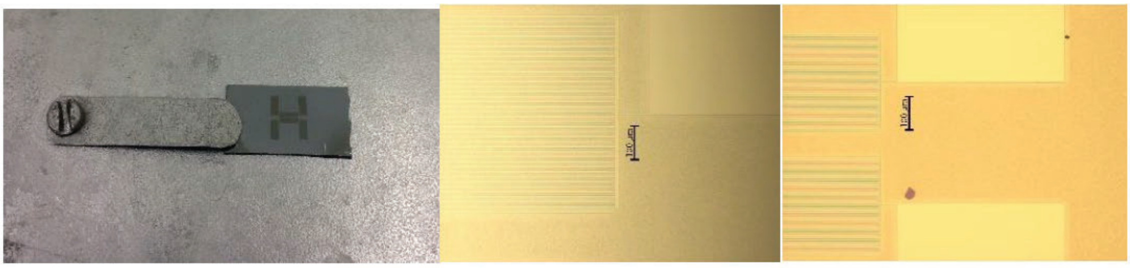

Figure 49: (Left) Sample after Cr coating process, (Middle and Right) microscope images.

Figure 50: IDT electrode enlarged sample with success after lift off.

Afterwards, the EBL procedure was repeated. By applying oxygen plasma for 10 seconds, the surface was completely cleansed of residues. Using the E-Beam Evaporator, the Cr coating made under 8 x 10^{-6} Torr pressure was reduced to 100 nm (Figure 49-50). Thus, two possibilities that could cause this error were eliminated.

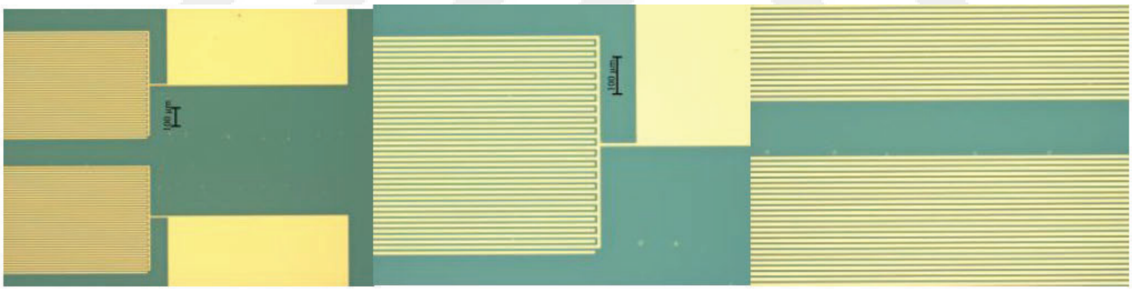

Figure 51: Microscope images of successfully magnified samples of the IDT electrode.

After placing the wafer coated with Cr in acetone and waiting for 1 hour, it was seen that our design was formed successfully. An ultrasonic bath was made with acetone in order to get rid of Cr residues of the kept sample. Then, the microscope images are as in Figure 51 after it is bathed in isopropyl alcohol for cleaning and dried with nitrogen.

4. RESULTS

4.1. Fabrication

In our thesis, ready-made epitaxial film on the silicon chip was taken as a template to facilitate fabrication studies. Thus, crystal orientation was as smooth as possible. However, although the characteristics of the materials are known, characteristic tests for the coated film should be performed. First, the crystal orientation of the material should be tested. This test was examined by the X-Ray Diffraction (XRD) method, it was determined that there was no orientation problem. In addition, the coated surface morphology and roughness were checked. In addition, velocity tests and damping tests of the Lamb Wave were also carried out. LW speed is an important design parameter for the project and its value has affected the design and simulation studies to be performed.

For this reason, an experiment to measure the speed of the acoustic wave is planned in our thesis. This setup, illustrated in Figure 52, includes two conventional 2-port LW devices on AlN coated film. These LW devices have the same center frequency, but while the delay line of one of their devices is 10λ, the delay line of the other is 20λ. The LW speed was determined by measuring the time difference in the delay lines with two separate transmit and receive tests to be carried out with two separate experiments. In this method, two LW devices must be produced far enough from each other to minimize the reflection effect. This speed value has been verified by measuring the center frequencies of the LW devices in the spectrum analyzer. The attenuation of LW waves was investigated using the same experimental setup and how much the amount of attenuation changed depending on the distance was measured at the center frequencies of the LW devices tested.

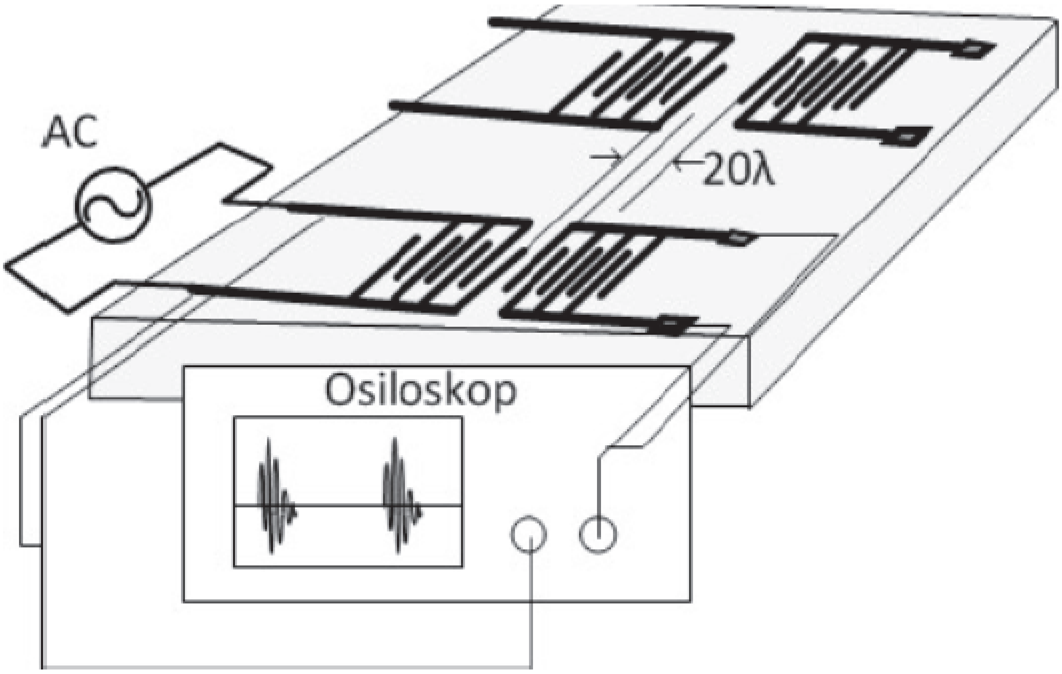

Figure 52: Demonstration of the circuit assembly to be set up to measure the LW speed.

The velocity and damping values got in thin-film characterization studies are important in terms of their use in design and COMSOL simulation studies. However, if a problem is encountered, the use of velocity and damping values reported in the literature will not be a problem for further studies, although it is not sensitive enough.

The second stage of the fabrication process is to produce according to the design parameters clarified by simulation studies. During the production, ready-made silicon chips coated with 500 nm film were used. The bottom of the thin film layer was evacuated as desired and the electrodes of the CT structure were placed. For the fabrication of the structure proposed in Figure 53, the following production steps are designed:

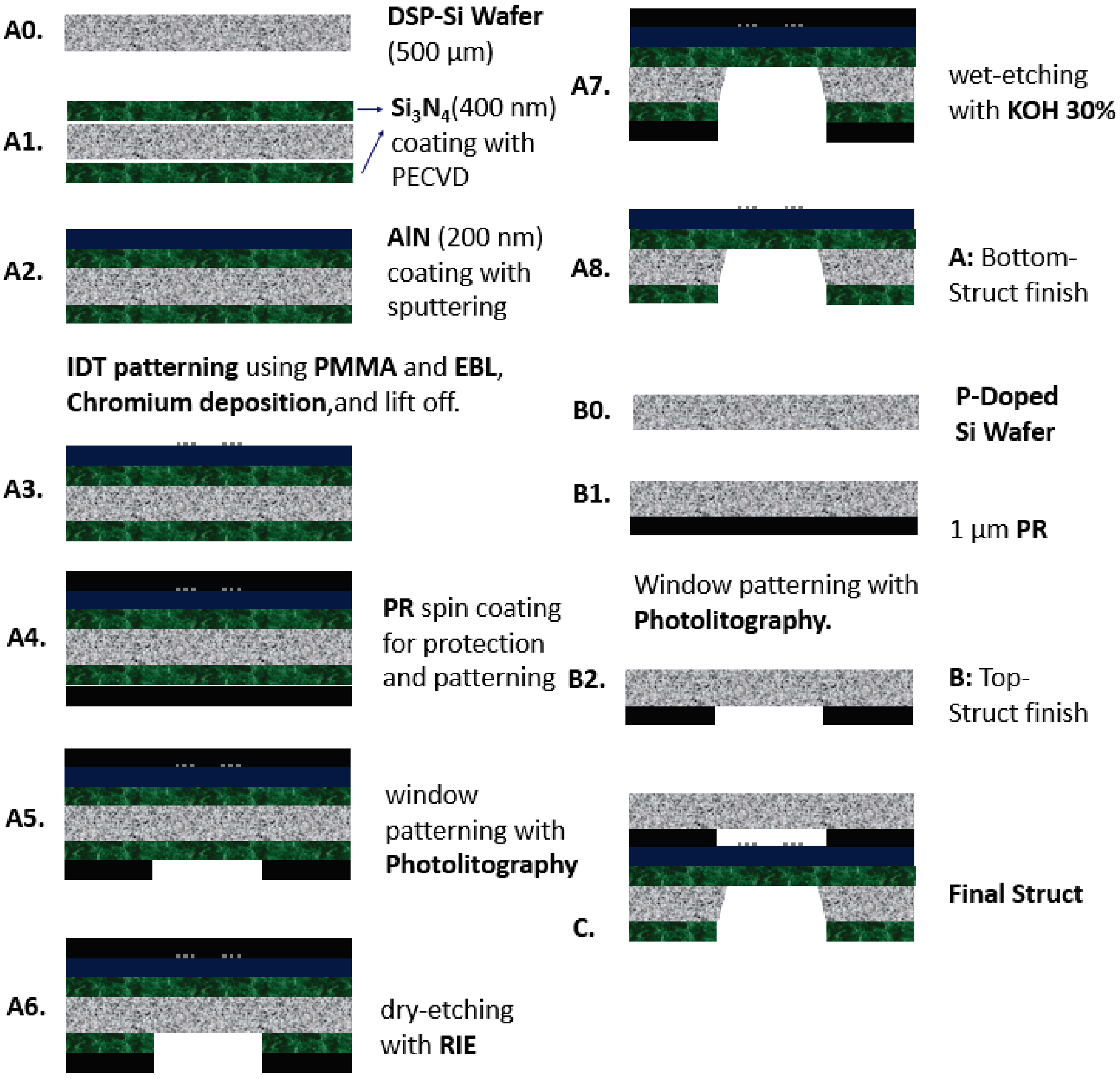

Figure 53: Fabrication processes of the Adjustable-Phased Lamb Wave Device via Analog-Voltage-Controlled.

A1. 400 nm Si_3N_4 coating to both sides of a DSP (Double Side Polished) Si wafer with Plasma-Enhanced Chemical Vapor Deposition (PECVD). The top coating is used as an etch-stop. The under-coating is used window patterning stage via photolithography for wet etching.

A2. 200 nm AlN coating on Si_3N_4 (Sputtering).

A3. IDT patterning using Polimetil Metakrilat (PMMA) and Electron-Beam Lithography (EBL). First, Chromium deposition for IDT Electrodes, and then, the surface is covered with photoresist and shaped with EBL, then IDT is shaped with the lift-off method.

Afterwards, the photoresist was cleaned and the IDT structures and the upper electrode were obtained as Figure 54.

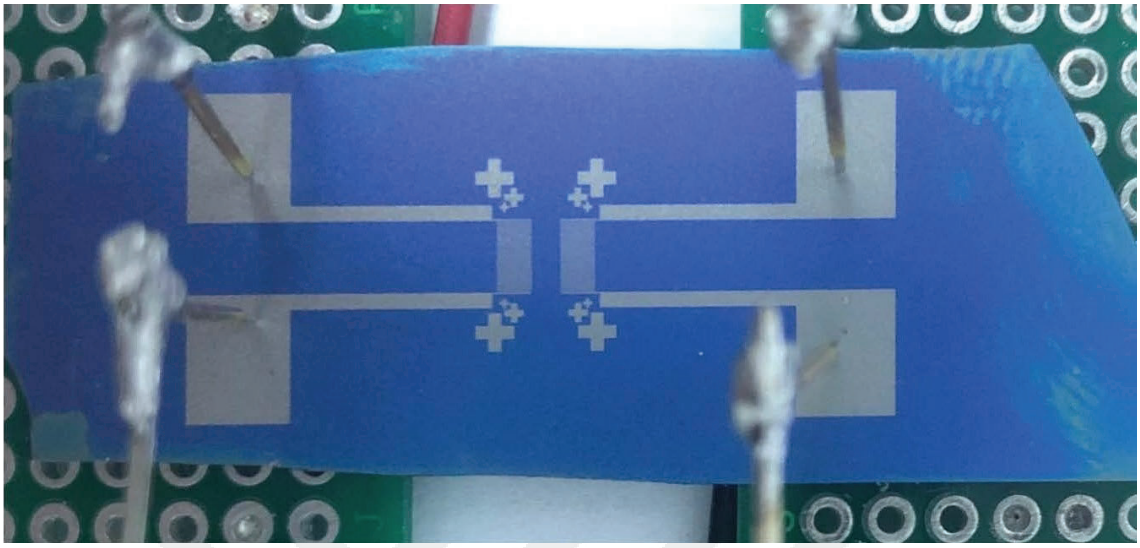

Figure 54: The final version of Cr IDT coated LW device after EBL.

A4. 1 µm photoresist (PR) protection layer on the IDT electrodes.

A5. Backside window patterning and, A6. dry etching of Si_3N_4 under the electrodes,

A7. Bulk wet etching of Si under the electrodes (using 30% KOH). Anisotropic bulk silicon etching: Anisotropic silicon etching is a widely used and well-characterized technique for machining bulk silicon in MEMS technology, using chemicals such as Potassium Hydroxide (KOH), TetraMethyl Ammonium Hydroxide (TMAOH). It is a wet etching technique and is performed by immersing the sample in a chemical bath and waiting (Figure 55). The most important advantage for our process is that the underlying surface is very flat because of the crystal plane and the process can be controlled very well. After this step, the remaining silicon height on the chip should be measured. This distance is important to determine the distance between the electrodes of the CT structure.

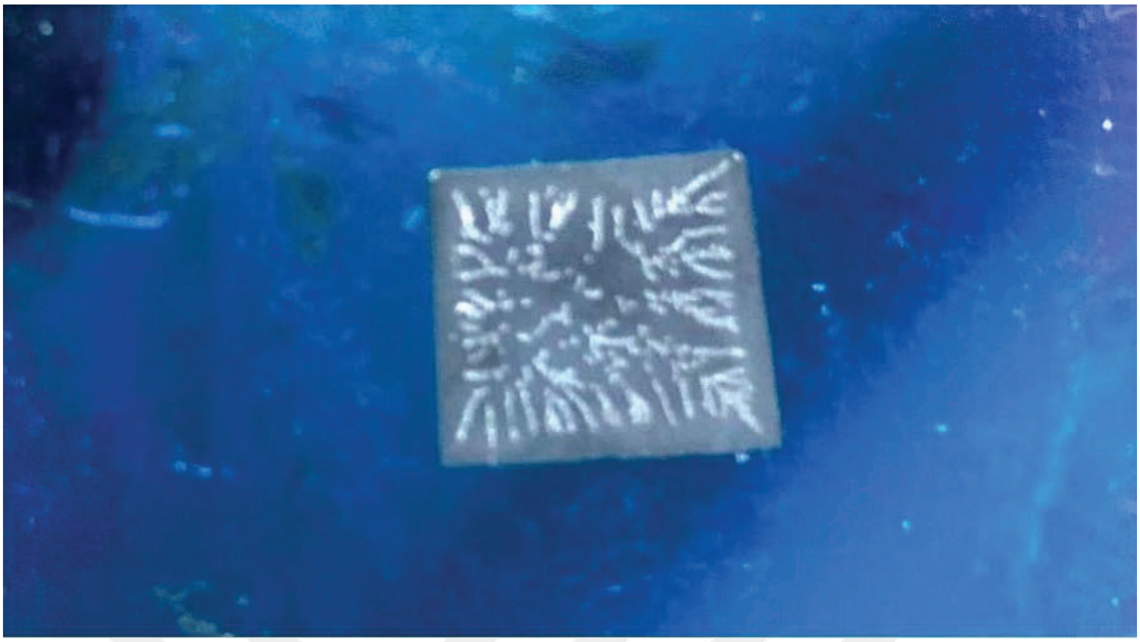

Figure 55: Si layer with SiN framework to be wet-etched with KOH.

A8. The SiN under the AlN film stops the etching operation. Acetone rinse.

B1. 1 µm PR is coated and cured on a doped Si wafer.
B2. Pattern a window, which has a bigger area than IDT electrodes. Put the top structure (B) on top of IDT electrodes on the bottom structure.
C. The window on the top structure will be aligned on the IDTs. The top structure forms a CT structure that is connected to a DC analog voltage (DC => p-doped Si, GND => Chromium coating on the bottom structure). The bottom structure has two ports for RF signals (input/output).

Post-production thin film thickness was tested with a surface profilometer. The morphology and purity of the film were checked using an X-ray fluorescence device. Apart from that, the membranes were examined optically. Processes planned for production are defined processes that are frequently used in fabrication processes. Therefore, there was no problem. However, if an error was detected in the test processes of the post-production devices, the production process was investigated against the possibility of an error and the production was repeated if necessary.

Another fabrication process was made for conventional two-port LW devices with the same design parameters but without an adjustable delay line. The manufacturing processes of these devices are the same, but only the steps for creating CT structures have not been implemented. The LW devices to be got with this production stage were used in test studies to set a standard for comparison.

The first step in the testing and verification process was the reflectance and transmission impedances of LW devices were measured with Network Analyzer (4 GHz) and RF Signal Generator (1 GHz) (Figure 56). At this stage, besides testing the functionality of LW devices, the classical LW device and the LW device with CT structure were compared in terms of reflection and transmission impedances. It is expected that the reflection parameters of these two devices would be similar.

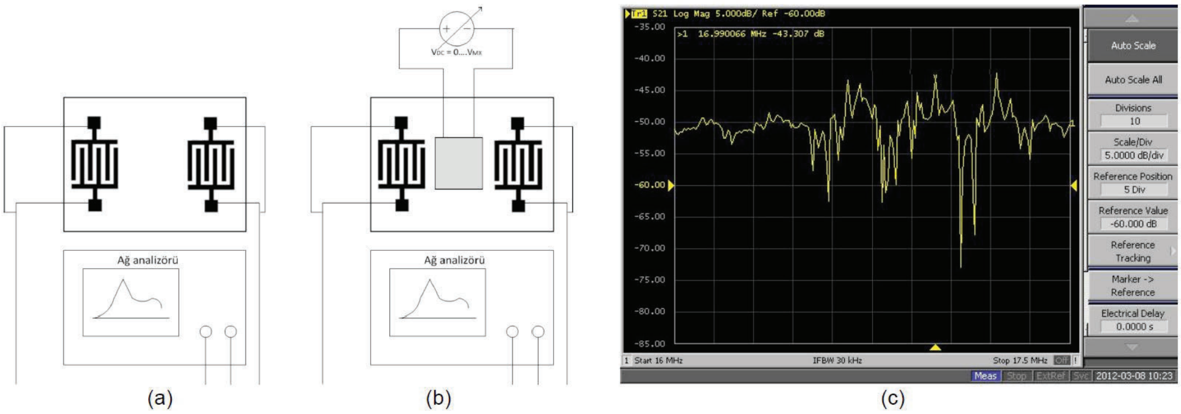

Figure 56: (a) The transmission characteristics of the classical LW device and (b) the adjustable delay line LW device using a spectrum analyzer and (c) the transmission characteristic of the classical two-terminal SAW device with a design frequency of 16.8 MHz manufactured on a piezoelectric (ST-Quartz material) wafer.

In the second stage, the amplitude and phase values of the transmission impedance and the phase change were investigated by applying the maximum precipitation value to the DC voltage input of the structure containing the CT. It should be seen that the applied voltage value can change the phase. In addition, it has been verified by experiments that a sinusoidal is applied to the input at the design frequency and an adjustable phase difference occurs in the output voltage. These measured characteristics are also compatible with the characteristics obtained in COMSOL simulation studies.

4.2. Simulation

Preliminary simulation studies were carried out for the tests of the aforementioned structure and concept, the 3-dimensional version of the model, the 2-dimensional cross-section, and the element mesh used are shown in Figure 57. In our preliminary simulation studies, a two-dimensional model of the system was used to reduce the computational load. In this model, the center frequency is chosen as 100 MHz. Since the thin film thickness we used in our thesis is 500 nm, the same film thickness was used in the simulation model.

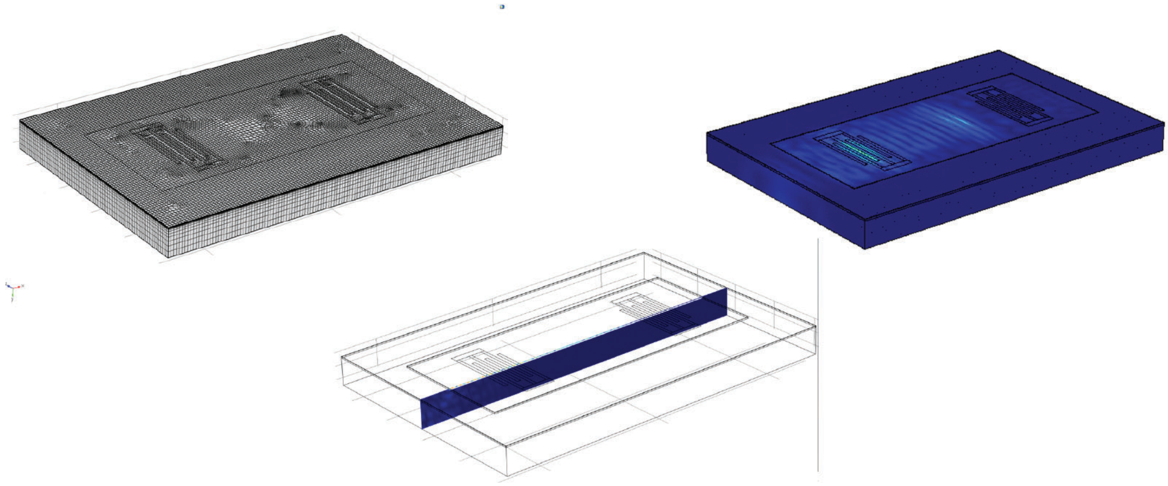

Figure 57: Element mesh representation of the 3D model (upper left). The progression of the Lamb Wave in the established model (upper right). Section (bottom) used in 2D simulation studies to reduce simulation time and complexity.

In the light of these parameters, phase velocity was calculated as 985 m/s by using dispersion curves for Lamb Wave A_0 mode. The dispersion curve got for the Lamb Wave A_0 mode can be seen in Figure 58. The value calculated by the numerical method was found to be quite close to the approximate velocity (971.3 m/s) calculated analytically using the formula given by the expression (4). The wavelength associated with this can be calculated as 9.85 µm.

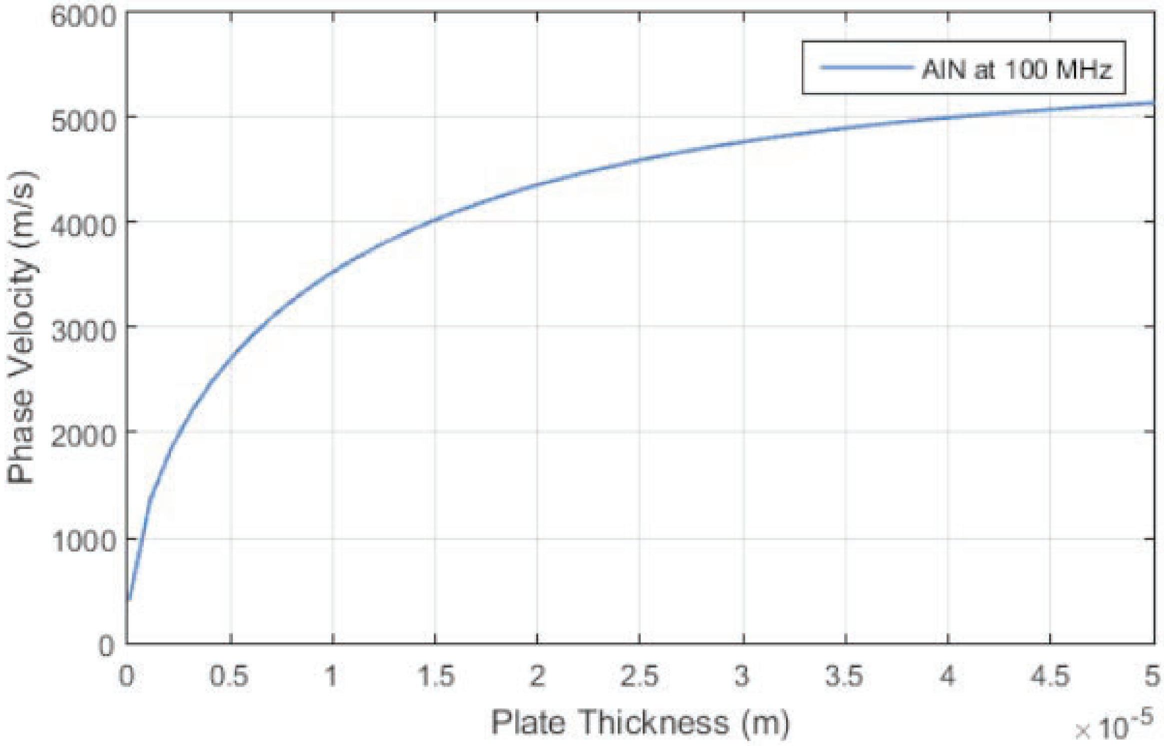

Figure 58: Dispersion curve obtained by numerical solution of Rayleigh-Lamb Equations. This curve is obtained for LW A_0 mode using f=100 MHz and AlN film mechanical properties.

The distance between the IDT fingers was determined by the wavelength. The distance between two opposite IDTs was chosen as 50 wavelengths. It is foreseen that the 50λ long delay line will attenuate below 50 dB at the design frequency (Figure 59.a). The simulation time was chosen as 37.5 cycles, 37.5/100 MHz in seconds. This time is sufficient for the generated Lamb Wave to reach the counter electrode and for the received signal to reach a continuous state.

The maximum mesh element size used in the simulation studies was calculated as 123.2 nm (Figure 59.b). Considerations in this calculation are that the IDT fingers of width λ/4 should be well-sampled, and it should be ensured that enough mesh elements are taken across the film thickness, and the maximum mesh element size should be chosen small enough then the wavelength.

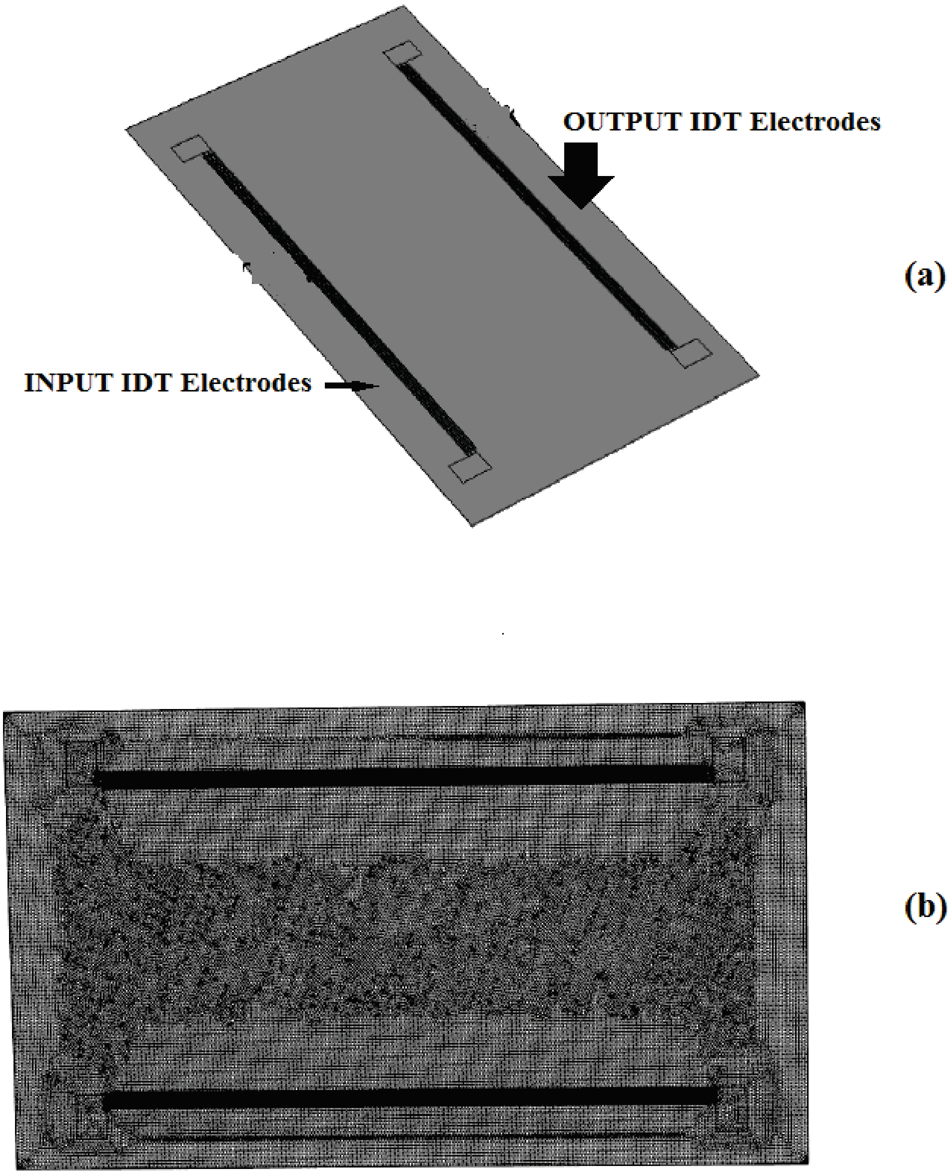

Figure 59: (a) 3D representation of IDT electrodes. (b) The view after meshing.

The simulation calculation time interval (t_{step}) was set as 0.2 ns. Mechanical stiffness damping coefficient was used as 1.6×10^{-12} sec. A sinusoidal input with an amplitude of 10 V at 100 MHz is applied to the model and the output voltage is observed. All parameters used are given in Table 2.

Table 2: Simulation parameters of the model established for the preliminary simulation studies.

Lamb Wave phase velocity	985 m/s
Center Frequency	100 MHz

Wavelength	9.85 µm
IDT Finger Thickness	2.4625 µm
IDT Finger-to-Finger Distance (Pitch)	9.85 µm
Number of IDT Fingers	3
Delay Line Distance	492.5 µm
Piezoelectric Film Length	1324.8 µm
Piezoelectric Film Thickness	500 nm
Simulation Time	375 ns
Simulation Time Step	0.2 ns
Maximum Network Element Size	123.12 nm
Stiffness Damping Coefficient	1.5915 ps
Distributed Load Trials	0 kPa, 0.1 kPa, 1 kPa, 4 kPa, 7 kPa, 10 kPa

(Continue)

In Figure 60, the two-dimensional model and the dimensions used are given. These dimensions are shown as AlN film thickness 500 nm, film length 1324 mm with IDT structures, delay line length 492.5 µm, and two adjacent IDT finger distances of 9.85 µm.

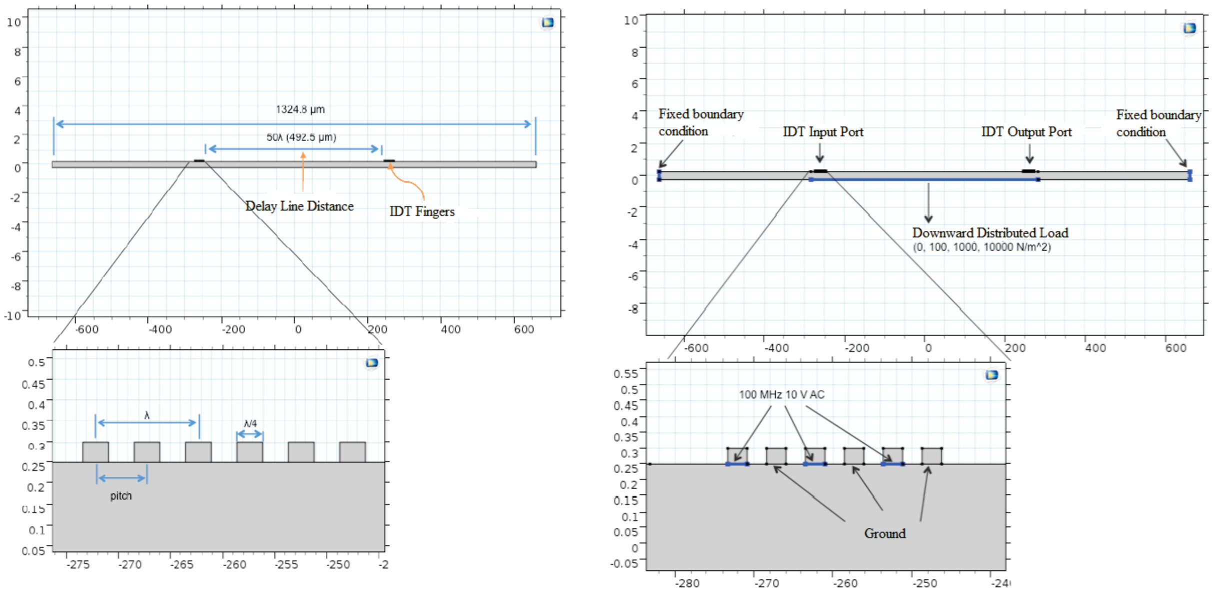

Figure 60: Constructed model and IDT fingers with measurements.

Boundary conditions are fixed from the right and left sides of the membrane. A homogeneous force was applied along the IDTs and the delay line and phase measurements were made between the input-output voltages for various values of the stress created by the force. The stresses and propagation of the LW wave for 0 and 10 kPa values are shown in Figure 61.

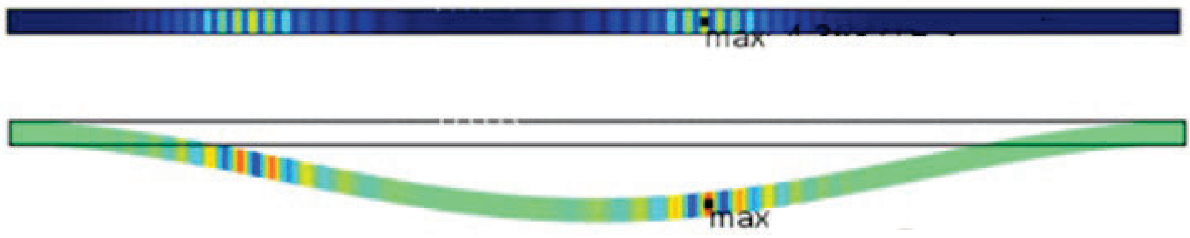

Figure 61: Stretching in the film with no distributed load (top) and 10 Kpa load (bottom) (stretching is exaggerated for clarity). Progression of the generated single cycle lamb wave.

When the output voltages of the adjustable phase LW device excited with the same input are measured for various force values, it is seen that it reaches the output electrode with a delay of 7 ns for the highest force and 0.4 ns for the lowest force (0.1 kPa).

In Figure 62, the output voltages read for various distributed load values are given one above the other. The phase difference between the output voltages is clearly visible. As the distributed load increases, the speed of the Lamb Wave slows down. This result is consistent with the results got in the literature characterizing the LW velocity under stress [48].

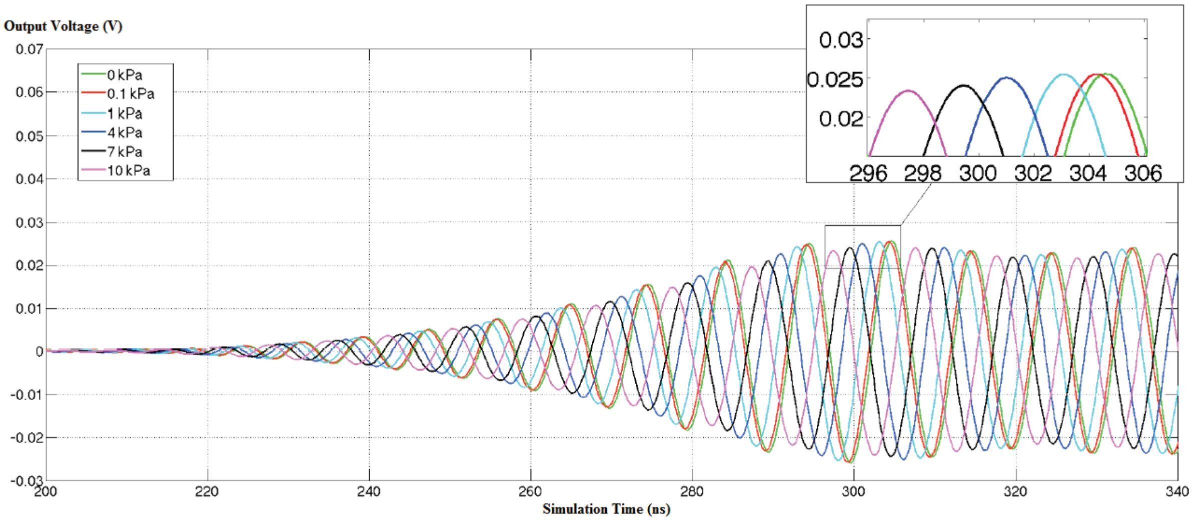

Figure 62: Output voltages read for various distributed load values between 0-10 kPa.

The power-phase relationship is obtained by reading the delay values of the output voltages from Figure 62. It is seen in Figure 63 that the phase difference value increases as the applied force increases. It is also seen that the force-velocity relationship is almost linear.

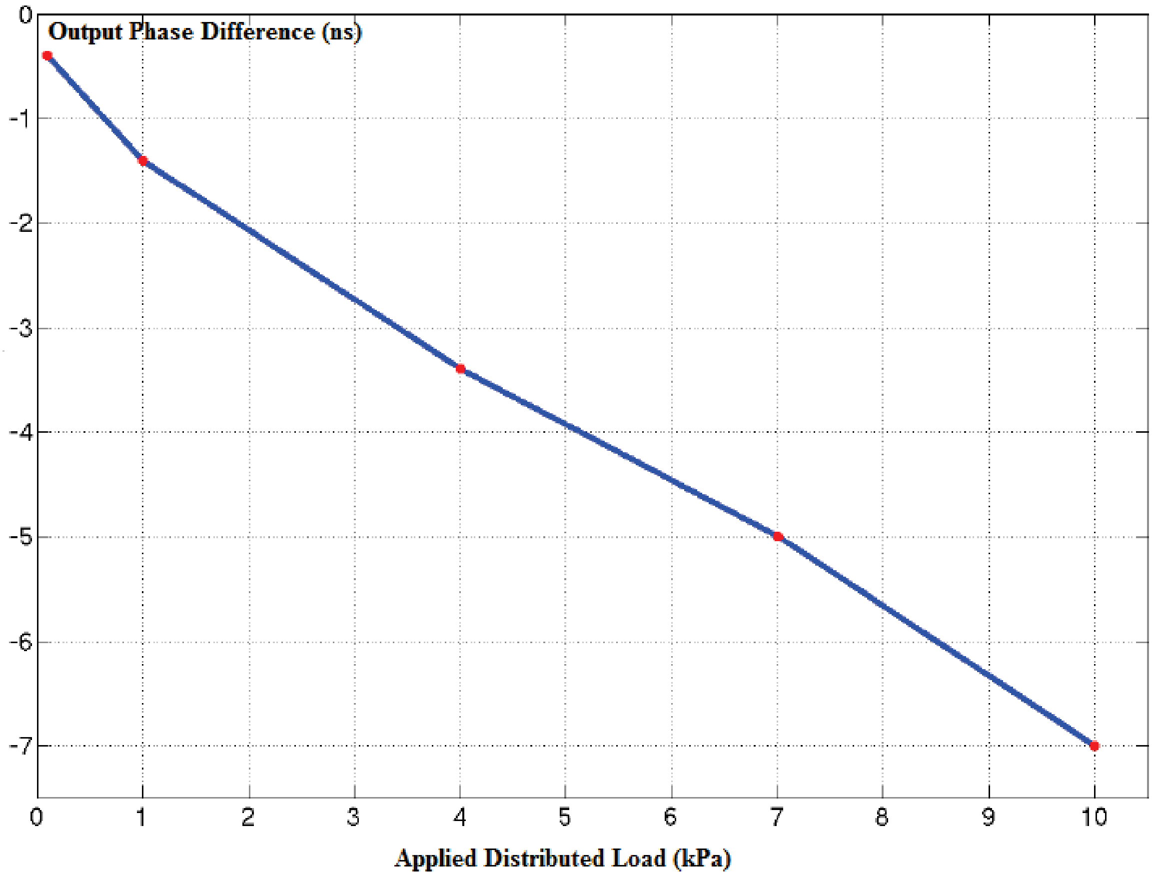

Figure 63: Phase differences read in output voltage for various distributed load values between 0-10 kPa. It is seen that the phase differences-distributed load relationship is almost linear.

Although the preliminary simulation studies show the accuracy of the concept of making up the subject of the project, simulation studies in which the system and parameters are handled and examined more comprehensively are required. Within simulation studies, 1. Getting the relationship between the applied voltage value and the stress collapse amount when the collapse amount in the designed CT membranes is maximum, 2. Performing tests for different thin film thicknesses, 3. Examining the relationship between membrane tension and LW damping, 4. Membrane length and determination of the optimum value of the depth ratio (l/h) of the CT structure, selected simulation studies will be repeated using a 3D model. Applications such as beamforming and filtering and performing the proposed structure in these applications will also be investigated through simulation studies.

The design parameters before the fabrication step were optimized using simulation studies. In addition, a model has been created for the design (Figure 7) for shifting the center frequency with simulation studies and its operation has been examined. Variables, such as the change of the frequency band of the modeled LWR device and the shift range of the center frequency, were investigated by changing the system parameters.

Following the simulation studies, fabrication and verification studies were carried out, and in the last part of the project, the use of the obtained structure as a phase-shifting narrow-band filter was experimentally shown. The parameters such as Q factor and frequency band of the filter were got and the effect of phase-shifting on these parameters was investigated (Figure 64-65).

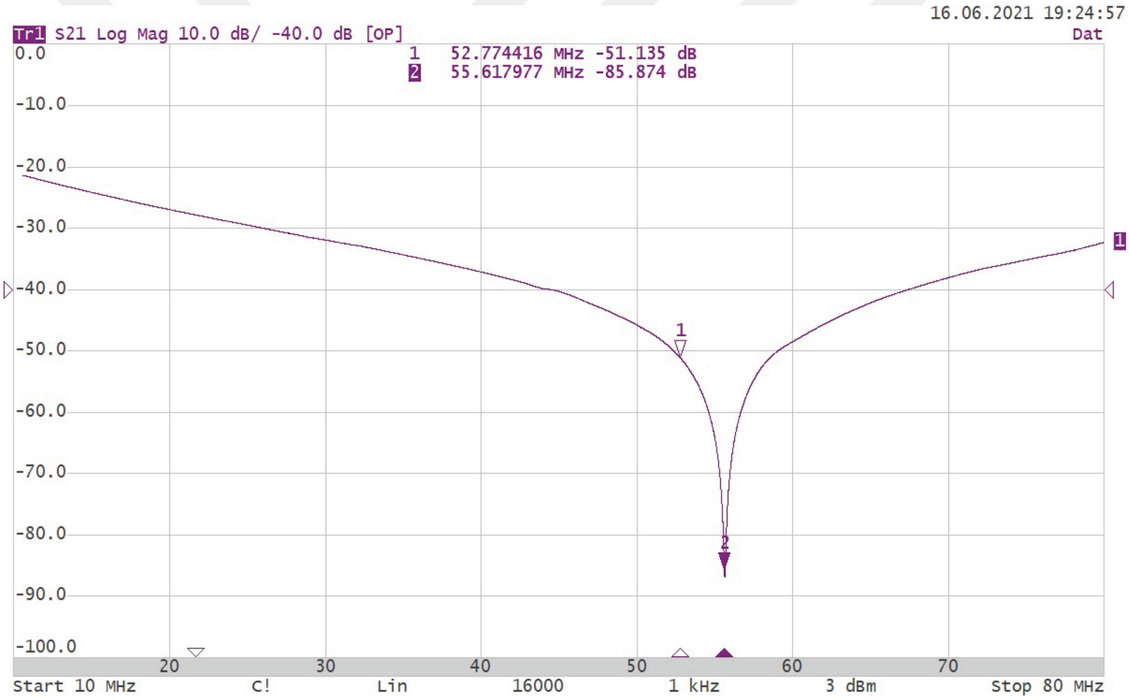

Figure 64: Network Analyzer results for the manufactured device, Center Frequency is 55 MHz.

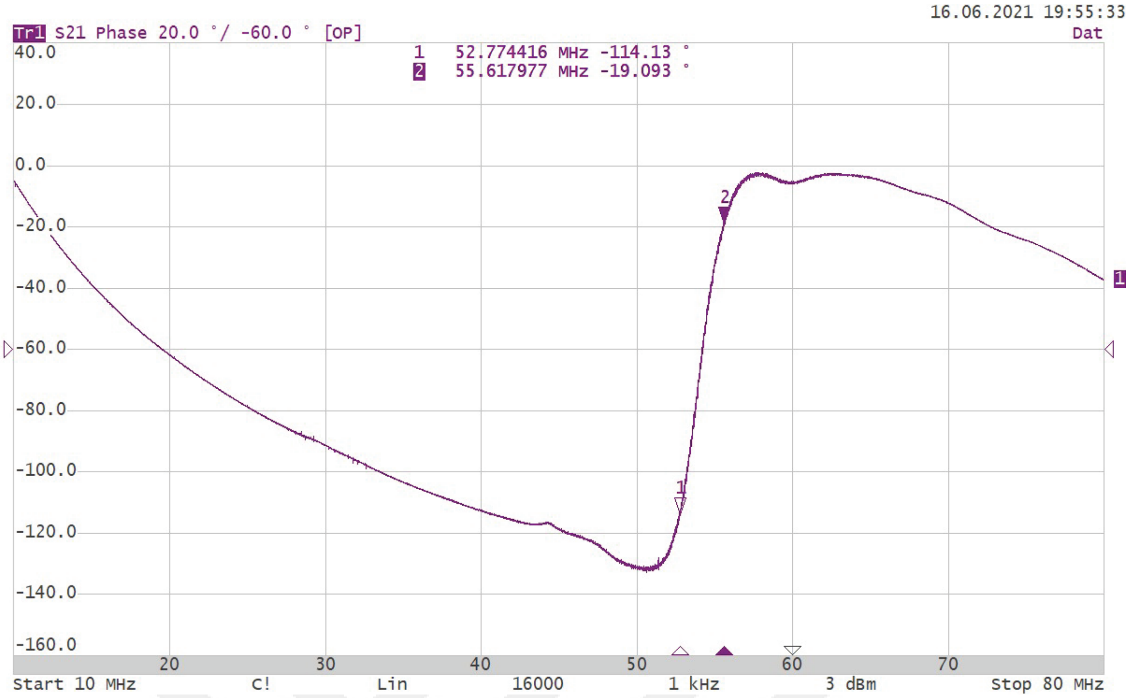

Figure 65: Phase change of the Center Frequency.

5. DISCUSSIONS AND EVALUATIONS

To enhance the sensor performance and stability, a reduction in insertion loss and unwanted spurious effects is essential. These reductions can be achieved by using a piezoelectric substrate with a high electromechanical coupling coefficient and controlling a few parameters, such as the IDT type, IDT length, aperture, and delay line length. Among these parameters, the IDT type is the most important parameter for realizing low insertion loss and improving device stability [26].

Our FUTURE APPROACH in the study is to try the FIDT (focused-IDT) structure, so a novel IDT approach for LW devices and to compare its performance data. We propose that energy loss in the delay line will be reduced and more efficient filtration will be made.

Because of the searches made through YÖKSİS, some theses that were previously studied with Lamb Waves were determined. Lamb Waves were used in the imaging of layered structures via a conical axion structure by focusing with an acoustic microscope (Yemişçiler, 1989) [117].

In studies on Acoustic Microscopy (Bozkurt, 1994), (Yaralıoğlu, 1994), non-contact and non-destructive testing was performed using Lamb Waves [118], [119].

Capacitive micro-mechanics studies (Bozkurt, 2000) have been carried out to generate and detect ultrasonic sound waves [120].

Lamb Waves, which have high energy efficiency in interface acoustic waves, were used for liquid density measurements (Bostan, 2017) [121].

Lamb Waves took part in an experimental study on damage detection technologies (Yılmaz, 2018) for the control of micro-cracks on surfaces [122].

These studies did not focus on evaluating the efficiency and sensitivity of the effects of IDT formation in the production of Lamb waves. We are investigating that a higher efficiency filter can be produced on the basis of the increase in sensitivity and energy efficiency brought by the innovative FIDT structure that synthesis with proposes in our study.

6. CONCLUSION

The lamb wave (LW) based MEMS, have an important potential to use in new generation high-frequency filters, oscillators, and sensor designs. LW oscillators stand out among MEMS technologies with their CMOS compatibility, high-frequency operation, low motion impedance, and multi-frequency operation. LW Devices are formed by depositing comb-shaped transmit/receive electrodes (Interdigital Transducer, IDT) on a thin piezoelectric membrane. IDT structures can transmit and receive acoustic waves, but they cannot control the wave properties that are determined during fabrication, such as speed, frequency, and phase.

A two-port novel-lamb wave narrow-band filter design is proposed in this study. The LW filter enables control of the amount of phase difference between input and output signals. The structure contains a 2-port LW device fabricated using aluminum-nitride thin-film. A capacitive transducer (CT) is mounted to the cavity above the film to apply mechanical stress to the film. The CT transducer is excited by an analog voltage, which controls the stress inside the film. The stress results in a phase velocity change in the LW traveling through the film. The change in velocity leads to a phase difference between the input and output signals of the LW filter.

The physical structure is analyzed using a finite element model, that is built using the COMSOL multi-physics tool. The proposed concept is proved and the design parameters are optimized during the simulation studies. We have tested an LW device that has 200 nm AlN film and two-ported IDT structures that can excite acoustic waves with 100 MHz center frequency. A CT is placed under the film with a 1µm distance between its plates. The relation between the voltage applied to the CT, and the stress vs LW phase difference relation is investigated. The simulation shows that 1.2882-1.2993 radian phase shifts are provided by using 0-34.6 kPa applied stresses respectively, while the response is almost linear. These stress values can be provided by voltages applied to CT between 0-50 V respectively while the response is exponential.

For the fabrication, the wafer bonding technique is used: A. Bottom and B. Top structure.

Fabrication steps for bottom structure as Schematic 1: A1. 400 nm SiN coating to both sides of a DSP-Si wafer (PECVD), A2. 200 nm AlN coating on SiN(Sputtering), A3. IDT patterning using PMMA and EBL, A4. Chromium deposition (IDT Electrodes) and lift off, A5. 1 µm PR protection layer on the IDT electrodes, A6. Backside window patterning and dry etching of SiN under the electrodes, A7. Bulk wet etching of Si under the electrodes (using 30% KOH) A8. The SiN under the AlN film stops the etching operation. A9. Acetone rinse. The LF filter is ready.

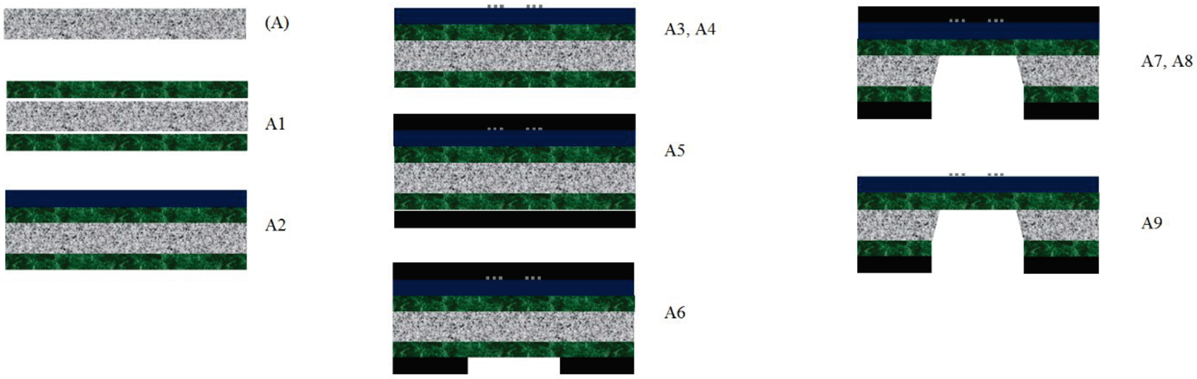

Schematic 1: Fabrication steps for bottom structure.

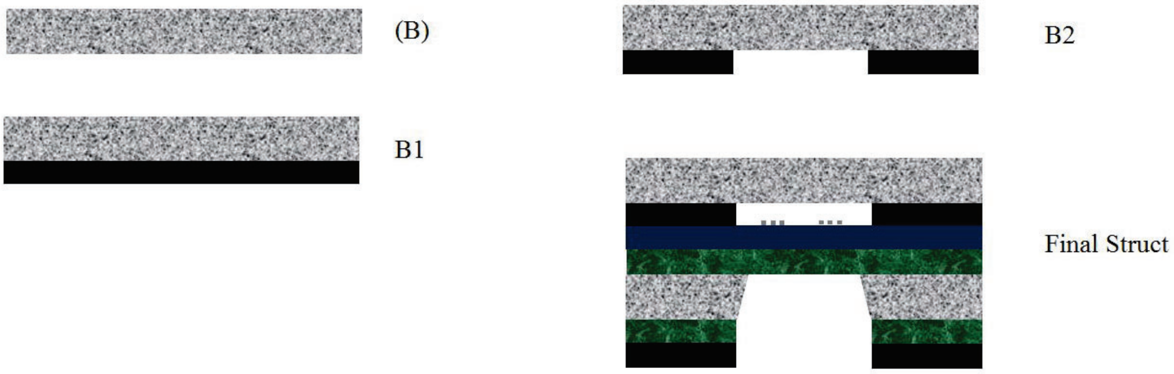

Schematic 2: Fabrication steps for top structure, and the schematic of the final form.

Fabrication steps for top structure as Schematic 2: B1. 1 µm PR is coated and cured on a doped Si wafer. B2. Pattern a window, which has a bigger area than IDT electrodes. Put the top structure (B) on top of IDT electrodes on the bottom structure. The window on the top structure will be aligned on the IDTs. The top structure forms a CT structure that is connected to a DC analog voltage (DC => p-doped Si, GND => Chromium coating on the bottom structure). The bottom structure has two ports for RF signals (input/output). In this thesis, the simulation results and the fabrication technique will be presented in detail. The results and the details about future work will be mentioned.

REFERENCES

[1] Nguyen, C. T.-C.: “MEMS Technology for Timing and Frequency Control”, *IEEE Trans. Ultrason. Ferroelect. Freq. Control*, vol. 54 **(2007)** 251–270.

[2] Yantchev, V.; Katardjiev, I.: “Thin Film Lamb Wave Resonators in Frequency Control and Sensing Applications: a Review”, *J. Micromech. Microeng*. 043001, vol. 23 **(2013)**.

[3] Piazza, G.; Stephanou, P.J.; Pisano, A.P.: “Piezoelectric Aluminum Nitride Vibrating Contour-Mode MEMS Resonators”, *J. Microelectromech. Syst.*, vol. 15 **(2006)** 1406–1418.

[4] Zou, J.; Lin, C.-M.; Chen, Y.-Y.; Pisano, A. P.: “Theoretical Study of Thermally Stable SiO2/AlN/SiO2 Lamb Wave Resonators at High Temperatures”, *J. Appl. Phys.* 094510, vol. 115 **(2014).**

[5] Lin, C.-M.; Chen, Y.-Y.; Felmetsger, V. V.; Senesky, D. G.; Pisano, A. P.: “AlN/3C–SiC Composite Plate Enabling High-Frequency and High-*Q* Micromechanical Resonators”, *Adv. Mater.*, vol. 24 **(2012)** 2722-2727.

[6] White, R.M.; Voltmer, F.W.: “Direct Piezoelectric Coupling to Surface Elastic Waves”, *Appl. Phys. Lett.*, vol. 7 **(1965)** 314-316.

[7] Toda, K.: “Lambwave Delay Lines with Interdigital Electrodes”, Citation: J. Appl. Phys. 44 **(1973)** 56-62.

[8] Bjurström, J.; Katardjiev, I.; Yantchev, V.: “Lateral-Field-Excited Thin-Film Lamb Wave Resonator”, Appl. Phys. Lett., vol. 86, 154103 **(2005)**.

[9] Zou, J.: “High-Performance Aluminum Nitride Lamb Wave Resonators for RF Front-End Technology”, *Doktora Tezi*, University of California, Berkeley, ABD **(2015)** 13-14.

[10] Piazza, G.: “Piezoelectric Aluminum Nitride Vibrating RF MEMS for Radio Front-End Technology”, Ph. D. dissertation, Department of Electrical Engineering and Computer Science, University of California, Berkeley, California, USA **(2005)**.

[11] Lin, C.-M.: “Temperature-Compensated and High-Q Piezoelectric Aluminum Nitride Lamb Wave Resonators for Timing and Frequency Control Applications”, Ph. D. dissertation, Department of Mechanical Engineering, University of California, Berkeley, California, USA **(2013)**.

[12] Yen, T.-T.: “Experimental Study of Fine Frequency Selection Techniques for Piezoelectric Aluminum Nitride Lamb Wave Resonators”, M. S. dissertation, Department of Electrical Engineering and Computer Sciences, University of California, Berkeley, California, USA **(2012)**.

[13] Wang, J.; Ren, Z.; Nguyen, C.T.-C.: “1.156-GHz Self-Aligned Vibrating Micromechanical Disk Resonator”, IEEE Trans. Ultrason. Ferroelectr. Freq. Control, vol. 51 **(2004)** 1607-1628.

[14] Yantchev, V.; Katardjiev, I.: “Micromachined Thin Film Plate Acoustic Resonators utilizing the Lowest Order Symmetric Lamb Wave Mode”, IEEE Trans. Ultrason. Ferroelectr. Freq. Control, vol. 54 **(2007)** 87-95.

[15] Weinstein, D.; Bhave, S.A.: “Internal Dielectric Transduction in Bulk-Mode Resonators”, J. Microelectromech. Syst., vol. 18 **(2009)** 1401-1408.

[16] Gong, S.; Kuo, N.-K.; Piazza, G.: “GHz High-Q Lateral Overmoded Bulk Acousticwave Resonators using Epitaxial SiC Thin Film”, J. Microelectromech. Syst., vol. 21 **(2012)** 253-255.

[17] Zou, J.: "High Quality Factor Lamb Wave Resonators", *Technical Report,* No. UCB/EECS-2014-217, EECS Department University of California, Berkeley **(2014)**.

[18] Rayleigh, L.: “On Waves Propagated along the Plane Surface on an Elastic Solid”, *Proc. London Math. Soc.*, vol. 17 **(1885)** 4-11.

[19] Love, A.E.H.: "Some Problems of Geodynamics", *the Cambridge University Press*, 1 st Ed. **(1911)**; *Dover, New York, USA.*, 2 st Ed. **(1967)** (Chapter 11: Theory of the propagation of seismic waves).

[20] Ballantine, D.S.; White, R.M.; Martin, S.J.; Ricco, A.J.; Frye, G.C.; Zellers, E.T.; Wohltjen, H.: “Acoustic Wave Sensors: Theory, Design, and Physico-Chemical Applications”, San Diego: Academic Press **(1997)**.

[21] White R.M.; Wenzel, S.W.: “Fluid Loading of a Lamb Wave Sensor”, *Appl. Phys. Lett.*, vol. 52 **(1988)** 1653-1655.

[22] Lamb, H.: “On Waves in an Elastic Plate”, Proceedings of the Royal Society, A: Mathematical, Physical and Engineering Sciences 93 **(1917)** 114–128.

[23] Court, I.N.; “Microwave Acoustic Devices for Pulse Compression Filters”, *IEEE Trans.*, MTT-17 *IEEE Trans.*, MTT-17 **(1969)** 968-986.

[24] Mortley, W.S.: "Pulse Compression by Dispersive Gratings on Crystal Quartz", *Marconi Rev.*, No.159 **(1965)** 273-290.

[25] Morgan, D.P.: "History of SAW", Proceedings of the 1998 IEEE International Frequency Control Symposium, Pasadena, May **(1998)**.

[26] Oh, H.; Lee, K.; Eun, K.; Choa, S.-H.; Yang, S.S.: "Development of a High-Sensitivity Strain Measurement System based on a SH SAW Sensor", Journal of Micromechanics and Microengineering **(2012)**.

[27] Yazdani, A.M.: "Size Based Micro Particle Separation usıng A Novel Acoustophoresıs Based Microfluidic System", *PhD Thesis*, Marmara University, İstanbul, Türkiye **(2019)**.

[28] Laurell, T.; Lenshof, A.: "Microscale acoustofluidics", Cambridge, UK: Royal Society of Chemistry **(2014)**.

[29] Shen, S. *et al.*: "High-Throughput Rare Cell Separation from Blood Samples using Steric Hindrance and Inertial Microfluidics", *Lab. Chip*, vol. 14, no. 14 **(2014)** 2525–2538.

[30] Nam, J.; Lim, H.; Kim, C.; Kang, J.Y.; Shin, S.: "Density-Dependent Separation of Encapsulated Cells in a Microfluidic Channel by using a Standing Surface Acoustic Wave", *Biomicrofluidics*, vol. 6, no. 2 **(2012)** 024120-024120–10.

[31] Gupta, S.; Feke, D.L.; Manas-Zloczower, I.: "Fractionation of Mixed Particulate Solids according to compressibility using Ultrasonic Standing Wave Fields", *Chem. Eng. Sci.*, vol. 50, no. 20 **(1995)** 3275–3284.

[32] Shi, J.; Huang, H.; Stratton, Z.; Huang, Y.; Huang, T.J.: "Continuous Particle Separation in a Microfluidic Channel via Standing Surface Acoustic Waves (SSAW)", *Lab. Chip*, vol. 9, no. 23 **(2009)** 3354.

[33] Ding X. *et al.*: "Cell Separation using Tilted-Angle Standing Surface Acoustic Waves", *Proc. Natl. Acad. Sci. U. S. A.*, vol. 111, no. 36 **(2014)** 12992–12997.

[34] Destgeer, G.; Ha, B.H.; Park, J.; Jung, J.H.; Alazzam, A.; Sung H.J.: "Microchannel Anechoic Corner for Size-Selective Separation and Medium Exchange via Traveling Surface Acoustic Waves", *Anal. Chem.*, vol. 87, no. 9 **(2015)** 4627–4632.

[35] Destgeer, G.; Ha, B.H.; Jung, J.H.; Sung H.J.: "Submicron Separation of Microspheres via Travelling Surface Acoustic Waves", *Lab. Chip*, vol. 14, no. 24 **(2014)** 4665-4672.

[36] Zou, J.: "High-Performance Aluminum Nitride Lamb Wave Resonators for RF Front-End Technology", *Doktora Tezi*, University of California, Berkeley, ABD **(2015)** 13-14.

[37] Rajendran, V.; Koike, M.; Hashimoto, K.-y.; Yamaguchi, M.: "Mass Density Sensor For Liquıds Using Zno-Film/Al-Foil Lamb Wave Device", IEEE 1992 Ultrasonics Symposium Proceedings **(1992)**.

[38] Zhou, L.; Wu, Y.; Xuan, M.; Manceau, J.-F.; Bastien, F.: "A Multi-Parameter Decoupling Method with a Lamb Wave Sensor for Improving the Selectivity of Label-Free Liquid Detection", Sensors 2012, 12 **(2012)** 10369-10380.

[39] Mirea, T.; Iborra, E.; Yantchev, V.: "S_0 Lamb Wave Resonators for In-Liquid Sensing: Promising alternative to Shear Bulk Acoustic Wave Devices", IEEE 2016 European Frequency and Time Forum (EFTF) **(2016)**.

[40] Sakharov, V.E.; Kuznetsov, S.A.; Zaitsev, B.D.; Kuznetsova, I.E.; Joshi, S.G.: "Liquid Level Sensor using Ultrasonic Lamb Waves", Ultrasonics, 41(4) **(2003)** 319–322.

[41] Lee, C.M.; Wong, K.M.; Chen, P.; Lau, K.M.: "GaN-based Lamb-Wave Mass-Sensors on Silicon Substrates", 2010 IEEE Sensors **(2010)** 2008-2011.

[42] Ochôa, P.; Infante, V.; Silva, J.M.; Groves, R.M.: "Detection of Multiple Low-Energy Impact Damage in composite plates using Lamb Wave Techniques", Composites Part B 80 **(2015)** 291-298.

[43] Chen, L.; Gui-e, L.; Jinyong, J.; Qiang, G.; Shaoguang, W.; Bin, W.: "Review on the Test Method of Adhesive Failure in Solid Rocket Motor", Joint International Mechanical, Electronic and Information Technology Conference (JIMET 2015) **(2015)** 675-681.

[44] Towsyfyan, H.; Biguri, A.; Boardman, R.; Blumensath, T.: "Successes and Challenges in Non-Destructive Testing of Aircraft Composite Structures", Chinese Journal of Aeronautics **(2019)**.

[45] Sharma, A.; Sinha, A.K.: "Ultrasonic Testing for Mechanical Engineering Domain: Present And Future Perspective", Int. J. Res. Ind. Eng. Vol. 7, No. 2 **(2018)** 243–253.

[46] Gandhi, N.; Michaels, J.E.; Lee, S.J.: "Acoustoelastic Lamb wave propagation in biaxially stressed plates. The Journal of the Acoustical Society of America, 132(3) **(2012)** 1284–1293.

[47] Roller, M.; Malocha, D.C.; Vaidyanathan, R.: "SAW OFC Strain Sensor", IEEE International Ultrasonics Symposium Ultrasonics Symposium (IUS) **(2009)** 2515-2518.

[48] Nalamwar, A.L.; Epstein, M.: "Propagation of Surface Acoustic Waves in Strained Media", 1975 Ultrasonics Symposium **(1975)** 484-487.

[49] Kadota, M.; Ogami, T.: "5.4 GHz Lamb Wave Resonator on $LiNbO_3$ Thin Crystal Plate and Its Application", Japanese Journal of Applied Physics 50 **(2011)** 07HD11-1-07HD11-4.

[50] Wingqvist, G.; Arapan, L.; Yantchev, V.; Katardjiev, I.: "A Micromachined Thermally Compensated Thin Film Lamb Wave Resonator for Frequency Control and Sensing Applications", J. Micromech. Microeng. 19 035018 (9pp) **(2009)**.

[51] Tancrell, R.H.; Schulz, M.B.; Barrett, H.H.; Davis, L., Jr.; Holland, M.G.: "Dispersive Delay Lines using Ultrasonic Surface Waves", Proceedings of the IEEE Proc. IEEE Proceedings of the IEEE. 57(6) USA **(1969)** 1211-1213.

[52] Daniel, M.R.; de Klerk, J.: "Acoustic Radiation Measurements and Calculations for Three Surface Wave Filter Designs", Conference Paper, 1973 Ultrasonics Symposium **(1973)** 449-455.

[53] Lin, C.-M.; Chen, Y.-Y.; Wu, T.-T.: "A Novel Weighted Method for Layered SAW Filters using Slanted Finger Interdigital Transducers", Journal of Physics D: Applied Physics, 39(3) **(2006)** 466–470.

[54] Ma, C.-C.; Huang, T.-J.; Yu, J.-M.: "Application of slanted finger interdigital transducer surface acoustic wave devices to ultraviolet array photodetectors", Journal of Applied Physics, 104(3) **(2008)** 033528.

[55] Li, S.-S.; Lin, Y-W.; Ren, Z.; Nguyen, C.T.-C.: "Self-Switching Vibrating Micromechanical Filter Bank", Proc. IEEE Intl. Freq. Control Symp. **(2005)** 135-141.

[56] Li, S.-S.; Lin, Y-W.; Ren, Z.; Nguyen, C.T.-C.: "A Micromechanical Parallel-Class Disk-Array Filter", Proc. IEEE Intl. Freq. Control Symp. **(2007)** 1356-1361.

[57] Hung, L.-W.; Nguyen, C.T.-C.: "Q-Boosted AlN Array-Composite Resonator with Q > 10000", Tech. Dig. IEEE Intl. Electron Devices Mtg. **(2010)** 162-165.

[58] Nguyen, C.T.-C.: "Integrated Micromechanical Radio Front-Ends. 2008 International Symposium on VLSI Technology", Systems and Applications (VLSI-TSA) **(2008)**.

[59] Çatlı, B.; Hella, M. M.: “A 1.94 to 2.55 GHz, 3.6 to 4.77 GHz Tunable CMOS VCO Based on Double-Tuned, Double Driven Coupled Resonators”, IEEE Journal Of Solid-State Circuits, Vol. 44, No. 9, September **(2009)** 2463-2477.

[60] Rinaldi, M.; Zuo, C.; Spiegel, J. V.; Piazza, G.: “Reconfigurable 4-Frequency CMOS Oscillator Based on AlN Contour-Mode MEMS Resonators”, IEEE International Ultrasonics Symposium Proceedings **(2010)** 1494-1497.

[61] Abdolvand, R.; Mirilavasani, H.; Ayazi, F.: “Single-Resonator Dual-Frequency Thin-Film Piezoelectric-on-Substrate Oscillator”, IEEE International Electron Devices Meeting **(2007)** 419-422.

[62] Safarian, Z.; Hashemi, H.: “A 1.3-6 GHz Triple-Mode CMOS VCO Using Coupled Inductors”, IEEE Custom Intergrated Circuits Conference (CICC) **(2008)** 69-72.

[63] Goel, A.; Hashemi, H.: “Frequency Switching in Dual-Resonance Oscillators”, IEEE Journal Of Solid-State Circuits, Vol. 42, No. 3, March **(2007)** 571-582.

[64] Zuo, C.; Spiegel, J.V.; Piazza, G.: “1.5-GHz CMOS voltage-controlled oscillator based on thickness-field-excited piezoelectric AlN contour-mode MEMS resonators”, IEEE Custom Integrated Circuits Conference **(2010)**.

[65] Al-Dahleh, R.; Mansour, R.R.: “High-Capacitance-Ratio Warped-Beam Capacitive MEMS Switch Designs”, Journal Of Microelectromechanical Systems, Vol. 19, No. 3, June **(2010)** 538-547.

[66] Piazza, G.; Stephanou, P.J.; Pisano, A.P.: “Piezoelectric Aluminum Nitride Vibrating Contour-Mode MEMS Resonators”, 1406 Journal Of Microelectromechanical Systems, Vol. 15, No. 6, December **(2006)** 1406-1418.

[67] Zou, J.; Lin, C.-M.; Lam, C.S.; Pisano, A.P.: “Transducer Design for AlN Lamb Wave Resonators”, Journal of Applied Physics, 154502 **(2017)** 121.

[68] Campbell, C. K.; Yanglin Y.; Sferrazza Papa, J. J.: “*Wide-Band Linear Phase SAW Filter Design Using Slanted Transducer Fingers”, IEEE Transactions on Sonics and Ultrasonics, 29(4)* **(1982)** 224–228.

[69] Campbell, C.: “Surface Acoustic Wave Devices and their Signal Processing Applications”, Academic Press, Inc., 1250 Sixth Avenue, San Diego, CA 92101 **(1989)** 59-83.

[70] Tobolka, G.: “Mixed Matrix Representation of Saw Transducers”, IEEE Transactions On Sonics And Ultrasonics, Vol. Su-26, No. 6 **(1979)**.

[71] Plessky, V.; Koskela, J.: “Coupling-Of-Modes Analysis Of Saw Devices”, International Journal Of High Speed Electronics And Systems **(2000)** 867–947.

[72] Smith, Jr., W.R.: “Studies of Microwave Acoustic Transducers and Dispersive Delay Lines”, Ph.D. Thesis in Department of Applied Physics, Stanford University (1969) 1-147.

[73] Smith, Jr., W.R.; Gerard, H.M.; Collins, J.H.; Reeder, T.W.; Shaw, H.J.: “Design of Surface Wave Delay Lines with İnterdigital Transducers”, *IEEE Trans. Microwave Theory and Techniques,* Vol. MTT-17 **(1969)** 865-873.

[74] Lehtonen, S.; Plessky, V.P.; Koskela, J.; Salornaa, M.M.: “Second Harmonic Reflectors on 128^0 LiNb03”, 2001 IEEE Ultrasonics Symposium. Proceedings. An International Symposium, Atlanta, GA, USA **(2001)** 139-143.

[75] Senturia, S.D.: “Microsystem Design”, Kluwer Academic Press, **(2001)** 109-147.

[76] O'Brien, G.J.; Monk, D.; Lin, L.: “Mems Cantilever Beam Electrostatic Pull-In Model”, Conference: 2006 Solid-State, Actuators, and Microsystems Workshop, June **(2006)**.

[77] Hashimoto, K.Y.: “Surface Acoustic Wave Devices in Telecommunications”, Springer, **(2000)** 27-30.

[78] Datta, S.: “Surface Acoustic Wave Devices”, Englewood Cliffs, NJ, Prentice-Hall, **(1986)** 29–40.

[79] Beckley, J.; Kalinin, V.; Voliansky, L.M.: “Noncontact torque sensors based on SAW Resonators”, IEEE Int. Frequency Control Symp. and PDA Exhibition, (2002) 202–13.

[80] Onen, O; Sisman, A.; Gallant, N.D.; Kruk, P.; Guldiken, R.: “A Urinary Bcl-2 Surface Acoustic Wave Biosensor for Early Ovarian Cancer Detection”, Sensors **(2012)** 7423-7437.

[81] Zuo, C.; Spiegel, J.V.; Piazza, G.: "1.05-GHz CMOS Oscillator Based on Lateral-Field-Excited Piezoelectric AlN Contour-Mode MEMS Resonators", IEEE Transactions on Ultrasonics, Ferroelectrics, and Frequency Control, January **(2010)** 82-87.

[82] Qi, X.:“Ultrasonic Guided Waves for Defect Characterization in Composite Structures”, *PhD Thesis*, The Pennsylvania State University, State College, PA,USA **(2011)** 10-11.

[83] Castaings, M.; Lowe, M.: “Finite Element Model for Waves Guided along Solid Systems of Arbitrary Section Coupled to İnfinite Solid Media”, The Journal of the Acoustical Society of America, 123(2) **(2008)** 696–708.

[84] Wilcox, P.D.; Velichko, A.: “Efficient Frequency-Domain Finite Element Modeling Of Two-Dimensional Elastodynamic Scattering”, The Journal of the Acoustical Society of America, 127(1) **(2010)** 155–165.

[85] Drozdz, M.; Skelton, E.; Craster, R.V.; Lowe, M.J.S.: “Modeling Bulk and Guided Waves in Unbounded Elastic Media Using Absorbing Layers in Commercial Finite Element Packages”, AIP Conference Proceedings **(2007)** 86-94.

[86] Noyan, M.A.: “Fabrication and Characterization of Zinc Oxide Based Surface Acoustic Wave Devices”, *MSc Thesis*, Bilkent University, Materials Science and Nanotechnology Program of The Graduate School of Engineering and Science, Ankara, Türkiye, **(2013)** 76.

[87] Wasa, K.; Kitabatake, M.; Adachi, H.: “Thin Film Materials Technology”, *1 st Ed.*, William Andrew Inc. **(2004)**.

[88] Wang, Q.J.; Pflügl, C.; Andress, W.F.; Ham, D.; Capasso, F.: “Gigahertz Surface Acoustic Wave Generation on ZnO thin films deposited by Radio Frequency Magnetron Sputtering on III-V Semiconductor Substrates”, Journal of Vacuum Science & Technology B: Microelectronics and Nanometer Structures Processing, Measurement, and Phenomena 26, 1848 **(2008)**.

[89] Kwan, J.K.W.: “Engineered Nanostructured Thin Films for Enhanced Surface Acoustic Wave Sensors”, *PhD Thesis*, University of Alberta, Edmonton, Alberta, Kanada, **(2013)** 33-35.

[90] Connacher, W.; Zhang, N.; Huang, A.; Mei, J.; Zhang, S.; Gopesh, T.; Friend, J.: “Micro/nano acoustofluidics: materials, phenomena, design, devices, and applications”, The Royal Society of Chemistry **(2018)**.

[91] Gurevich, G.L.; Sandler, M.S.; Sveshnikov, B.V.: “Radiation Losses in a SAW Resonator Formed by Interdigital type Reflectors”, Sov. Phys.-Radio Engng. & Electron., vol. 24, no.3 **(1979)** 28-36.

[92] Visintini, G.; Baghai-Wadji, M.-R.; Manner, O.: “Modular Two-Dimensional Analysis of SAW Filters-Part I: Theory”, IEEE Transactions on Ultrasonics, Ferroelectrics, and Frequency Control, Vol. 39, No. 1 **(1992)** 61-71.

[93] Namdeo, A.K.; Nemade, H.B.: "Simulation on Effects of Electrical Loading due to Interdigital Transducers in Surface Acoustic Wave Resonator", International Conference on Design and Manufacturing, IconDM **(2013)**.

[94] Skeie, H.: "Electrical and Mechanical Loading of A Piezoelectric Surface Supporting Surface Waves", Ultrasonics, 9(3), 180. Vol 48, No 5 **(1971)** 1098-1109.

[95] Jin, X.C.; Khuri-Yakub, B.T.; Degertekin, F.L.; Ladabaum, I.; Calmes, S.: "Micromachined Capacitive Ultrasonic Immersion Transducer For Medical Imaging", Proceedings of the 20th Annual Znternational Conference of the ZEEE Engineering in Medicine and Biology Society, Vol. 20, No 2, **(1998)** 779-782.

[96] Badi, M.H.; Yaralioglu, G.G.; Ergun, A.Ş.; Degertekin, F.L.; Cheng, C.H.; Khuri-Yakub, B.T.: "A First Experimental Verification Of Micromachined Capacitive Lamb Wave Transducers", IEEE Ultrasonics Symposium. Proceedings. An International Symposium vol.1 **(2000)**.

[97] Jin, X.; Oralkan, Ö.; Degertekin, F.L.; Khuri-Yakub, B.T.: "Characterization of One-Dimensional Capacitive Micromachined Ultrasonic Immersion Transducer Arrays", IEEE Transactions On Ultrasonics, Ferroelectrics, And Frequency Control, vol. 48, no. 3, May **(2001)** 750-760.

[98] Na, S.; Zheng, Z.; Chen, A.I.; Wong, L.L.P.; Li, Z.; Yeow, J.T.W.: "Design And Fabrication Of A High-Power Air-Coupled Capacitive Micromachined Ultrasonic Transducer Array With Concentric Annular Cells", IEEE Transactions On Electron Devices, Vol. 64, No. 11, November **(2017)** 4636-4643.

[99] Lucarini, I.; Maiolo, L.; Savoia, A.S.: "Fabrication and Characterization of Capacitive Micromachined Ultrasonic Transducers Integrated on Ultra-thin and Flexible Substrates", IEEE International Ultrasonics Symposium (IUS), Conference Paper, Glasgow, Scotland, October 6-9 **(2019)** 778-780.

[100] Chen, A.I.H.; Wong, L.L.P.; Li, Z.; Na, S.; Yeow, J.T.W.: "Practical CMUT Fabrication With A Nitride-To-Oxide-Based Wafer Bonding Process", Journal Of Microelectromechanical Systems, Vol. 26, No. 4, August **(2017)** 829-836.

[101] Hickernell, F.S.: "Zinc Oxide Films for Acoustoelectric Device Applications", IEEE Transactions on Sonics and Ultrasonics, 32(5) **(1985)** 621–629.

[102] Kobayashi, Y.; Tanaka, N.; Okano, H.; Takeuchi, K.; Usuki, T.; Shibata, K.: "Characteristics of Surface Acoustic Wave on AlN Thin Films", The Japan Society of Applied Physics, Japanese Journal of Applied Physics, Volume 34, Number 5S **(1995)**.

[103] Ishihara, M.; Li, S.; Yumoto, H.; Akashi, K.; Ide, Y.: "Control of Preferential Orientation of AlN Films Prepared by The Reactive Sputtering Method", Thin Solid Films 316(1-2) **(1998)** 152-157.

[104] Takagaki, Y.; Santos, P.V.; Wiebicke, E.; Brandt, O.; Schönherr, H.-P.; Ploog, K.H.: "Guided Propagation of Surface Acoustic Waves in AlN and GaN Films Grown On 4*H*–SiC(0001) Substrates", Physical Review B, 66(15) 155439 **(2002)**.

[105] Takagaki, Y.; Santos, P.V.; Wiebicke, E.; Brandt, O.; Schönherr, H.-P.; Ploog, K. H.: "Superhigh-Frequency Surface-Acoustic-Wave Transducers using AlN layers grown on SiC Substrates", Applied Physics Letters, 81(14) **(2002)** 2538–2540.

[106] Li, J.; Wang, C.; Liu, M.: "Design and Fabrication of a Novel PZT Films Based Piezoelectric Micromachined Ultrasonic Transducers", International Conference on Measuring Technology and Mechatronics Automation, Vol. 2, Conference Paper **(2009)** 45-49.

[107] Wang, H.; Yu, Y.; Chen, Z.; Yang, H.; Jiang, H.; Xie, H.: "Design and Fabrication of a Piezoelectric Micromachined Ultrasonic Transducer Array Based on Ceramic PZT", 2018 IEEE SENSORS, Conference Paper **(2018)**.

[108] Ahn, H.; Sung, M.; Been, K.; Moon, W.: "Design and fabrication of a piezoelectric micromachined ultrasound array transducer for photoacoustic imaging applications", 2014 11th International Conference on Ubiquitous Robots and Ambient Intelligence (URAI), Conference Paper **(2014)** 73-76.

[109] Liu, W.; Li, X.; Wu, D.; Yu, T.: "Design and Fabrication of Flexible and Transparent Piezoelectric Micromachined Ultrasonic Transducer Based on Mica Substrates", 2019 IEEE International Ultrasonics Symposium (IUS), Conference Paper **(2019)** 785-787.

[110] Thao, P.N.; Yoshida, S.; Tanaka S.: "Development of Mechanically-Robust Piezoelectric Micromachined Ultrasonic Transducer (pMUT) with Island-Shaped PZT Monocrystalline Thin Film", 2019 20th International Conference on Solid-State Sensors, Actuators and Microsystems & Eurosensors XXXIII (TRANSDUCERS & EUROSENSORS XXXIII), Conference Paper **(2019)** 833-836.

[111] Luo, G.; Horsley, D.A.: “Piezoelectric Micromachined Ultrasonic Transducers with Corrugated Diaphragms Using Surface Micromachining”, 2019 20th International Conference on Solid-State Sensors, Actuators and Microsystems & Eurosensors XXXIII (TRANSDUCERS & EUROSENSORS XXXIII), Conference Paper **(2019)** 841-844.

[112] Prakash, J.; Bose, G.: “Aluminum Nitride (AlN) Film Based Acoustic Devices: Material Synthesis and Device Fabrication”, Acoustic Waves - From Microdevices to Helioseismology **(2011)**.

[113] Clement, M.; Vergara, L.; Sangrador, J.; Iborra, E.; Sanz-Hervás, A.: “SAW Characteristics of AlN Films sputtered on Silicon Substrates”, Ultrasonics, 42(1-9) **(2004)** 403–407.

[114] Fu, Y.Q.; Luo, J.K.; Nguyen, N.T.; Walton, A.J.; Flewitt, A.J.; Zu, X.T.; Li, Y.; McHale, G.; Matthews, A.; Iborra, E.; Dui, H.; Milne, W.I.: “Advances in Piezoelectric Thin Films for Acoustic Biosensors, Acoustofluidics and Lab-On-Chip Applications”, Progress in Materials Science 89 **(2017)** 31-91.

[115] Jian, S-J.; Chu, S-Y.; Huang, T-Y.; Water, W.: “Study of Preferred Orientation of Zinc Oxide Films on the 64 ° $LiNbO_3$ substrates and their applications as Liquid Sensors”, Journal of Vacuum Science & Technology A 22 **(2004)** 2424-2430.

[116] Gerfers, F.; Kohlstadt, P.M.; Ginsburg, E.; He, M.Y.; Samara-Rubio, D.; Manoli, Y.; Wang, L.-P.: “Sputtered AlN Thin Films for Piezoelectric MEMS Devices - FBAR Resonators and Accelerometers”, Solid State Circuits Technologies **(2010)** 333-352.

[117] Yemişçiler, O.: “Imaging layered structures using focused lamb waves”, Yüksek Lisans Tezi, Orta Doğu Teknik Üniversitesi / Fen Bilimleri Enstitüsü, Elektrik ve Elektronik Mühendisliği, Ankara, Türkiye **(1989)**.

[118] Bozkurt, A.: “The V-Groove lens”, Yüksek Lisans Tezi, Karadeniz Teknik Üniversitesi / Fen Bilimleri Enstitüsü, Elektrik ve Elektronik Mühendisliği, Trabzon, Türkiye **(1994)**.

[119] Yaralıoğlu, G.G.: "Material characterization by using high velocity modes", Yüksek Lisans Tezi, Bilkent Üniversitesi / Mühendislik ve Fen Bilimleri Enstitüsü, Elektrik ve Elektronik Mühendisliği, Ankara, Türkiye **(1994)**.

[120] Bozkurt, A.: "Modeling and characterization of capacitive micromachined ultrasonic transducers", Doktora Tezi, Bilkent Üniversitesi / Mühendislik ve Fen Bilimleri Enstitüsü, Elektrik ve Elektronik Mühendisliği, Ankara, Türkiye **(2000)**.

[121] Bostan, O.: "Fluid property measurements using planar Quasi-Scholte waveguides", Yüksek Lisans Tezi, İzmir Yüksek Teknoloji Enstitüsü / Mühendislik ve Fen Bilimleri Enstitüsü / Makine Mühendisliği Ana Bilim Dalı, İzmir, Türkiye **(2017)**.

[122] Yılmaz, Ç.: "Monitoring Micro-Damage Accumulation Based on Reduction in Elastic Properties Using Fiber Bragg Grating Sensors, and Acoustic Emission and Thermography Methods in Fiber Reinforced Polymeric Composites", Doktora Tezi, Sabancı Üniversitesi / Mühendislik ve Fen Bilimleri Enstitüsü / Malzeme Bilimi ve Mühendisliği Ana Bilim Dalı / Malzeme Bilimi ve Mühendisliği Bilim Dalı, İstanbul, Türkiye **(2018)**.